Stony Brook University

The official electronic file of this thesis or dissertation is maintained by the University Libraries on behalf of The Graduate School at Stony Brook University.

STRUCTURAL HEALTH MONITORING AND ENERGY HARVESTING FOR RAILROAD

A Thesis Presented

by

GOPINATH REDDY PENAMALLI

to

The Graduate School

in Partial Fulfillment of the

Requirements

for the Degree of

Master of Science

in

Mechanical Engineering

Stony Brook University

August 2011

Stony Brook University

The Graduate School

Gopinath Reddy Penamalli

We, the thesis committee for the above candidate for the

Master of Science degree, hereby recommend

acceptance of this thesis.

Zuo, Lei **– Thesis Advisor**
Assistant Professor in Mechanical Engineering

Jeffrey, Ge **– Chairperson of committee**
Professor and Deputy Chair of Mechanical Engineering

Kao, Imin **– Committee Member**
Associate Dean in College of Engineering and Applied Sciences

This thesis is accepted by the Graduate School

Lawrence Martin
Dean of the Graduate School

Abstract of the Thesis

STRUCTURAL HEALTH MONITORING AND ENERGY HARVESTING FOR RAILROAD

by

Gopinath Reddy Penamalli

Master of Science

in

Mechanical Engineering

Stony Brook University

2011

Untimely damage detection/heath monitoring of rails and improper functioning of the trackside infrastructure like signals, gates, switches etc results in service disruptions, inefficient transportation management, or severe train accidents and cause huge direct and indirect losses. To facilitate policy makers and rail transportation agencies to make informed decisions on operating and managing the region's transportation system implementing continuous health monitoring methods for rails and self powering the railway track side electric infrastructure is essential.

In this thesis continuous structural health monitoring methods for rail is developed. The train(actuator) induced elastic waves are used for long range damage detection and piezoelectric admittance based methods are used for localized damage detection. Train induced high frequency elastic waves are analyzed by taking the wheel-rail interaction as the moving Hertzian contact forces using the semi-analytical finite element analysis. Their feasibility for long range damage detection is explained by calculating their decay rate. Low cost piezoelectric admittance based method using higher order inductive circuits is analyzed. The circuit parameters are optimized to enhance admittance damage metric sensitivity for localized damage detection.

Energy harvested from the railway track vibrations due to the moving trains can be used to self power the railway track side electric infrastructure. In this thesis the available power in the track site is estimated. Conventional Linear electromagnetic energy harvesters are assessed for energy harvesting from the erratic railway track vibrations and improvements to the linear

harvester design to achieve high power density are discussed. A novel high efficient and reliable rotational energy harvester suitable for the irregular track vibration energy harvesting is proposed. The harvester designed has <u>mechanical motion rectifier to convert the irregular up-and-down vibration into regular unidirectional rotation</u> and a <u>flywheel to stabilize the generator speed</u>. A full-scale prototype of this novel energy harvester was built and preliminarily tested in lab. The power harvested is sufficient enough for powering the track side electric infrastructure like signal lights, track switches etc as well as the structural health monitoring systems.

Contents

List of figures

List of tables

Acknowledgements

I owe my thanks to all those people who have made this thesis possible and because of whom my graduate experience has been one that I will cherish forever.

Firstly, I would like to express my sincere gratitude to my advisor, Dr. Lei Zuo, for his constant guidance, supervision and encouragement throughout my Master's program and also with my research. He has been a continuous source of knowledge and motivation and has helped me to enhance my skills set.

I would like to thank Dr. Jeffrey Ge and Dr. Imin kao for their time and effort in serving as committee members and also helping through my graduate studies. I would like to appreciate George and Lester for their help in the machine shop.

I am indebted to the members of the *Energy harvesting and Mechatronics lab group* , Xiudong, Peisheng, Xiaoming, Tao, Wanlu, Zhongjie, Gausheng and Bo with whom I have interacted during the course of my graduate studies. Especially Xiudong with whom I shared all my thoughts, his support and guidance helped me to overcome setbacks and stay focused. I greatly value their friendship and I deeply appreciate their belief in me. I am also thankful to my senior design team members John, Joseph and Paul.

I am obliged to my parents, my sister and brother in-law, without whom I wouldn't have succeeded in at least a single phase of my graduate studies. I dedicate this thesis to my parents for their love, endless support and encouragement all through my education. I also thank my friends who have been offering encouragement throughout my graduate studies.

Chapter 1 - Motivation and literature review

1 Motivation

The railroad transportation, including the commuter rail and subway, plays a very important role in the economy and quality of life for the people. About two-thirds of all U.S. passenger rail riders, and one in every three U.S. mass transit users, rides trains in the New York Metropolitan Region. To facilitate policy makers and transportation agencies to make informed decisions on operating and managing the region's transportation system, continuous structural health monitoring of rails and proper maintenance of the track side electric infrastructures (signal lights, road crossing gates, wireless communication, train and track monitoring, positive train control, etc) is very much essential.

Unfortunately, the continuous structural health monitoring of rails and the cost-effective and reliable power supply needed for the electrical infrastructures remains a challenge. The existing rail damage detection/health monitoring system need a moving actuator and sensing system and the track should be traffic free while operating them. This leads to untimely damage detection which happens once in a year. Significant portion of the rails are in the underground tunnels, on the bridges, or in relative remote areas, as shown in Figure 1.1 where the energy needed to power electric infrastructure is uneconomical to install and maintain. Thus failure of the continuous structural health monitoring and cost-effective electrical supply for railway electrical infrastructures leads to service disruptions, inefficient transportation management, severe train accidents and derailments.

Figure 1.1 (a)No warning lights and gates in remote area, (b) subway tunnels requires significant expenditure for power wiring and (c) improper track structure monitoring and positive train control.

Safety statistics data from the US Federal Railroad Administration indicate that train accidents caused by track failures resulted in 2700 derailments and $441 million in direct costs during the 1992-2002 decade [1]. The primary cause of these accidents is the transverse defect type that was found responsible for 541 derailments and $91 million in cost during the same period. Transverse defects are cracks developing in a direction perpendicular to the rail running direction as show in Figure 1.2.The statistics of 2000-2009 shown in Figure 1.3 indicates that there is no significant decrease in the number of train derailments[1].

Figure 6.2 Transverse crack
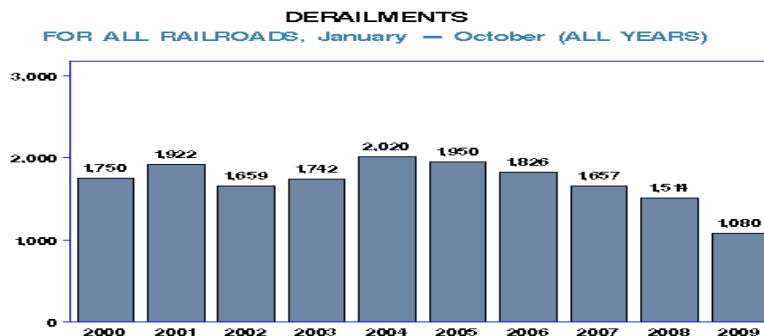
Figure 1.3 Derailments statistics for the decade 2000-2009 [1]

Though the existing damage detection methods are very developed they still need a special moving type actuating and sensing system[2-10] and is operated only once in every six months or an year. The damage may occur in this idle period and leads to the train derailment. Many technologies for railway energy harvesting like piezoelectric and electromagnetic are also investigated[11-12]. The power output from these harvesters is in the milliwatts which is not sufficient to power most of the railway track side infrastructure.

Minimizing train accidents and maintaining proper traffic control can only be achieved by implementing continuous structural health monitoring of the rail and developing high efficiency and reliable energy harvesters that can harvest high power, sufficient to power most of the track side electric infrastructure (requires around 50-100watts) along with the health monitoring systems. This can be done by the following

1) Using train as an actuator i.e. the wheel-rail interaction forces will induce the guided waves in the rail, these guided waves can be used for long range damage detection in rails. Since the trains operate frequently the system is continuous.

2) Using improved localized damage detection methods like low cost and small size piezoelectric impedance based methods for detecting damages in bolted rail joints and welded rail joints.

3) High power should be harvested from the railway track vibrations caused due to the moving trains using high efficient vibrational energy harvesters to power the track side electric infrastructure like signals, gates, switches etc and also self power the sensors, actuators and data processing systems used for the health monitoring of the railroad.

The conventional damage detection methods like ultrasonic transduction, guided waves, electromagnetic acoustic transduction (EMAT), and acoustic emission technique [4&5] require a specific actuator to excite the waves into the rail. Other methods like radiography[13&14], visual cameras, eddy current sensing[6], infrared[3] and magnetic induction [2]require a specific moving system(on or near the rail) to detect the damage. The moving train can induce great deal of energy to the railroad track through the moving wheel-rail interaction Hertzian contacts, which lead to high frequency elastic /guided waves that can propagate miles beyond the actual train[15]. Since trains operate very frequently these trains induced waves can be used for continuous health monitoring of rails. The theoretical study of these waves is important before implementing them. But so far little work has been done for rail damage detection using environmental excited high frequency waves i.e. the train induced high frequency waves. In this thesis in chapter 2 we take the moving train as an "actuator", investigated high frequency elastic waves in the rail due to Hertzian contact of wheel rail interaction, and the feasibility of these waves for the long range damage detection in rails is explained by considering their decay rate.

The guided wave based method are not efficient in detecting damage at the joints like the welded and bolted joints of the rails due to the sudden change in the cross sectional shape and also the medium of the structure. To detect damage in the rail joints, localized damage detection methods like the impedance based methods are to be used. The conventional piezoelectric impedance based methods need a heavy impedance analyzer which are very expensive and occupy large space when implemented in field[16]. The low cost methods are developed which need simple piezoelectric resistive circuits[17] and some small signal analyzing systems which can be

implemented on fields. These current low cost and small size impedance based methods are low sensitive to the smaller crack[17] and detecting the crack at initial stage is very important in rails because of their continuous operation. In this thesis in chapter 3 the <u>new low cost piezoelectric inductive circuits are analyzed and the circuit parameters are optimized for enhancing the damage detection metric sensitivity</u>. These enhanced piezoelectric inductive circuits can detect much smaller cracks at initial stages and can be implemented to the localized damage detection in railroad application.

When the loaded train moves on the track it vibrates due to the load exerted by the wheels. These vibrations can be used to harvest energy that can power most of the railway track electric infrastructure along with the health monitoring sensors. The conventional energy harvesting techniques like the piezoelectric[11] and electromagnetic[12] when implemented for the railway track vibration application are very low efficient and can only produce power of 2-3 watts maximum. The conventional type energy harvesters are very ineffective in railway application because the track vibration is like a pulse[18] and can only produce instantaneous peak power. In this thesis in chapter 4 the linear electromagnetic harvesters are analyzed for track vibration application and improvements were suggested for railway energy harvesting implementation. In chapter 5 a new type of <u>high efficient and reliable energy harvester with mechanical motion rectifier and an integrated flywheel</u> is developed and tested which can produce direct DC power from the pulse like railway track vibrations caused due to moving train.

The literature review of the current existing guided wave methods for long range damage detection in rail, Piezoelectric Impedance based methods for the localized damage detection and existing railway track side energy harvesting methods is discussed in the below sections of this chapter.

1 Literature review

1.1 Guided Waves based structural health monitoring

1.1.1 Introduction

The transverse cracks can be detected by using the waves travelling in the direction of the motion of the train. Frequency over KHz is required because the smaller cracks of size below 1cm have to be detected. There are many high frequency wave based damage detection methods developed

like ultrasonic transduction[4&5], guided waves[15], electromagnetic acoustic transduction (EMAT), acoustic emission technique [8&10]. Where the ultrasonic and guided waves are wave based methods used for long range damage detection i.e. these techniques can detect the damage over several hundred meters from the actuation. The electromagnetic acoustic transduction can detect the damage by measuring the change in the eddy currents of the sensors due to the damage in the sensing region and acoustic emission measures the crack propagation sound along the rail both these methods can detect the damage over a certain region around the actuator and a moving type actuator is used when these methods are used in detecting the damages in rails[10].

There are also many other methods like radiography[13&14], visual cameras, pulsed eddy current sensing[6], infrared and magnetic induction [2]. Radiographic inspection of rails can be carried out using either gamma or X-ray sources. Visual inspection is carried out only by experienced personnel walking along the rail track and physically looking for defects. In the eddy current pulsed sensing method the induced eddy currents are disturbed causing fluctuations in the magnetic field giving rise to changes in the impedance of the eddy current sensor. In the infrared based damage detection an infrared camera is moved along the rail and the record infrared image, simultaneously the recorded image is used to find the damages in the rails by image processing. In the magnetic flux induction method the actuating magnetic coil will induce the magnetic flux into the rail and the sensing coil detects a change in the magnetic field caused due to the discontinuity (transverse crack) and the defect indication is recorded. All these methods describe in this paragraph can only detect the damages over the localized region of the actuator or the sensor unlike the ultrasonic or the guided wave methods. These methods are also not very fast and when applied to the rail damage detection these methods become ineffective because a moving type of system should be used.

The guided waves based methods and ultrasonic methods have gained popularity because of their ability to detect damages over long range and at a greater speed which is important of the railway track health monitoring. However the guided waves are preferred to ultrasonic methods because of their easy implementation and better damage detection ability[2]. The later section reviews the work done by some researches on implementing the guided waves for the damage detection in rails.

1.1.2: Modeling of guided waves:

At low frequencies below 2 KHz railway track vibrations due to the train are dominated by vertical bending waves caused due to continuous moving load on a simple beam supported elastically. At high frequency up to 100 KHz or above, elastic waves can travel along the rail tracks as guided waves for long distance before they damp out. This elastic waves cannot be modeled by conventional finite element analysis (FEA).

Hayashi et al. [19] first proposed a different finite element method called semi analytical finite element method (SAFE) for the analysis of high frequency elastic waves in arbitrary cross sections and predicted the dispersion curves up to 100 KHz. Assuming plain strain, a cross-section of a rail is divided in the thickness direction into layered elements as shown in Figure 1.4, and waves in the propagating direction x are described by the orthogonal function e^{inx} where n is the wavenumber of the Lamb wave. The

Figure 1.4 Directions of wave propagation

m[th] eigenvalue nm of the eigensystem denotes the wavenumber of the mth resonance mode.

The main advantage of this method is it reduces the three dimensional analysis to two dimensional one and reduces lot of computational effort. This SAFE method is described in detail in section 1.1. The dispersion curve and the phase velocity are shown in Figure 1.5. The dispersion curves shows that the guided waves have multi modes at particular frequency[19].
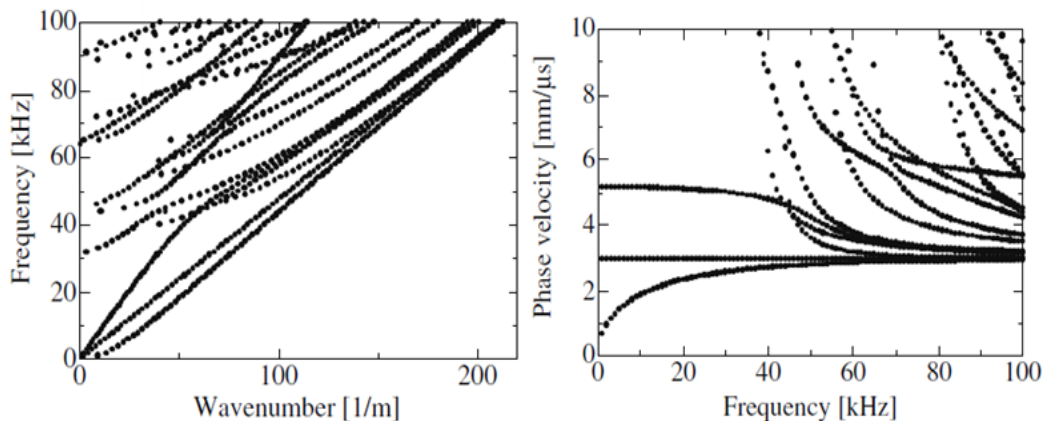
Figure 1.5 Dispersion curves and phase velocity of the rail [19]

The above modeling by Hayashi et al. [19] was done considering that the guided waves travel long distance and has very less damping. Linza di scalea et al.[20] extended SAFE for the different structures including rail by introducing the complex damping stiffness matrix based on Kelvin-Voigt viscoelastic model which contributes for the decay of the wave, and predicted the dispersion curves and group velocities/energy velocities. The cross section of the rail is shown in Figure 1.6 and the phase velocity and group velocity after considering the damping in the structure are shown in Figure 1.7. The structural damping will not change the phase velocity it will change the group velocity.
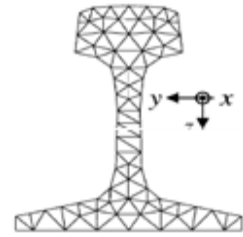
Figure 1.6 rail cross section
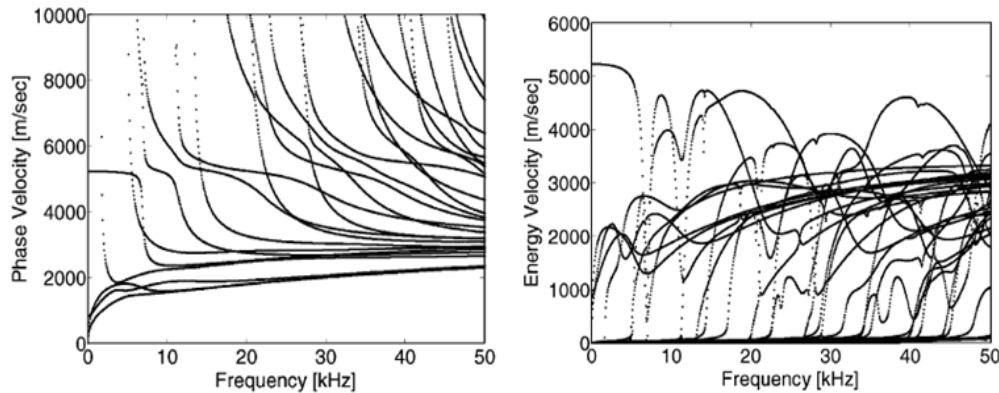
Figure 1.7 Phase velocity and group/energy velocity by considering damping in the structure [20]

Ryue et al [21] extend the modeling and showed 63 different types of vertical, lateral and torsional high frequency waves propagate in the rails using SAFE and validated conducting experiments using impact hammer and piezoelectric excitations. They also separated the waves that travel only certain parts of the rail like a localized head bending wave travels primarily through the rail head in the vertical direction above 15 kHz. At the side of the rail head, the primary wave measured is a lateral bending wave which has global deformation including the web and rail head in the lateral direction. The first-order web bending wave propagates dominantly through the web above 10 kHz. The waves propagating along the foot do not travel long distance because of the rail foundation which has a large damping effect.

Further Ryue et al [22] investigated the decay rates of waves propagating along a railway track in the frequency region up to 80 kHz by means of WFE analysis in the rails by measuring the damping loss factor and validated it by experiments. From this prediction, it was identified that

the decay rates of waves that propagate furthest are predominantly influenced by the damping of the rail, not by the damping of the rail pads. They concluded that the most effective frequency range for long range wave propagation along railway tracks is between 20 and 40 kHz. The maximum propagating distances that can be detected will be about 1.2km at the rail head and about 1.0 km at the web, respectively.

1.1.3 Implementation of guided waves in rails

Linza di scalea et al.[23-25] developed a small movable sensing system using EMAT(electro-magnetic acoustic transmission sensors) as shown in Figure 1.8 and used it for guided wave based damage detection in rails. A high frequency excitation hammer up to 50kHz is used to actuate the guided wave in the rail. Air coupled EMAT sensors are used for sensing the transverse crack and longitudinal crack in the rail. Figure 1.9 shows that this method can detect the transverse crack at a distance of 15mts from the actuator and sensing system. Hence concluded that guided wave based method is applicable for long range transverse crack detection in rails.

Figure 1.8 Movable sensing system using air coupled EMAT sensors [23]
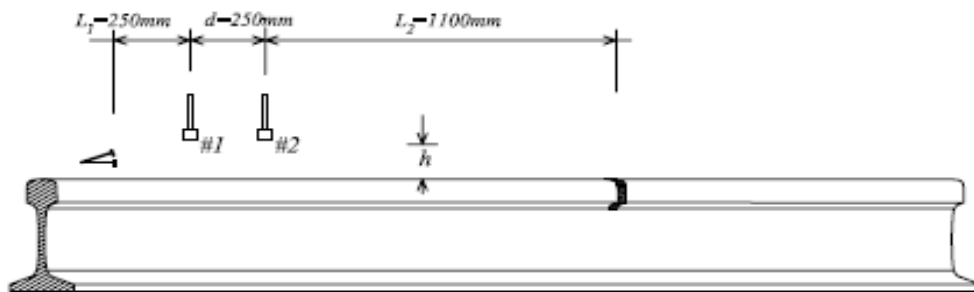
Figure 1.9 Crack detection using impact hammer actuator and air-coupled sensor [23]

Cawley et al.[26&27] have developed a G-Scan guided wave inspection system show in Figure 1.10 which can actuate and sense the guided waves. The G-Scan guided wave inspection system uses an array of transducers to generate one specific guided wave mode at one frequency by suppressing the other modes at the same frequency. Also this G-Scan guided wave inspection system can induce guided waves only to a specific portion of the rail like only to the rail head or only to the rail web or foot to detect the damage in them. This G-scan system will sense the wave that is reflected from a transverse crack and compares the reflection coefficient value with the predicted one to indicate the damage.
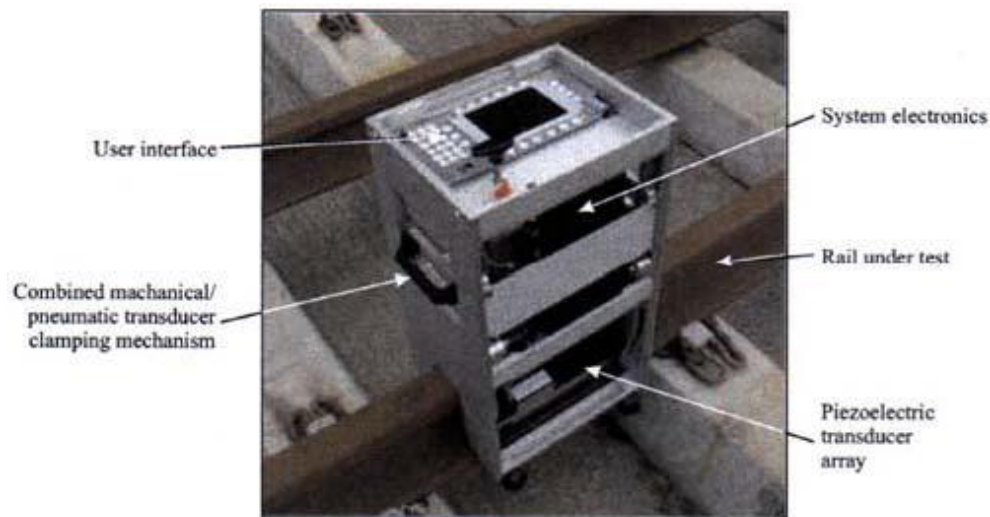
Figure 1.10 G-Scan guided wave inspection system [27]

Rose[28] also demonstrated the potential of guided waves in the long range damage detection of rails using an pneumatic actuator similar to impact hammer and an air coupled sensor to sense the guided waves in the rail. Further Rose[29] proved that the guided waves are induced into the rail due to the wheel- rail interaction of the moving train. Accelerometers were used to at a distance of 2000mts away from the train to detect the guided wave at different positions of the rail.

But so far little work has been done for rail damage detection using environmental excited high frequency waves mainly the waves induced by the wheel-rail interaction (moving Hertzian contact) of the moving train. In chapter 2 these train induced guided waves are modeled using the semi analytical finite element(SAFE) method and the feasibility of these high frequency train induced waves for the use of damage detection is explained by calculating their decay rate.

1.2 Piezoelectric Impedance/admittance based structural health monitoring

1.2.1 Introduction

Piezoelectric materials acting in the direct manner produce an electrical charge when stressed mechanically. Conversely, a mechanical strain is produced when an electrical field is applied. The direct piezoelectric effect has often been used in sensors like a piezoelectric accelerometer. With the converse effect, piezoelectric materials apply localized strains and directly influence the dynamic response of the structural elements when either embedded or surface bonded into a structure. This converse effect is used in the piezoelectric impedance based structural health monitoring.

The piezoelectric attached or bonded to the structure is used as a both sensor and actuator in impedance based structural health monitoring. The basis of this active sensing technology is the energy transfer between the actuator and its host mechanical system. It has been shown that the electrical impedance of the PZT material can be directly related to the mechanical impedance of a host structural component where the PZT patch is attached [16]. Utilizing the same material for both actuation and sensing not only reduces the number of sensors and actuators, but also reduces the electrical wiring and associated hardware. Furthermore, the size and weight of the PZT patch are negligible compared to those of host structures so that its attachment to the structure introduces no impact on dynamic characteristics of the structure.

The application of impedance measurements to structure health monitoring has its theoretical development first proposed by Liang et al.[30] and subsequently developed by Chaudhry et al. [31], Park et al.[32-37], Giurgiutiu et al.[37-42_], Bhalla et al.[43&44], and Naidu et al.[45]. The method utilizes high frequency structural excitations, which are typically higher than 10 kHz through surface-bonded PZT patches to monitor changes in structural mechanical impedance. The PZT patches require very low-level voltage, typically less than 1 volt, to produce high frequency excitation in the host structure.

1.2.2 Modeling of impedance based methods

An electromechanical model which quantitatively describes the process is presented in Figure 1.11. The structure is modeled as a simple spring mass and damper system and the piezoelectric is attached to it. When the voltage is applied to the piezoelectric patch it will act as actuator and

make the structure vibrate and the same piezoelectric is used as a sensor to measure the impedance using impedance analyzer.
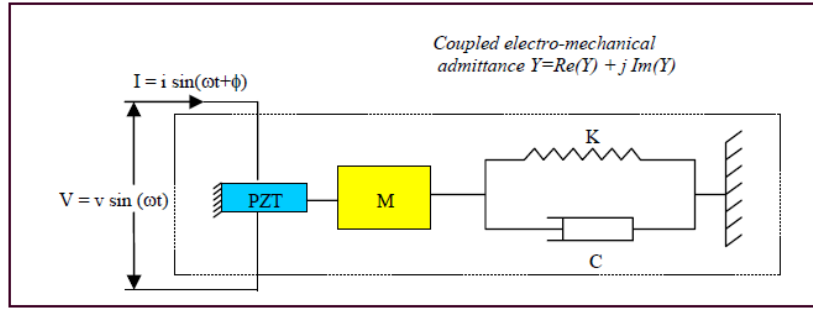
Figure 1.11 Electro mechanical model of piezoelectric impedance method [16]

Liang et al.[30] shows that the electrical admittance $Y(\omega)$, which is an inverse of the electrical impedance, of the PZT actuator is a combined function of the mechanical impedance of the PZT actuator $Z_p(\omega)$ and that of the host structure $Z(\omega)$

$$Y(\omega) = \frac{I}{V} = i\omega a\left(\varepsilon_{33}{}^T - \frac{Z(\omega)}{Z(\omega) + Z_p(\omega)} d_{3x} Y_{xx}{}^E\right) \qquad 1.1$$

where V is the input voltage to the PZT actuator, and I is the output current from the PZT, a, d_{3x} $Y_{xx}{}^E$ $\varepsilon_{33}{}^T$, are the geometry constant, piezoelectric coupling constant, Young's modulus, and complex dielectric constant of the PZT at zero stress, respectively.

Eq. 1.1 sets groundwork for using the PZT actuator for impedance-based structural health monitoring applications. Assuming that the mechanical property of the PZT does not change over the monitoring period of the host structure, Eq. 1.1 clearly shows that the electrical impedance of the PZT is directly related to the mechanical impedance of the host structure, allowing the monitoring of the host structure's mechanical properties using the measured electrical impedance. Consequently, any changes in the electrical impedance can be considered an indication of changes in the structural mechanical properties. It should be noted that the electrical admittance $Y(\omega)$ is primarily capacitive. In other words, the imaginary part of the admittance plays a dominant role. This imaginary part is more sensitive to the temperature variation than the real part because the dielectric constant $\varepsilon_{33}{}^T$ is temperature sensitive and it only affects the imaginary part. Therefore, the real part of the admittance (or impedance) is mainly used for monitoring in applications. The variation in the PZT electrical impedance over a

range of frequencies is analogous to that of the frequency response functions of a structure, which contains vital information regarding the health of the structure. Wang et al. [46] further extended the work done by Liang et al. [30] for the PZT stack actuators connected with structures at both sides, and checked their sensing and actuation ability in detail. The dependence of the electric admittance on the structural impedance is once again observed, which confirms a possibility of monitoring structural behavior by measuring the electric admittance of the PZT.

1.2.3 Parameters of the piezoelectric impedance method

1.2.3.1 Frequency Ranges

The sensitivity of the vibration-based NDE techniques in detecting damage is closely related to the frequency band selected. Stokes and Clouds[47] proved that to sense incipient-type damage, it is necessary for the wavelength of excitation to be smaller than the characteristic length of the damage to be detected. In order to ensure high sensitivity to incipient damage, the electrical impedance is measured at high frequencies in the range of 30 kHz to 400 kHz. Under this high frequency range, the wavelength of the excitation is small, and sensitive enough to detect minor changes in the structural integrity. The frequency range for a given structure is commonly determined by trial-and-error.

1.2.3.2 Real Part of Electric Impedance

As stated in the previous section, the real part of electric impedance is more reactive to damage or changes in the structure's integrity than the imaginary part[30&48]. The change in the structure's impedance is attributed to change in integrity of the structure due to damage. This characteristic is exhibited only in the real portion of the impedance as indicated in Eq. 1.1.

1.2.3.3 Sensing Region of Impedance Sensors

Under the high frequency ranges employed in the impedance-based method, the sensing region of the PZT is limited to an area close to the PZT sensor/actuator. The localized nature of the sensing region provides an advantage in that the impedance sensor is less sensitive to boundary condition changes or any operational vibrations, which usually affect lower-order global modes. Esteban[49] performed extensive numerical modeling based on the wave propagation theory to identify the sensing region of the impedance-based method. In general, the sensing range of an impedance sensor is closely related to the material properties of a host structure, geometry,

frequency ranges being used, and properties of PZT materials. Based on the knowledge acquired through various case studies, it has been estimated that the sensing area of a single PZT can vary anywhere from 0.4 m (sensing radius) on composite structures to 2 m on simple metal beams.

1.2.4 Damage metrics

The measured data like the impedance is processed to analyze the structure integrity. That is the current measured data has to be compared or correlated with the baseline measurements which are taken under no damage conditions to assess the damage in the structure unlike the instantaneous damage detection methods. There are various statistical damage metric methods to compare or correlate the data for the damage assessment like Root mean square deviation (RMSD), Mean absolute percentage deviation (MAPD), correlation coefficient (CC), covariance change (COV) and correlation coefficient deviation (CCD). Each of them has their own advantage like the RMSD and MAPD were found suitable for the characterizing the occurrence of the new damage while increase in the damage size over a fixed location can be analyzed by CC and COV. In most of the cases only Root mean square deviation damage metric (RMSD) is used because of its high sensitivity for the initial damage detection in structure[45]. The Root mean square deviation(RMSD) is taken for the real part of the impedance as shown in the Eq. 1.2 and based on this value the structure integrity is analyzed.

$$\text{RMSD} = \frac{\sqrt{\sum_1^n (\text{Re}(Z_i) - \text{Re}(Z_d))^2}}{\sqrt{\sum_1^n \text{Re}(Z_i)^2}} \qquad 1.2$$

Where $\text{Re}(Z_i)$ the real part of the impedance Z_i measures at the initial condition that when the structure is in pristine condition, $\text{Re}(Z_d)$ is the real part of the impedance Z_d measured when the structure is in damaged condition and *n* denotes the number of frequency point over the frequency range.

1.2.5 Procedure of piezoelectric impedance based damage detection

A piezoelectric path is bonded to the structure and the impedance of the damage structure is measure using the impedance analyzer over a certain range of the high frequency. The measure impedance is compared to the reference impedance measured when the structure is in good condition. The Figure 1.12 shows how the measure impedance signature under damaged condition varies over the reference impedance signature measured in good condition. These

impedance signatures are analyzed using any of the damage metrics explained in the above section depending on the type of damage assessment. If the damage metric value is significantly high over the threshold value then the structure is indicated as damaged[41&42].
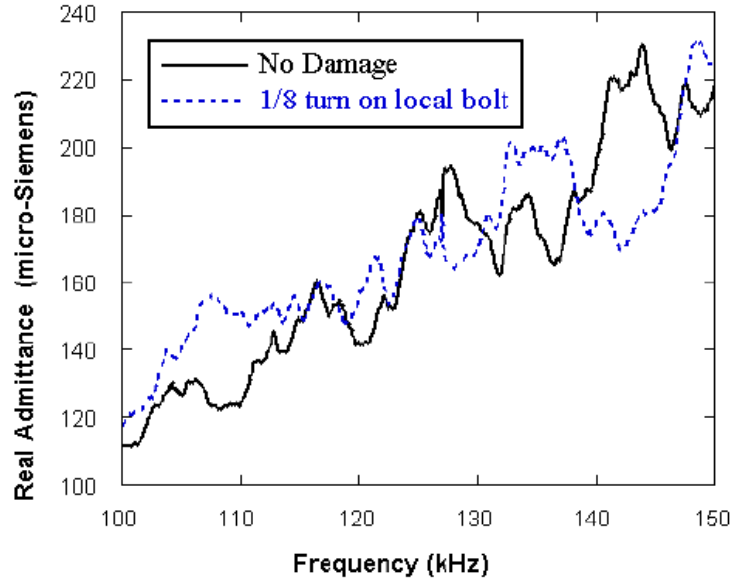
Figure 1.12 Impedance signatures after damage and before damage [41]

1.2.6 Low cost impedance based methods

Impedance based structural health monitoring is very expensive because of the impedance measuring devices like the impedance analyzers. Also they are heavy and occupy more space, hence the piezoelectric impedance methods are difficult to implement for the on-field damage detection. Recently Peairs et al.[17] have proposed some low cost impedance based methods. The piezoelectric patch bonded to a structure is attached with a resistive circuit and the voltage across the resistance is measured to calculate the impedance of the total circuit as shown in the Figure 1.13. The voltage across the resistance will be very small because low input voltages are used to the piezoelectric actuator to excite the high frequency vibration in the structure. An amplifying circuit is used to amplify the voltage across the resistor.
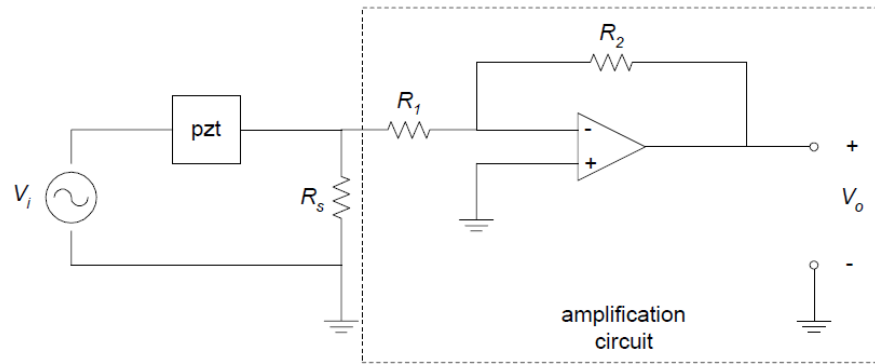
Figure 1.13 Low-cost resistive circuit for impedance measurement [17]

Figure 1.14 shows the other type of low cost impedance based method using the transfer impedance method proposed by Bhalla[48]. The structure is actuated using one piezoelectric and the other piezoelectric is used as a sensor and the voltage is measured across it. This method only needs a signal generator and a signal analyzer.
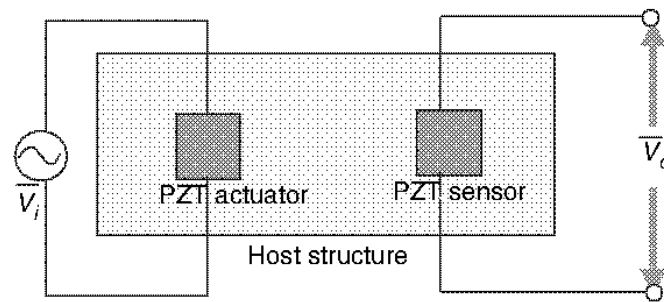
Figure 1.14 Low-cost Transfer impedance method [48]

1.2.7 Instantaneous damage detection impedance based methods

In the conventional piezoelectric impendence based methods the measured impedance of the structure is compared with that of the reference impedance taken when the structure is in good condition. Since the reference data and the measured data may not be measured at the same environmental condition and also the structure properties might change because of it usage (may not be because of the damage) the measured data will be different from the reference data and this leads to wrong assumptions. Recently Inman et al.[50] using an array of piezoelectric patches and Kim and Sohn [51&52] using the polarizing characteristics of the piezoelectric and transfer impedance method has developed some instantaneous piezoelectric impedance based damage detection.

1.2.8 Piezoelectric Impedance methods for railway structural health monitoring

This piezoelectric based impedance method is applied for the structural health monitoring of rails by Inman et al.[53]. Experiments were conducted on a 2 meter long rail shown in Figure 1.15(a). The localized damage was simulated using magnets and C-clamps as shown in Figure 1.15(a). The root mean square deviation(RMSD) damage metric is used to assess the measured impedance signatures over the frequency range.
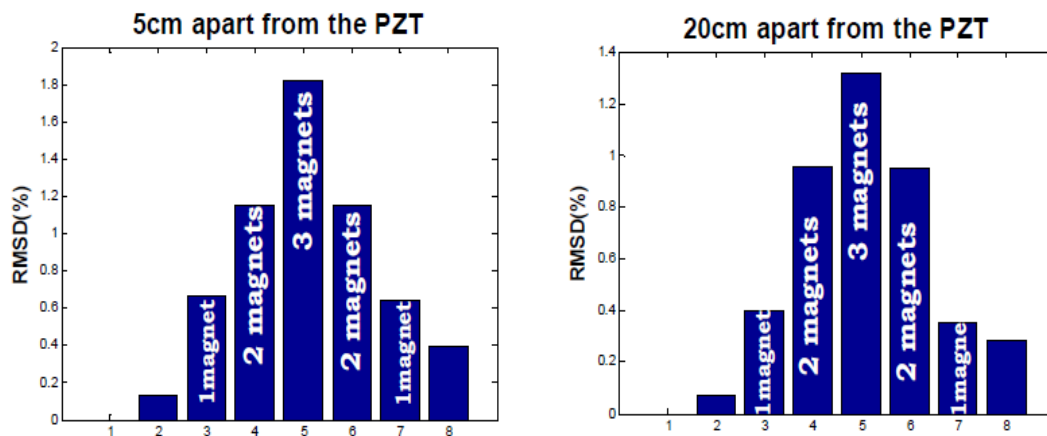
Figure 1.15 a) Application of impedance damage detection methods for rail and b) Root mean square deviation for magnets as damage [53]

The conclusions made from the experiments performed are, the method can detect damage in the entire length of the provided 1.42m sample rail. However, no relation has been established between the RMSD value and the PZT / magnet distance due to the short length of the sample rail. Various ranges of the frequencies were used and concluded that the best range of the frequency is dependent on the type of damage.

1.3 Railroad energy harvesting

1.3.1 Piezoelectric based railroad energy harvesting

Few researches looked into harvesting power from the railroad track using piezoelectric materials. An Israeli company Innowattech[54] is one of them. They replaced the railroad steel tie plates which are placed at the interface of the sleeper and the rail with piezoelectric pads as shown in Figure 1.16. These piezoelctric pads are replaced over a certain range of the railway track and all these pads are connected in series. When the loaded train pass by, the track will undergo stresses due to the loads exerted by the train wheels. These stress are applied directly on the piezoelctric tie pads and generate the volatge due to the propert of the piezoelctric material. The power generated is in the form pulses, that is peak voltage is generated when the train wheel are exactly under the tie plate.

Figure 1.16 Piezoelectric rail pads [54]

Innowattech also atatched piezoelectrci layers to the rails at different positions like under the rail head, over the rail base and on the sides of the rail flange as shown in the Figure 1.17 [55]. The rail will have huge stress when the loaded train moves on it. The rail will undergo different stresses at different positions. These stesses will be transmitted directly to the piezoelectric layers attached to the rail at various positions and the piezoelctric layers will generate volatge. In this case the piezoeclctric enery is also generated from other reasons like compression and elongation caused due to noise, as well as the thermal stresses caused by environmental temperature variations of the rail.

Figure 1.17 Piezoelectric adhered to rail [55]

All these piezoelectric pads and the layers attached to the rail and the railroad are connected to each other in series over a range of the railway track and the total energy is stored in the road side battery recharging stations.

Further Nelson[11] also looked into the piezoelectric based railway energy harvesting. They followed the similar way as of Innowattech by attaching the piezoelectric to the rail base as shown in Figure 1.18. They also conducted the on-field experiments to estimate the energy generated. The Figure 1.18(b) shows that the generated energy is in the order of milliwatts, which is only sufficient to power the structural health monitoring sensors.
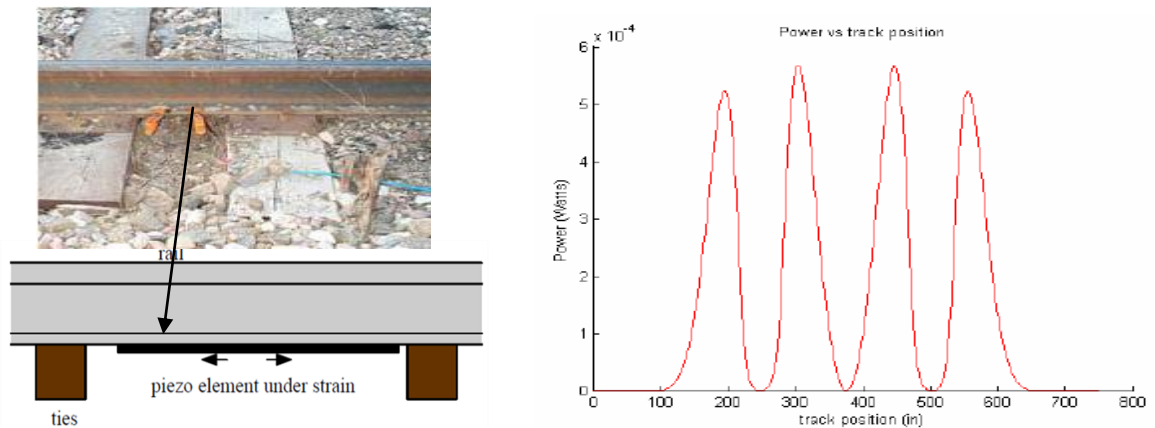
Figure 1.18 a) Piezoelectric energy harvesting on field rail and b) Power generated due to the strain induced by train (milliwatts) [11]

1.3.2 Electro-magnetic generator based railroad energy harvesting

Since the piezoelectric based energy harvesting from railroad can only harvest power in the order of milliwatts which is sufficient to power the structural health monitoring sensors, but not the track side electric infrastructure, later Nelson [12] used a rotational electromagnetic generator to harvest energy from rail road as shown in Figure 1.19(a). This is an adaptation of conventional rack & pinion based vibration energy harvester to the railway track vibrations. In this the rack and pinion will convert the irregular linear vibrations into irregular rotational oscillatory motion and the rotational generator is driven by this rotational oscillation. Hence the power produced is also irregular as show in Figure 1.19(c). Detailed explanation of the disadvantages of these conventional rotational vibration energy harvesters is explained in chapter 5.

This conventional rotational vibration energy harvester prototype for railway application is shown in the Figure 1.19(b). The rack is grounded into the soil to certain depth. The whole system is placed on a mounting plate and the plate is bolted to the two sleepers as shown in Figure 1.19(a). When the loaded train passes by the track will vibrate vertically and drive the harvester to produce energy. The vertical displacement of the track at a sleeper is maximum,

only when the train wheel is directly under it, when the wheel is offset to the sleeper the displacement will be minimum almost zero. Hence the harvester is driven only when the train wheel passes by it and the power is produced only at that time. The track vibration is like a pulse because the train wheels are far apart to each other. The power produced by this conventional harvester from the railway track vibrations is like a pulse and the average power is very low in the order of 0.5Watts as shown in Figure 1.19(b).
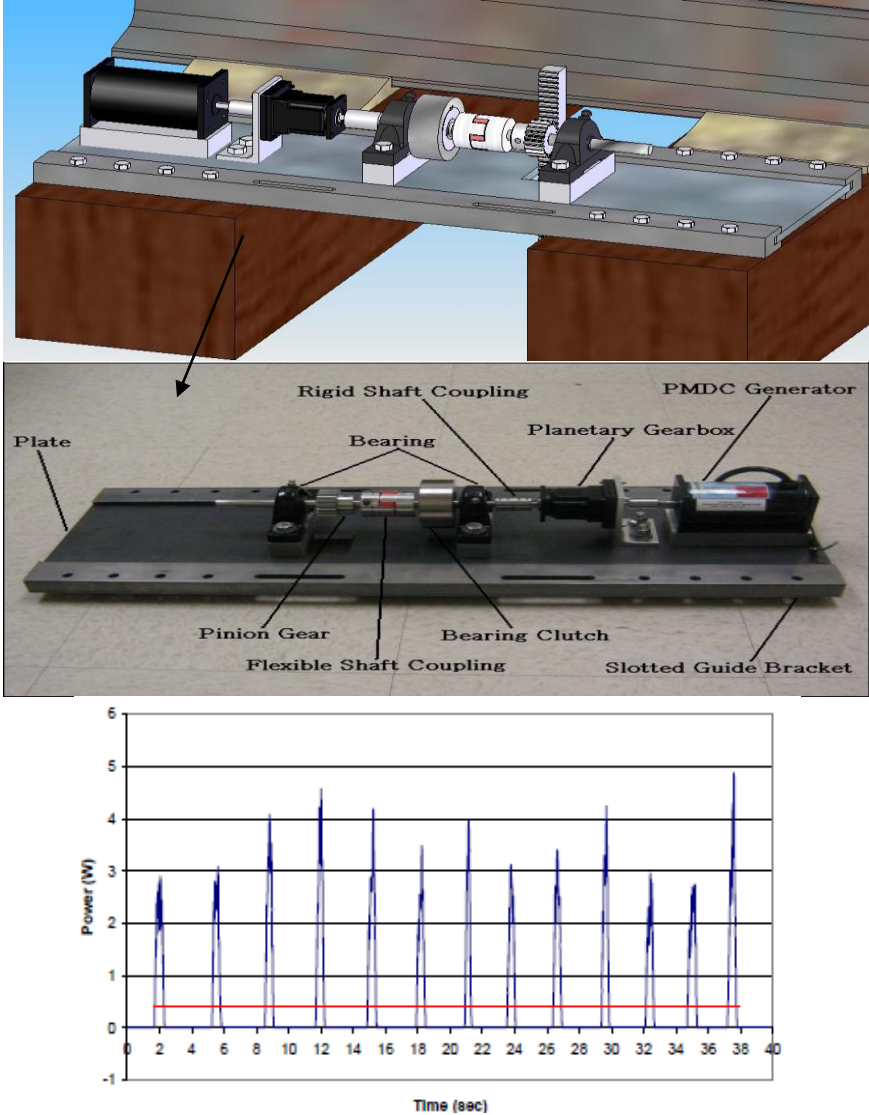
Figure 1.19 a) Electro-magnetic based railroad energy harvesting b) Prototype of the rotational harvester c) Power harvested by the harvester (avg-0.5Watts) [12]

19

1.3.4 Other types of railroad energy harvesting

Apart from piezoelectric and rotational electromagnetic energy harvesting methods, a very few other types of railroad energy harvesting methods are also invented. Zahid.F.Mian[56] generated power by placing an electromagnetic coil near the rail as shown in Figure 1.20. When the train wheel passes by, the coil will generate electricity just because the moving wheel will change the magnetic flux around the coil. The high permeability of steel wheel will allow the magnetic flux to pass by and the rate of change of flux depends on the velocity of the wheel. This method can only generate only in the order of very few milliwatts.
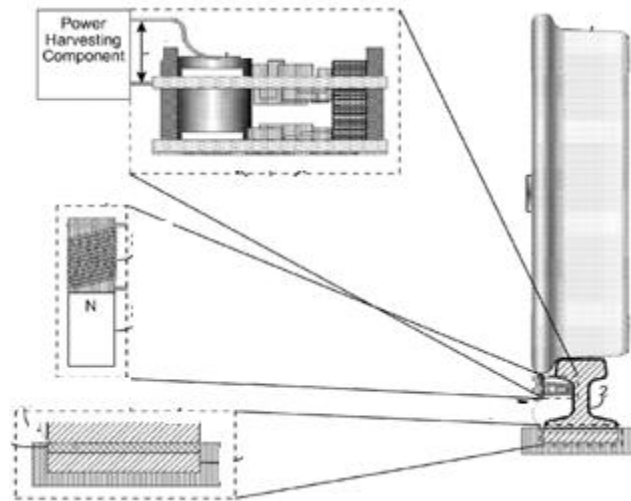
Figure 1.20 Magnetic coil based railroad energy harvesting [56]

Nelson et al.[57] also used an inductive voice coil device to harvest energy from railroad. The inductive voice coil device is placed on the side of the rail as shown in the Figure 1.21. The inductive coil is like an electromagnetic coil when the magnet inside the coil oscillates, voltage is produced. As shown in Figure 1.21 the inductive coil magnet is moved due to the vertical displacement of the rail caused by the moving train. The link is attached to the rail web (maximum displacement point in the rail) in order to have the maximum displacement. Thus the inductive coil magnet is directly driven by vertical rail displacement caused when the loaded train passes by.
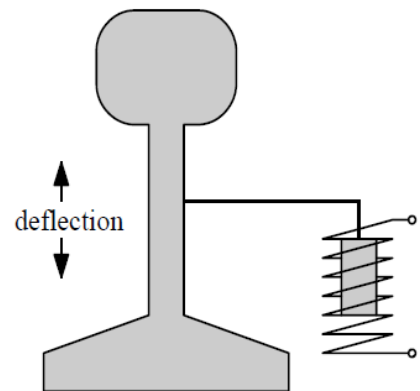
Figure 1.21 Inductive coil attached to rail [57]

Chapter 2 - Analysis of Train induced guided waves in rails

2 Introduction

Conventionally specific actuators are required for ultrasonic high frequency wave based rail damage detection methods like ultrasonic and guided wave[2-10]. A great deal of energy is imparted to the railroad track through the moving wheel-rail interaction Hertzian contacts, which lead to elastic waves that can propagate miles beyond the actual train[15]. In this chapter we present the analysis of train-induced waves and their propagation along the rail by taking account of the Hertzian contacts and moving load. Semi analytical finite element and mode superposition methods are used for the modeling. The analysis is compared with the experimental results in literature. The feasibility to use train induced waves for the long range damage detection in the rail is explained by calculating their decay rate.

2.1 Wavenumber finite element analysis of the rail

The conventional FE method has several drawbacks for the high frequency guided wave modeling in rails application, it requires very large models for the high frequency analysis and so the computation becomes cumbersome. For the analysis of the high frequency waves we need to take at least 10 nodes for the each wavelength, since the wavelength is very small it is not easy to do that in the conventional FE methods. To overcome these difficulties, an improved numerical method called wavenumber finite element (WFE) method or semi analytical finite element (SAFE) method [19] is employed. The main advantage of this method is it reduces the three dimensional analysis to two dimensional one and reduces lot of computational effort. Using this method the different wave types are readily identified and can be analyzed, which helps in interpretation of the wave propagation in the structure under investigation.

The wave propagates in an elastic structure like rail which is assumed to be infinitely long in x direction and uniform in cross-section. The solution of the propagation of waves in all directions can be modeled using WFE method without making a finite element mesh in the propagation direction (x-direction). The detailed theoretical modeling of semi analytical finite element analysis is explained below.

Equations of motion for the cross-section are formulated by inserting the kinetic, potential or strain energies and work done by external traction forces into Hamilton's equation

$$\int_{t_1}^{t_2} \delta U + \delta T - \delta W = 0 \qquad 2.1$$

Where $\quad \delta U = \int_T \delta u^T t\, dT;\ \delta T = \int_V \delta u^T \rho \ddot{u}\, dV\ and\ \delta W = \int_V \delta \epsilon^T C\, \epsilon$

The upper script T means a transpose vector and V is the volume, C is the Young's modulus in the direction of x and ρ is the density of the material
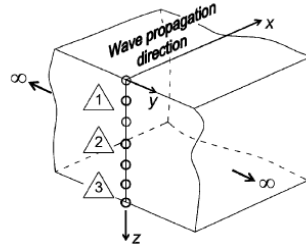
Figure 2.1 Wave propagation direction

The strain vector is given as

$$\epsilon = \left[L_x \frac{\partial}{\partial x} + L_y \frac{\partial}{\partial y} + L_z \frac{\partial}{\partial z} \right] u \qquad 2.2$$

$$L_x = \begin{bmatrix} 1 & 0 & 0 \\ 0 & 0 & 0 \\ 0 & 0 & 0 \\ 0 & 0 & 0 \\ 0 & 0 & 1 \\ 0 & 1 & 0 \end{bmatrix} \quad L_y = \begin{bmatrix} 0 & 0 & 0 \\ 0 & 0 & 0 \\ 0 & 0 & 1 \\ 0 & 1 & 0 \\ 1 & 0 & 0 \\ 0 & 0 & 0 \end{bmatrix} \quad L_z = \begin{bmatrix} 0 & 0 & 0 \\ 0 & 1 & 0 \\ 0 & 0 & 0 \\ 0 & 0 & 1 \\ 0 & 0 & 0 \\ 1 & 0 & 0 \end{bmatrix}$$

The displacement is assumed harmonic along the propagation direction x, and the interpolation functions are used to describe its amplitude in the all the directions.

$$\boldsymbol{u}(x,y,z,t) = \begin{bmatrix} u_x\,(x,y,z,t) \\ u_y\,(x,y,z,t) \\ u_z\,(x,y,z,t) \end{bmatrix} = \begin{bmatrix} U_x(y,z) \\ U_y(y,z) \\ U_z(y,z) \end{bmatrix} e^{i(\vartheta x - \omega t)} \qquad 2.3$$

Where t is time, y and z denotes coordinates of the cross-section, ω is the frequency, ϑ is the wavenumber and i is the imaginary unit.

The displacement expressions in Eq. 2.3 over the element domain can be written in terms of the shape functions, $N_k(y,z)$, and the nodal unknown displacements, (U_{xk}, U_{yk}, U_{zk}), in the x, y and z directions

$$u(x,y,z,t) = \begin{bmatrix} \sum_{k=1}^{n} N_k(y,z)U_{xk} \\ \sum_{k=1}^{n} N_k(y,z)U_{yk} \\ \sum_{k=1}^{n} N_k(y,z)U_{zk} \end{bmatrix} e^{i(\vartheta x - \omega t)} = N(y,z)q^e e^{i(\vartheta x - \omega t)} \qquad 2.4$$

$N(y,z)$ is the shape function matrix of the element and q^e is the displacement vector for all the nodes in all three directions.

The strain vector for the element is given as

$$= \left[L_x \frac{\partial}{\partial x} + L_y \frac{\partial}{\partial y} + L_z \frac{\partial}{\partial z}\right] N(y,z)q^e e^{i(\vartheta x - \omega t)} \qquad 2.5$$

$$= (B_1 + i\vartheta B_2)q^e e^{i(\vartheta x - \omega t)} \qquad 2.6$$

$$B_1 = L_y N_y + L_z N_z \quad B_2 = L_z N$$

The strain energy for an element is

$$\int_{V_e} \delta\epsilon^{eT} C \epsilon^e dV_e \qquad 2.7$$

$$\int_{V_e} \left(\delta q^{eT}(B_1^T - i\vartheta B_2^T)e^{i(\vartheta x - \omega t)^*}\right)C^e\left(q^e(B_1 + i\vartheta B_2)e^{i(\vartheta x - \omega t)}\right)dV_e \qquad 2.8$$

$$\int_{A_e} \delta q^{eT}(B_1^T - i\vartheta B_2^T)C^e(B_1 + i\vartheta B_2)q^e dA_e \qquad 2.9$$

$$\delta q^{eT}\left[\int_{A_e}(B_1^T C^e B_1 - i\vartheta B_2^T C^e B_1 + i\vartheta B_1^T C^e B_2 + \vartheta^2 B_2^T C^e B_1)dA_e\right]q^e \qquad 2.10$$

The kinetic energy for an element is

$$\int_{V_e} \delta u^{eT}\rho \ddot{u}^e dV_e = -\omega^2 \delta q^{eT}q^e \int_{A_e} N^T \rho N \ dA_e \qquad 2.10$$

The traction force vector on the element is

$$t^e = NT^e e^{i(\vartheta x - \omega t)} \qquad 2.11$$

Work done on the element is derived by substituting Eq. 2.11 in work done element in Eq. 2.1

$$\int_{V_e} \delta u^{eT} t^e dV_e = \delta q^{eT} \int_{V_e} N^T N T^e \ dV_e \qquad 2.12$$

By substituting the strain, kinetic energy and work done in Eq. 2.1 we get the equation of motion for the element

$$\int_{t_1}^{t_1} \left\{ \bigcup_{e=1}^{n_e} \delta q^{eT}[K_1{}^e + i\vartheta K_2{}^e + \vartheta^2 K_3{}^e - \omega^2 M^e]q^e - \delta q^{eT}f^e \right\} dt = 0 \qquad 2.13$$

Where $K_1{}^e = \int_{A_e} B_1{}^T C^e B_1 dA_e$; $K_2{}^e = \int_{A_e}(B_1{}^T C^e B_2 - B_2{}^T C^e B_1)dA_e$; $K_3{}^e = \int_{A_e} B_2{}^T C^e B_1 dA_e$

$$M^e = \int_{A_e} B_1{}^T C^e B_1 dA_e \text{ and } f^e = \int_T N^T N T^e dT$$

By making the equation global considering all the finite elements in the cross section

$$\int_{t_1}^{t_1} \{\delta W^T[K_1 + i\vartheta K_2 + \vartheta^2 K_3 - \omega^2 M]W - \delta W^T f\} = 0 \qquad 2.14$$

$$[K_1 + i\vartheta K_2 + \vartheta^2 K_3 - \omega^2 M]\overline{W} = f \qquad 2.15$$

Where K_1 and K_3 are global stiffness matrix related with the cross-section strain deformation and the out of plane deformation, and K_2 is a global stiffness matrix related to both. M is the mass matrix of the cross section, and $\overline{W}$ is the global displacement vector for all directions. All the matrices are constants and real if the material damping is not considered.

For finding the wavenumbers and the mode shapes in the equation of motion in Eq. 2.15 has to be solved by considering the external force as zero which gives

$$(K_1 + i\vartheta K_2 + \vartheta^2 K_3 - \omega^2 M)\overline{W} = 0 \qquad 2.16$$

The above differential equation of motion is expressed in terms of wave number and is in the form of an eigenvalue problem. This is solved for finding the various wave numbers ϑ at particular frequencyω.

2.2 Track model

In this study a typical US rail 115-lb A.R.E.M.A.[60] is modeled as an isotropic material. Since the rail has a complex geometry finer mesh is created in order to achieve the better results. Also the finer mesh on the top of rail head is necessary to give the proper force excitation to the nodes. The triangular mesh is generated using the Matlab's pde tool box. The total cross section of the

rail is divided in to 473 triangles and 291 nodes are generated. The finite element mesh used for the analysis is shown in Figure 2.2.
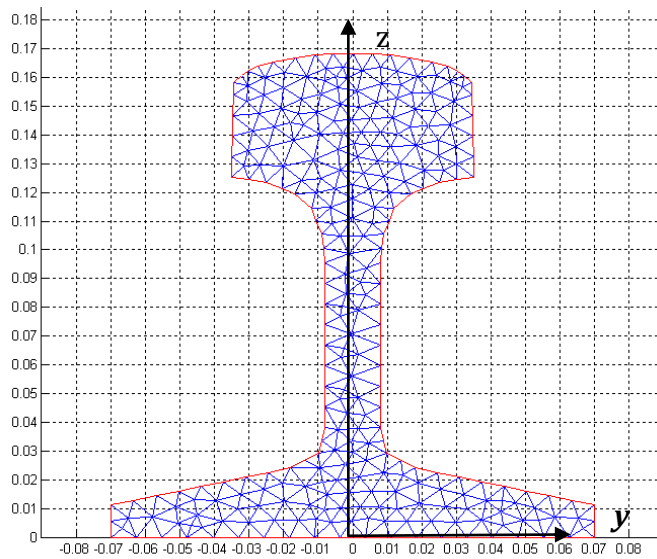
Figure 7.2 Rail Element Mesh (unit in meter)

2.2.1 Validation of the modelling

The above track model is used for analyzing the train induced guided waves in rails. Before extending the model to analyze the train induced guided waves in rail the modeling is validated by generating the dispersion curves and phase velocity of the guided waves upto 100kHz shown in Figure 2.3 and these are compared with that of the literature[19&20]. The results look the same and hence the model is correct and used to analyze the train induced elastic waves using the wheel rail interaction as moving Hertzian contacts.
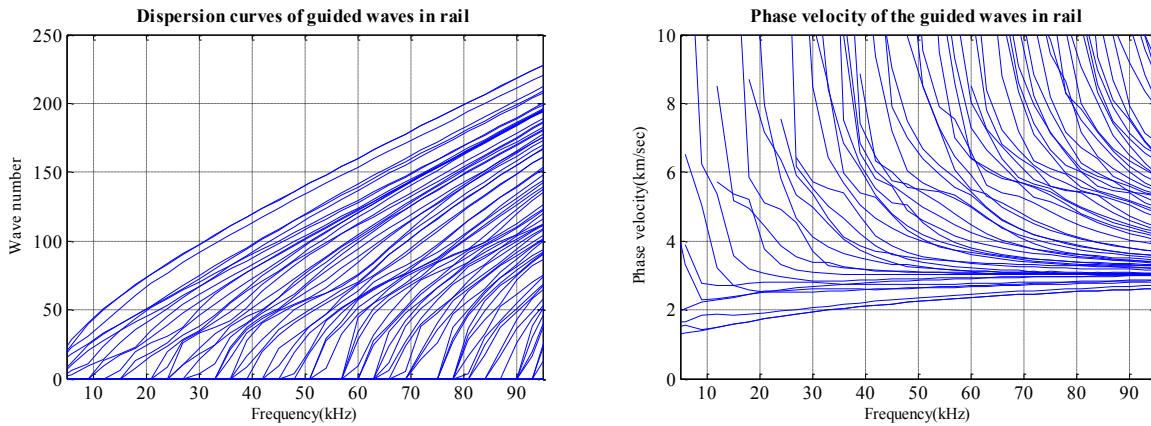
Figure 2.8 a) Dispersion curves and b) phase velocity in rails

25

2.3 Analysis of train induced elastic waves using Hertzian contacts

In this section the analysis of the train induced waves is modelled as static hertzian contact stress first, and then moving hertzian contact is considered..

2.3.1 Wheel-rail Hertz contacts

The strsses due to the wheel rail interaction is modelled using hertz conact stesses. According to the Hertzian contact theory the conatct area of the wheel is in eleptical shape with a major semi axis a and a minor semi axis b. the conatct pressure distribution in this eleptical area can be expressed as [61&62]
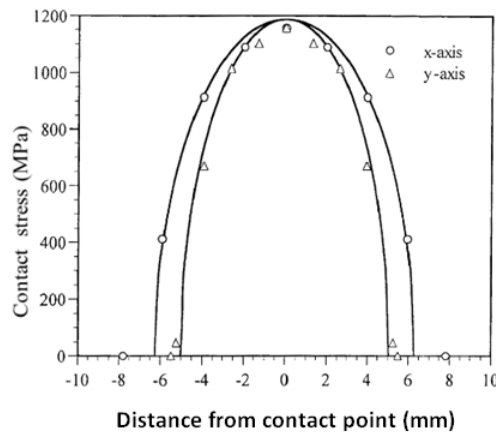
Figure 2.4 Force distribution of Hertzian contact on the rail head in x and y direction [61]

$$p = p_0 \sqrt{1 - \left(\frac{x}{a}\right)^2 - \left(\frac{y}{b}\right)^2} \qquad\qquad 2.17$$

Where p_0 is the maximum conatct pressure at the initial contact point. It can be obtained from

$$p_0 = \frac{3}{2}\left(\frac{F}{\pi ab}\right) \qquad\qquad 2.18$$

Where F is the applied force in the normal direction. The major axis extends along the rail longitudinal direction and the minor axis is in transverse direction. The magnitudes of a and b depends on the normal load, profiles and wheel and rail materials [62].

The conatct pressure distributions of the wheel rail interaction is taken from literature [61], as shown in the Figure 2.4 for fully loaded case. The major and minor semi axes are $a=6mm$ and

b=5mm. This figure gives the exact distribution of the forces in the rail due to the wheel, these force distribution is used in this paper for the analysis of the hertzian contact induced elastic waves.

2.3.2 Analysis of the elastic waves due to static Hertzian contacts

The equation of motion discribed in Eq. 2.16 is sufficient for giving the different mode shapes for the unforced guided waves . For the forced guided wave the motion Eq 2. 15 can be writen as

$$(A - \vartheta B)Q = f \qquad 2.19$$

$$A = \begin{bmatrix} 0 & K_1 - \omega^2 M \\ K_1 - \omega^2 M & iK_3 \end{bmatrix} \quad B = \begin{bmatrix} K_1 - \omega^2 M & 0 \\ 0 & -K_3 \end{bmatrix} \quad Q = \begin{bmatrix} \bar{W} \\ \vartheta \bar{W} \end{bmatrix} \quad f = \begin{bmatrix} 0 \\ f_n \end{bmatrix}$$

Where f_n is the nodal force given to the nodes on which force is excerted. This equation can be solved as a standard eigenvalue problem for the forced ocillations. The displacement equation of guided wave for the harmonic force at a specific frequency is given in superposition, as a summation of the response due to different modes existing at that frequency [19]. This equation is shown below.

$$\bar{W} = \sum_{m=1}^{M} -\frac{\bar{W}^l f}{B_m} \bar{W}^{r,up} e^{\{i\vartheta_m(x-x_s)\}} \qquad 2.20$$

Where $B_m = \bar{W}^l B \bar{W}^r$, $\bar{W}^l$ and $\bar{W}^r$ represent the left and right eigen vectors, $\bar{W}^{r,up}$ represents the upper part of the right eigen vector $\bar{W}^r$, x_s is the location of the excitation source and x is the location where the response is calculated.

The analysis is extended to include the Hertzian contact, by considering a multi-point conatct forces distributed in both x and y direction according to Figure 2.4. A broad sprectrum of guided waves will be excited due to these multipont excitations of the Hertzian contact. This will lead to the superposition of the waves which intern lead to a different combinations of modes. The dispalacement due to the a harmonic hertzian conatct forces can be expressed as the superposition of the different modes excited due to contact forces at different location $x_{s,n}$. The Eq. 2.21 represents the displacement.

$$W = \sum_{n=1}^{N} \sum_{m=1}^{M} -\frac{\overline{W}^l f}{B_m} \, \overline{W}^{r,up} \, e^{\{i\vartheta_m(x-x_{s,n})\}} \qquad\qquad 2.21$$

Where N is the number of points in x direction cosidered in the rail due to Hertzian conact. And the force distribution in y direction has been considered in the node force vector f_n.
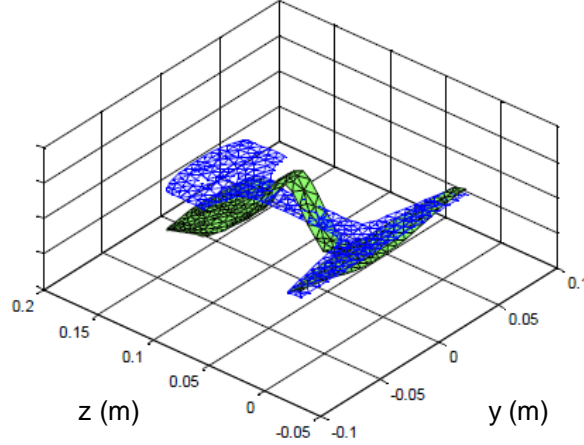
Figure 2.5 Displacement response due to static Hertzian contact at 30 KHz

Figure 2.5 shows of the displacement response in the rail at 30 KHz obtatined by modelling the Hertzian conatct force with 11 disribution points in x direction. The hertzian conatct forces are given to the specific nodes at the top of the rail in the f matrix in the vertical direction of the rail. Each point excitation will give 20 different modes of which 10 are lateral, torisional and assymetric longitudinal waves, and remaining 10 are vertical and symmetric longitudinal waves. The response plotted in the Figure 2.5 is for a distance of 1 metre away from the mid point of the wheel rail interatction.

Futher looking into the responses we find that the Hertzian conatct will make difference only at high frequency when the wavelengh smaller than twice of the Hertzian conatct.

2.3.3 Analysis of the elastic waves due to moving Hertzian contacts

The train induced elastic waves is then analyized by considering the moving hertzian contact usingthe Doppler effect concept. The frequencies of the excited waves are revised acordingly, and the wavenumber in the Eq. 2.19 should be revised as

$$\hat{\vartheta}_m = \left\{\vartheta_m + \left(\frac{V_{s,r}}{\omega}\right)\vartheta_m^2\right\} \qquad\qquad 2.22$$

28

Where $\hat{\vartheta}_m$ and ϑ_m are the m-th wavenumbers of the cases of moving and static contacts, respectively., ω is the frequency at which the wave is excited, and $V_{s,r}$ is the train velocity. The displacement Eq 2.21 will be changed into

$$\overline{W} = \sum_{n=1}^{N} \sum_{m=1}^{M} -\frac{\overline{W}^l f}{B_m} \overline{W}^{r,up} e^{\{i\,\hat{\vartheta}_m(x-x_{s,n})\}}$$ 2.23
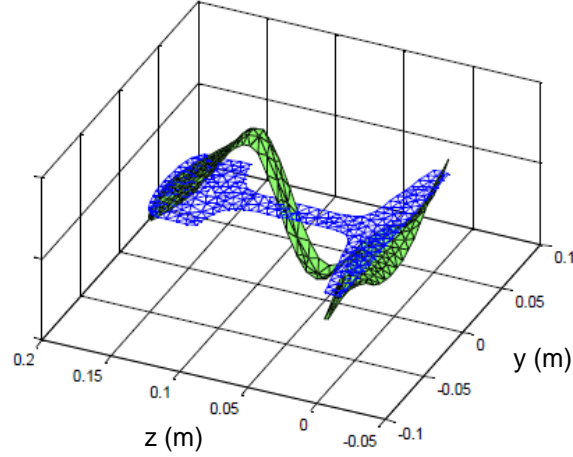
Figure 2.6 Displacement Response due to moving Hertzian contact at 30KHz

The displacement response plotted in Figure 2.6 is plotted for a train of 112 mph (50m/sec)at a distance away from 1metre from the mid point of the wheel rail conatct.

Comparing the response of the static Hertzian conatct case in Figures 2.5&2.6, the moving hertzian conatct (due to train motion) gives quite different response in the rail at this frequency. This is because of the change in wave number and different superposition of the waves.

2.4 Comparison of results

In order to check the validation of our analysis, we compare the simulation with the experimental results from literature. In the references [21&22] horizontal accelerations measured at three different portions of the rail like side of or under the rail head and middle of the web, are shown in Figure 2.7(b). The acceleration were plotted for the points located at such positions of the rail based on our analysis for the same train speed 34m/sec, as shown in Figure 2.7(a). For middle and high frequency the trend of analysis matches well with the experimental results, and we also predict that at acceleration at 35-45 kHz and 60-70 kHz is large. Below 3KHz the trend does not

29

match well, the reason is there will be additional excitation due to the wheel/rail rolling contact at low frequencies [14], which is not consider in the modeling.
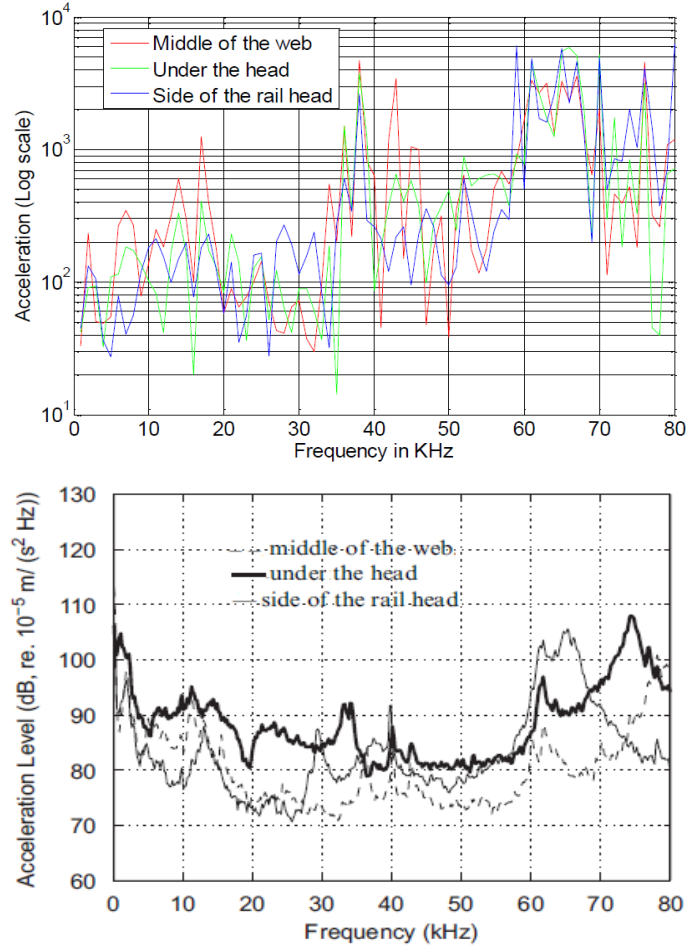
Figure 2.7 Horizontal accelerations of the rail induced by moving train: (a) our analysis. (b) Experimental measurement in reference [22]

2.5 Feasibility for damage detection

These train induced elastic waves have been observed travel very long distance along the rail depending on their damping [22]. The two types of damping losses that contribute for the damping is material damping or hysteresis damping and acoustic damping caused due to acoustic emission along the propagation. The decay rates for a wave can be calculated by its attenuation factor. The generic wave equation for the displacement is given as $A_0 e^{-\alpha x} e^{-i\beta x}$ where α is the attenuation factor and β is the phase change. Comparing this generic equation with the guided

30

wave displacement equation given in Eq. 2.21 we get the attenuation factor is the imaginary part of the wave number $I_m(\vartheta)$.
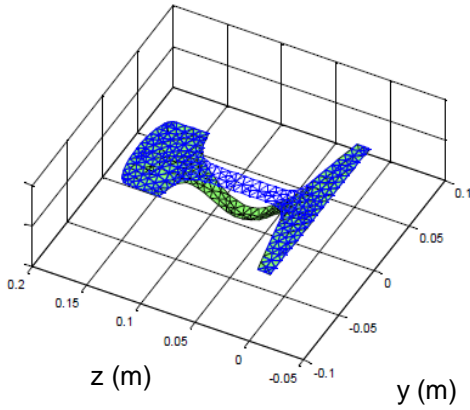
Figure 2.8 Mode shape of wave number 91.4 at 30 kHz
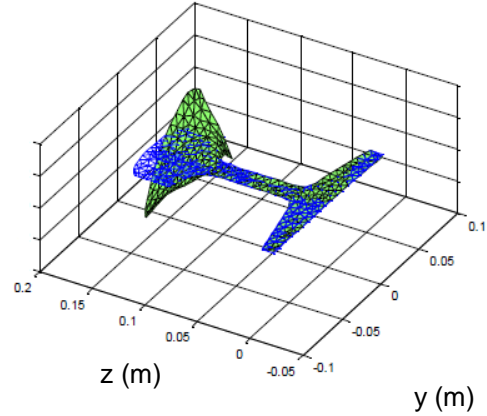
Figure 2.9 Mode shape of wave number 70.46 at 30 KHz

The wave number can be approximated by the Taylor series as $\vartheta_d = \vartheta + \frac{\partial \vartheta_d}{\partial \eta}\eta$ where ϑ and ϑ_d are the undamped and damped wavenumbers. Based on this equation the imaginary part of the damping wavenumber is given by the Eq. 2.24.

$$I_m(\vartheta_d) = \frac{\omega \eta}{2 c_g} \qquad\qquad 2.24$$

Where c_g is the group velocity given by

$$\frac{W^l(i K_2 + 2\vartheta K_3)W^r}{2\omega W^l(M)W^r} \qquad\qquad 2.25$$

This wave attenuation factor is used in calculating the decay rates of the different wave modes. As an example Figures 2.8&2.9 are plotted for two different modes that exist at 30 KHz at wavenumber 91.4 and 70.46. A special feature of these two modes is that they have mode displacement only at the rail head and web but not in rail foot. The decay rates of these modes calculated using Eq. 2.24 are 0.1152dB/m and 0.0275dB/m respectively, for damping loss factor of 0.0002. This calculated decay rates show that mode at wave number 91.4 diminishes faster than the mode of wave number 70.46. Based on the decay rates of the modes, different modes may be used to detect the damage in different parts of the rail. Though there exist a broadband of modes due to the moving Hertzian contact there will be only certain modes available at

31

particulate distance due to different decay rates, hence damage detection may be done based on these modes.

2.6 Conclusion

This chapter presents the analysis of the elastic waves induced in the rail due to wheel rail interaction of the moving train. Semi-analytical finite element and mode superposition methods are adapted to take the Hertzian contacts between wheel and track. Doppler Effect is used to interpret the influence of moving load/train. The analysis results are compared with experiments in literature, and the trend matches well. The analysis shows the acceleration is of broad spectrum with relatively high amplitude around 40 KHz and 65 KHz. The moving load has significant influence to the responses in the rail. This analysis also helps in understanding the feasibility of train induced elastic waves for the damage detection in the rail.

Chapter 3 - Sensitivity enhanced low-cost admittance based damage detection

3 Introduction

In the previous chapter long range damage detection methods of rails using guided waves generated from the wheel-rail interaction is analyzed. The long range methods like guided wave based methods are not suitable for damage detection in a bolted joint or a welded joint of rails. Hence a localized damage detection method has to be used for the joints. Piezoelectric impedance-based methods have been effectively employed in a variety of localized damage detection and structural health monitoring applications[32-42]. The mechanical impedance of the host structure is explicitly associated with the local structural properties, the change of the local properties upon the occurrence of structural damage can cause magnitude changes and frequency shifts in the measured impedance response[31]. This impedance based method is only used in detecting the localized damage detection. This idea has been exploited to detect small size localized crack in various structures[31-42]. The conventional impedance based methods are of high cost and huge in size due to the heavy impedance analyzers and are difficult to implement in fields[16]. But it gained more importance in the recent times because if it's easy implementation and integration with embedded systems using low cost impedance measuring circuits[17,48,64&65].

In this chapter low cost admittance (inverse of impedance) based damage detection methods are analyzed. A new inductive higher order circuits integrated to the structure are explored for localized damage detection. The inductance circuit parameters are optimized to enhance the sensitivity of the damage metric (root mean square deviation of the admittance change). First the existing low cost resistive circuit method is explained and later by modeling the piezoelectric attached structure the inductive circuits are analyzed and the optimized.

3.1 Impedance/admittance measurement with resistive piezoelectric circuit

The electrical impedance of the bonded PZT is equal to the voltage applied to the PZT divided by the current through the PZT. An approximation of the impedance is generated by taking the ratio with the FFT analyzer of the voltage supplied to the circuit, V_i, to the voltage, V_o, across a

sensing resistor, R_s, in series with the PZT as seen in below Figure 3.1. This circuit can be recognized as a voltage divider. The output voltage is proportional to the current through the sensing resistor, which, if the sensing resistor is small (less than 200Ω), is approximately the current through the PZT if the sensing resistor was not included (as when measuring with a normal impedance analyzer). The circuit is described by the following equations[17]

$$I = \frac{V_o}{R_s} \tag{3.1}$$

$$Z = \frac{V_i}{I} = \frac{V_i}{V_o/R_s} \tag{3.2}$$

Since PZTs are a capacitive element the current through them increases with frequency. Conversely, at low frequencies the circuit has very high impedance. In this case an inverting amplification circuit can be used to provide a larger output voltage. The size of the sensing resistor could be increased however, this reduces the voltage applied to the PZT (a larger voltage drop occurs on the sensing resistor).
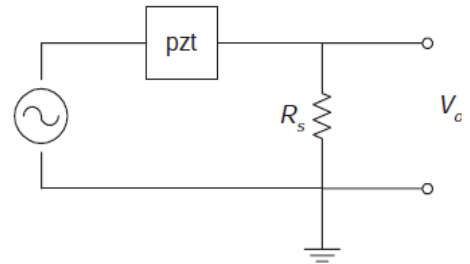
Figure 3.9: Only resistance PZT circuit

3.2 Modeling of a structure with piezoelectric patch

To analyze the piezoelectric circuits integrated to the structure, the system of a structure with piezoelectric patch has to be modeled. In this section a structure with piezoelectric patch attached to it is modeled by considering the structure as a beam. The electro mechanical properties of the piezoelectric attached to the structure will have significant effect on the frequency response of the structure. The linear constitutive relation for a piezoelectric material has various equivalent forms, the following is one of those which is frequently used in one-dimensional application.

$$T = c^E S - e^T E \tag{3.3}$$

$$D = e^S S - \varepsilon^S E \tag{3.4}$$

Where c is the modulus of elasticity, e is the dielectric constant and the superscript, S signifies that the parameter was measured at constant strain and the superscript, E indicates that the parameter was measured at constant electric field (short circuit). These constitutive equations

relate the electrical and mechanical properties of the PZT element. The specifications of these relationships allow electromechanical interaction to be included in the model.

Here for the analysis purpose the structure to which piezoelectric is attached is considered as a cantilever beam as shown in Figure 3.2. The following derivation uses energy methods to develop the consecutive equations of the cantilever beam with a piezoelectric patch attached to it. The general form of the Hamilton's principle is the basic energy conservation

$$\int_{t_1}^{t_2} [\delta T - \delta U - \delta E + \delta W] dt = 0 \tag{3.4}$$

Where T is the total kinetic energy of the system, U is the potential or elastic energy of the system, E is the electrical energy of the piezoelectric and W is the virtual work done. In this case the above terms are separated as

$$\int_{t_1}^{t_2} [\delta T_b + \delta T_p - \delta U_b - \delta U_p - \delta E_p + \delta W_v] dt = 0 \tag{3.5}$$

Where T_b, T_p, U_b, U_p, E_p and W_v are, respectively the kinetic energy of the beam, kinetic energy of the PZT patch, the elastic energy of the beam, the elastic of the PZT and electrical energy of the PZT patch, and the virtual work done over the volume.

The total kinetic energy T is

$$T = T_b + T_p = \int_{V_b} \rho_b \ddot{w}^2 dV_b + \int_{V_p} \rho_p \ddot{w}^2 dV_p \tag{3.6}$$

Where ρ_b, ρ_p, V_b, V_p and w are density of the beam, density of piezoelectric, volume of the beam, volume of the piezoelectric patch and the transverse displacement of the beam respectively

The total potential energy U is

$$U = U_b + U_p = \int_{V_b} STdV_b + \int_{V_p} STdV_p \tag{3.7}$$

Where *S* and *T* are the strain and the stress in the beam and the piezoelectric patch

The electrical energy of the piezoelectric E is

$$E = E_p = \int_{V_p} EDdV_p \tag{3.8}$$

Where E and D are the electric field and electric displacement of the piezoelectric patch

Based on the mode superposition principle the transverse displacement of the beam is assumed to be as below

$$w(x,t) = \varphi(x)q(t) \tag{3.9}$$

where $\varphi(x) = A(\cos(\beta x) + \cosh(\beta x) + \sin(\beta x) + \sinh(\beta x))$ is the first Eigen function or mode shape function of the cantilever beam without the piezoelectric patch and shunt circuit, $q(t)$ and is the generalized mechanical displacement, and β depends on the mode.

The assumption made is to apply the Euler–Bernoulli beam theory. This allows the strain in the beam to be the product of the distance from the neutral axis and the second derivative of displacement with respect to the position along the beam. The mechanical strain S in the beam is given as

$$S = -y\frac{\partial^2 w(x,t)}{\partial x^2} = -y\ \varphi(x)''q(t) \tag{3.10}$$

The change in the kinetic energy is give by differentiating Eq. 3.6 with respective to time

$$\delta T = \left(\int_0^{l_b} \rho_s A_s \varphi(x)^2 dx + \int_0^{l_b} \rho_p A_p \varphi(x)^2 \Delta H dx \right) \dot{q}(t)q(t) \tag{3.11}$$

Where $\Delta H = H(x - x_a) - H(x - x_b)$ and Heavyside step function x_a and x_b are the initial and final positions of the piezoelectric patch over the length of the structure. A_s and A_p are the area of the beam and piezoelectric patch.

$$\delta T = (M_b + M_p)\ \dot{q}(t)q(t) \tag{3.12}$$

M_b and M_p are the modal mass of the beam and piezoelectric patch, which are integral functions of the mode shape $\varphi(x)$

The total kinetic energy in the Eq. 3.11 can be split into both mechanical and electrical parts by substituting the piezoelectric Eq. 3.3 &3.4 into it

$$U = U_s + U_p = \int_{V_s} S c_s S dV_b + \int_{V_p} S c_p^E S dV_p - \int_{V_p} S e^T E dV_p \qquad (3.13)$$

The term e is the PZT coupling coefficient and relates the stress to the applied electric field. The PZT coupling coefficient can be written as shown in Eq. 3.3 &3.4 in terms of the more commonly specified coupling coefficient d by

$$e^T = d_{31} c_p^E \qquad (3.14)$$

The third and last assumption is that the electric potential across the PZT element is independent of the spatial coordinates. This assumption also indicates that no field is applied to the beam. The electric potential is then given ad the voltage produced per thickness of the piezoelectric.

$$E = \frac{v(t)}{t_p} \qquad (3.15)$$

The change in the potential energy is give by differentiating Eq. 3.7 with respective to time

$$\delta U = \left(\int_0^{l_b} c_s I_s \varphi''(x)^2 dx + \int_0^{l_b} c_p^E I_p \varphi''(x)^2 \Delta H dx \right) \ddot{q}(t) \dot{q}(t)$$
$$+ \left(\int_0^{l_b} \frac{c_p^E d_{31} F_p}{t_p} \varphi''(x) \Delta H dx \right) \dot{q}(t) v(t) \qquad (3.16)$$

Where I_s , I_p and F_p are the second moment of inertia of the beam , second moment of inertia of the piezoelectric patch and first moment of inertia of the piezoelectric patch. All of them are with respect to the neutral axis of the beam. d_{31} is the piezoelectric strain coefficient

$$\delta U = (K_s + K_p) \, \ddot{q}(t) \dot{q}(t) + K_{sp} \, \dot{q}(t) v(t) \qquad (3.17)$$

K_b and K_p are the modal stiffness of the beam and piezoelectric patch, which are integral functions of the mode shape $\varphi''(x)$. K_{sp} is the electro mechanical coupling coefficient which show the interaction of the piezoelectric and the structure.

The electrical energy of the piezoelectric can be spit as two components by substituting the piezoelectric effect Eq. 3.3&3.4 in Eq. 3.8

$$E = E_p = \int_{V_p} E e^T S dV_p + \int_{V_p} E \varepsilon^S E dV_p \qquad (3.18)$$

The change in the electrical energy is

$$\delta E = \left(\int_0^{l_b} \frac{c_p^E d_{31} F_p}{t_p} \varphi^{''(x)} \Delta H dx \right) q(t)\dot{v}(t) + \left(\int_0^{l_b} \frac{\varepsilon^S}{t_p{}^2} \Delta H dx \right) v(t)\dot{v}(t) \tag{3.19}$$

d_{31} is the piezoelectric strain coefficient and ε^S is the dielectric coefficient of the piezoelectric material.

$$\delta E = K_{sp} \, q(t)\dot{v}(t) + K_{pp} \, v(t)\dot{v}(t) \tag{3.20}$$

K_{sp} is the electro mechanical coupling coefficient and the K_{pp} is the effect due to capacitance of the piezoelectric material

The change in the work done is the sum of the work done due to external force, structural damping force and the electric charge.

$$\delta W = \int_0^{l_b} \hat{F}_e \dot{w}(x,t) \, dx - \int_0^{l_b} F_d \dot{w}(x,t) \, dx + \dot{v}(t)Q(t) \tag{3.21}$$

$$F_d = C_d \dot{w}(x,t) \tag{3.22}$$

$$\delta W = \left(\int_0^{l_b} \hat{F}_e \varphi(x) dx \right) \dot{q}(t) - \left(\int_0^{l_b} C_d \varphi(x)^2 \, dx \right) \dot{q}(t)\dot{q}(t) + \dot{v}(t)Q(t) \tag{3.23}$$

$\hat{F}_e$ is the external force vector, F_d is the force due to damping and C_d is the damping coefficient,

$$\delta W = F_s \dot{q}(t) - C \dot{q}(t)\dot{q}(t) + \dot{v}(t)Q(t) \tag{3.24}$$

In the Hamilton equation the integral is zero only when the integrant is zero

$$\delta T_b + \delta T_p - \delta U_b - \delta U_p - \delta E_p + \delta W_v = 0 \tag{3.25}$$

By substituting the above derived equations for the change in the energy's and work done in Eq. 3.25 leads to the following coupled equation

$$(M_b + M_p) \, \dot{q}(t)q(t) + (K_s + K_p) \, \ddot{q}(t)\dot{q}(t) - K_{sp} \, \dot{q}(t)v(t) + K_{sp} \, q(t)\dot{v}(t) + K_{pp} \, v(t)\dot{v}(t)$$
$$= F_s \dot{q}(t) - C \dot{q}(t)\dot{q}(t) + \dot{v}(t)Q(t) \tag{3.26}$$

The above equation can be split in to two coupled equations as below. The two equations are couple by the electro-mechanical coupling coefficient K_{sp}. The first equation defines the mechanical motion and the second equation defines the electrical properties of the system

$$(M_b + M_p)\,\ddot{q}(t) + (K_s + K_p)\,q(t) + C\dot{q}(t) + K_{sp}\,v(t) + K_{sp} = F_s \tag{3.27}$$

$$K_{sp}\,q(t) + K_{pp}\,v(t) = Q(t) \tag{3.28}$$

These equations now represent the electro-mechanical system and can be used to determine the motion of the beam to which a piezoelectric patch is attached.

The following Figure 3.2 shows the effect of the frequency shift for the first 10 modes of the beam due to the shunted piezoelectric patch, the frequency response is plotted for the short circuit of the piezoelectric and open circuit of the piezoelectric.
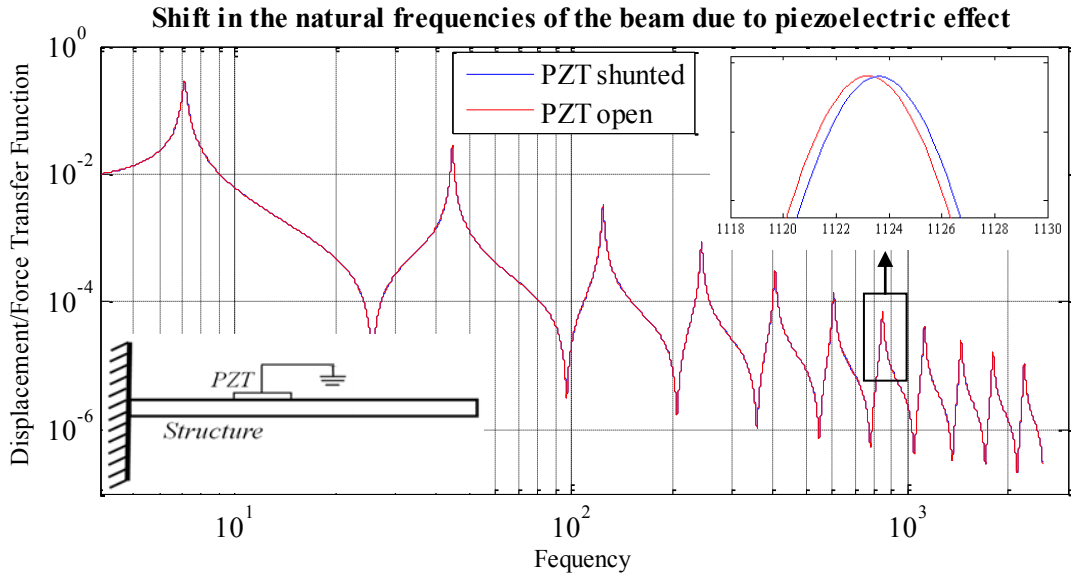
Figure 3.2: Shift in the frequency response of the beam due to piezoelectric effect

3.2.1 Coupling coefficient

The two coupled equations of motion of the piezoelectric have a common term also the coupling term called coupling coefficient. This coupling coefficient value is mode dependent and various for different modes. The mode with larger coupling coefficient will lead to better interaction between the structural properties of the structure and the change in the parameters of the piezoelectric circuit[64]. Since the damage detection is more sensitive at higher frequencies only modes higher than 10 are considered. The coupling coefficient values of 10 to 20 modes listed in the Table 3.1. It is shown that the coupling coefficient of the 17th mode is higher over the 20modes, hence all the below simulations are done for the 17th mode. Also the sign of the

coupling coefficient will not affect the properties because all the transfer function shown below has only the square of the coupling coefficient term

Table 3.1: Coupling coefficient values for different modes

Mode No	11	12	13	14	15	16	17	18	19	20
Coupling coefficient($K_{sp}/10^6$)	0.74	0.81	-0.14	-1.25	-1.17	0.36	1.88	1.52	-0.71	-2.58

3.3 Single degree freedom inductance circuit

3.3.1 Circuit description

In this section inductor is added in addition to resistance for the impedance measuring circuit. The Figure 3.3 shows the simple inductance circuit integration to the structure where the total circuit forms a LCR circuit in which the piezoelectric patch bonded with the structure acts as capacitor. The resonant effect of the inductive circuitry can greatly increase the measurement amplitude. The inductor can be a tunable synthetic inductor which can be easily tuned to achieve the required resonant frequency of the circuit that is close to any structural resonance mode. Moreover, when the inductance is properly tuned, very significant dynamic interaction between the mechanical structure being monitored and the electrical circuitry will occur. This results in an order-of-magnitude amplification of the admittance change upon the occurrence of damage, which can yield much increased damage detection sensitivity.
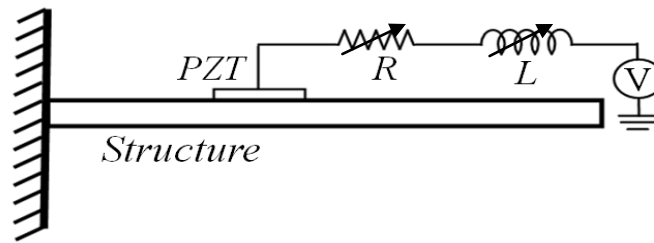
Figure 3.3: Single degree of freedom PZT inductance circuit integrated to the structure

From the above Eq. 3.27&3.28, the equations of motion of the inductance circuit integrated system can be given as

$$(M_b + M_p)\,\ddot{q}(t) + (K_s + K_p)\,q(t) + C\dot{q}(t) + K_{sp}\,v(t) = F_s \qquad (3.29)$$

$$K_{sp}\,q(t) + K_{pp}\,v(t) = Q(t) \qquad (3.30)$$

By modifying the above equations to $Q(t)$ charge in the piezoelectric as the parameter we get

$$(M_b + M_p)\,\ddot{q}(t) + (K_s + K_p)\,q(t) + C\dot{q}(t) + \frac{K_{sp}}{C_p}Q(t) = F_s \tag{3.31}$$

$$\frac{K_{sp}}{C_p}q(t) + \frac{K_{pp}}{C_p{}^2}Q(t) = V(t) \tag{3.32}$$

C_p is the capacitance of the piezoelectric patch attached to the structure.

Here $V(t)$ is the voltage across the piezoelectric patch which is given by Kirchhoff's voltage law

$$V(t) = -L\ddot{Q}(t) - RQ(t) + V_o \tag{3.33}$$

The modified coupled equations of motion are

$$M\,\ddot{q}(t) + Kq(t) + C\dot{q}(t) + K_1Q(t) = F_s \tag{3.34}$$

$$K_1\,q(t) + K_p\,Q(t) + L\ddot{Q}(t) + RQ(t) = V_o \tag{3.35}$$

By taking the Laplace transforms for the above two equations of motion and substituting $s = j\omega$ we get

$$(-\omega^2 M + j\omega C + K)q + (K_1)Q = F_s \tag{3.36}$$

$$\left(-\omega^2 L + j\omega R + K_p\right)Q + (K_1)q = V_o \tag{3.37}$$

These above two coupled equations of Eq. 3.36&3.37 can be used to derive the transfer functions of the structural response over external disturbance and that between structural response and input voltage

$$\frac{q}{F_s} = \frac{-\omega^2 L + j\omega R + K_p}{\left(-\omega^2 L + j\omega R + K_p\right)(-\omega^2 M + j\omega C + K) - K_1{}^2} \tag{3.38}$$

$$\frac{q}{V_o} = \frac{K_1}{K_1{}^2 - \left(-\omega^2 L + j\omega R + K_p\right)(-\omega^2 M + j\omega C + K)} \tag{3.39}$$

The above two transfer functions are plotted in Figure 3.4 for the 17th mode where all the structural properties like the mass, stiffness, damping and the electro-mechanical coupling coefficient are taken only for the respective mode. The inductance L is chosen according to the capacitance of the piezoelectric to get the resonant frequency same as the structure modal frequency. The resistance of the plot is just taken as 10ohms. The figure shows the two peaks

near to each other one is the structural modal resonance and the other is induced due to the inductance circuit which is tuned near the structural resonance.
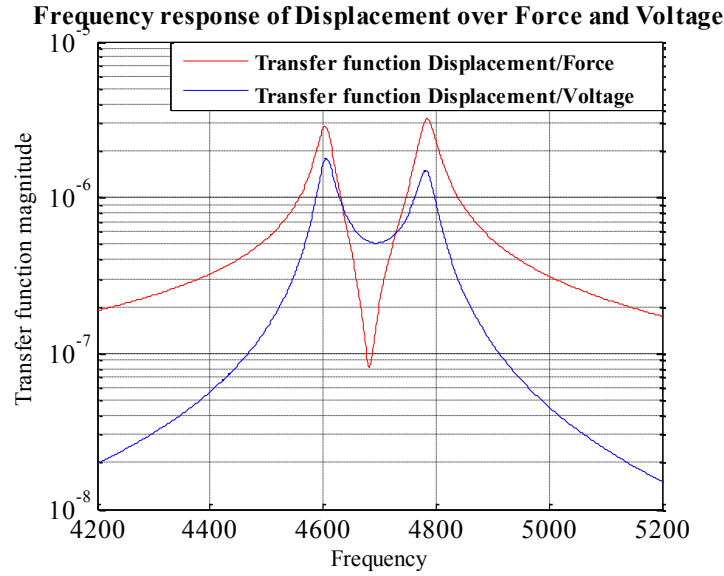
Figure 3.4: Frequency response of displacement over force and voltage for Single DOF PZT inductive circuit integrated to structure

3.3.2 Admittance of the circuit

For the structural damage detection mainly the impedance of the circuit integrated to the same structure is measured over a frequency range and compared with that of the impedance measured when the structure is in pristine condition. Here we considered the admittance which is the inverse of the impedance. The admittance of this inductance circuitry integrated system can be derived from the same couple equations of motion in Eq. 3.36&3.37. The admittance of the circuit is the ratio of current over voltage input to the circuit.

$$Y = \frac{I}{V_o} \tag{3.40}$$

$$Y = \frac{V_r/R}{V_o} \quad V_r = V_o - K_1\, q(t) - K_p\, Q(t) - L\ddot{Q}(t) \tag{3.41}$$

The by using the above transfer functions in Eq. 3.38&3.39 and the equation in Eq. 3.41 we get the admittance of the circuit as

42

$$Y = \frac{I}{V_o} = \frac{j\omega(-\omega^2 M + j\omega C + K)}{(-\omega^2 L + j\omega R + K_p)(-\omega^2 M + j\omega C + K) - K_1{}^2} \qquad (3.42)$$

For clear demonstration the admittance of the above circuit is normalized with respect to the electrical admittance of the stand alone piezoelectric transducer $Y_p = j\omega/K_p$

$$Y_N = \frac{Y}{Y_p} = \frac{K_p(-\omega^2 M + j\omega C + K)}{(-\omega^2 L + j\omega R + K_p)(-\omega^2 M + j\omega C + K) - K_1{}^2} \qquad (3.43)$$

The normalized admittance of the inductor circuit and just resistance circuit is plotted in Figure 3.5. We can get the admittance in the just resistance circuit by taking inductance L=0. The figure shows that the admittance of the inductor circuit is enhanced and an additional peak is also seen over the simple resistance case.
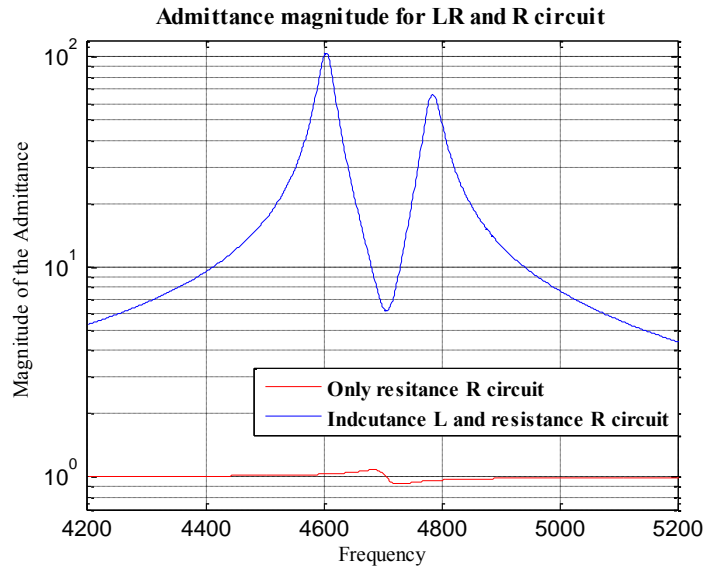
Figure 3.5: Comparison of the admittance for single DOF inductive circuit and resistive circuit integrated to structure

The Figure 3.6 shows the sensitivity of the admittance for a small change of the inductance value. The two resonant peaks heights of the admittance change for a small change of the inductor value. The Figure 3.7 shows the admittance change for the different resistor values. As the resistance increase the damping of the structure and also the integrated circuit vary.
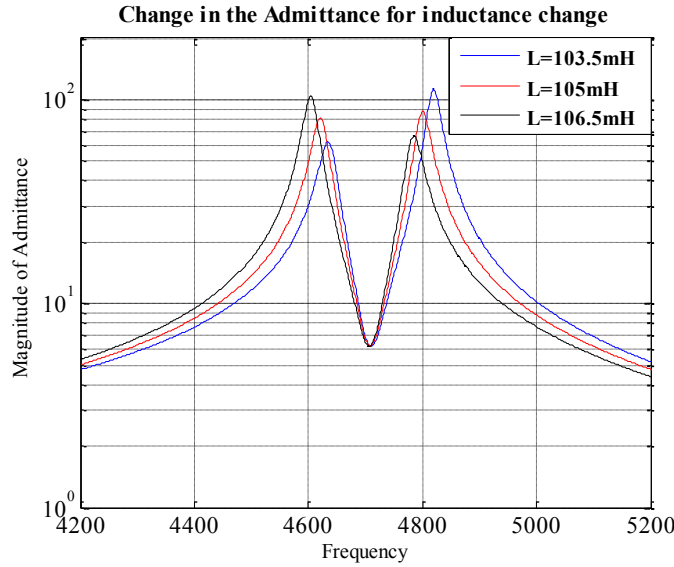
Figure 3.6: Admittance sensitivity to inductance change for single DOF inductive circuit integrated to structure
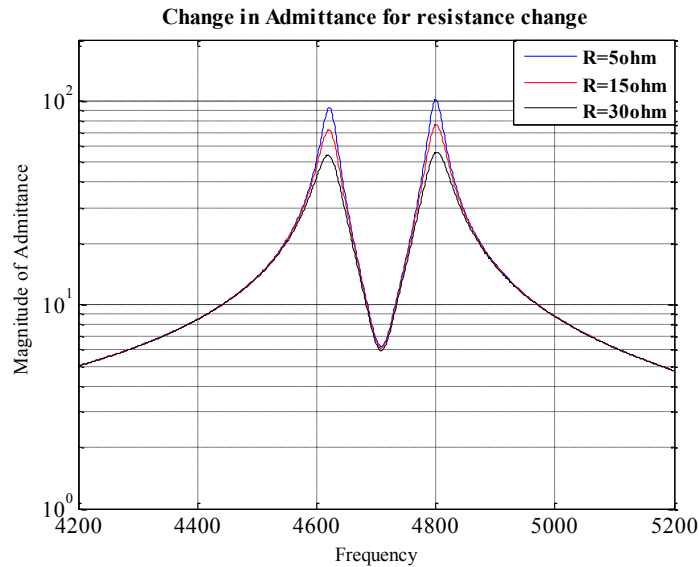
Figure 3.7: Admittance sensitivity to resistance change for single DOF inductive circuit integrated to structure

3.3.3 Change in the admittance of circuit for a damage

The analyses in the previous sections have demonstrated the positive effect of the inductance circuitry for the admittance enhancement. In the structural damage detection the change in the admittance that is the damage detection sensitivity is measure to assess the health of the structure. The change in the admittance is given as

$$\Delta Y_N = \frac{K_p\left(-\omega^2 M + j\omega C + K\right)}{\left(-\omega^2 L + j\omega R + K_p\right)\left(-\omega^2 M + j\omega C + K\right) - K_1{}^2}$$
$$- \frac{K_p\left(-\omega^2 M + j\omega C + (K - \Delta K)\right)}{\left(-\omega^2 L + j\omega R + K_p\right)\left(-\omega^2 M + j\omega C + K - \Delta K\right) - K_1{}^2} \qquad (3.44)$$

Since the above equation for the change in admittance due to a damage occurrence ΔY_N i.e. the change in the structural stiffness is a nonlinear function of the stiffness change ΔK, Taylor series approximation is used for optimizing the function in the later section.

$$\Delta Y_N(\Delta K) = \Delta Y_{N_{(\Delta K=0)}} + \frac{\partial \Delta Y_N}{\partial \Delta K}_{(\Delta K=0)} \Delta K \qquad (3.43)$$

$$\Delta Y_N(\Delta K) = \frac{K_p K_1{}^2}{\left(\left(-\omega^2 L + j\omega R + K_p\right)\left(-\omega^2 M + j\omega C + K\right) - K_1{}^2\right)^2} \Delta K \qquad (3.44)$$

The Figure 3.8 shows the change in the admittance for a different percentage of change in the structural stiffness. The Figure shows that the admittance change is significantly enhanced due to the inductance circuitry than that of the just resistive circuit.
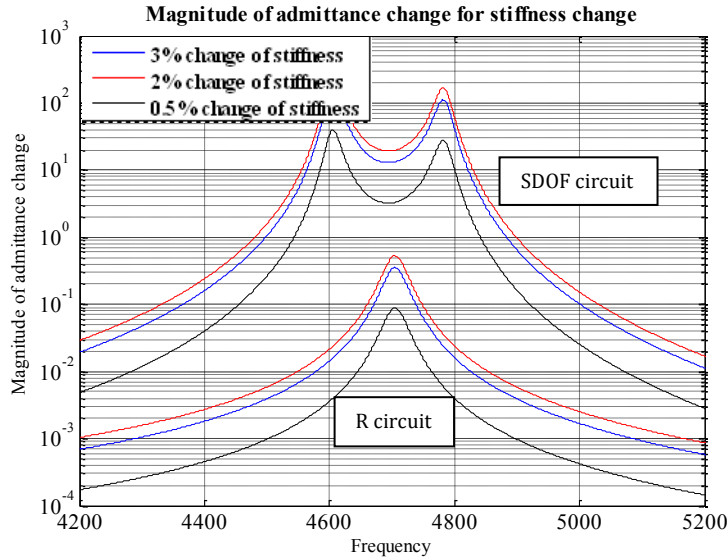
Figure 3.8: Admittance change for percentage of structure stiffness change for single DOF inductive circuit integrated to structure

3.3.4 Damage detection metric, Root mean square deviation (RMSD)

The measured data like the admittance has to be processed. That is the current measured data has to be compared or correlated with the baseline measurements which are taken under no damage conditions to assess the damage in the structure. There are various statistical damage metric methods to compare or correlate the data for the damage assessment. The RMSD root mean square deviation is found suitable for the characterizing the occurrence of the new damage in a structure. The RMSD of the admittance is shown in the Eq. 3.45

$$\text{RMSD} = \frac{\sqrt{\sum_1^n \text{Re}(\Delta Y_N)^2}}{\sqrt{\sum_1^n \text{Re}(Y_N)^2}} \tag{3.45}$$

Where $\text{Re}(\Delta Y_N)$ the real part of the admittance change ΔY_N , $\text{Re}(Y_N)$ is the real part of the actual admittance when the structure is in pristine condition and *n* denotes the number of frequency point over the frequency range.

$$\text{RMSD}(\Delta K) = \frac{\text{RMSD}}{\Delta K} = \frac{\sqrt{\sum_1^n \text{Re}(\delta Y_N)^2}}{\sqrt{\sum_1^n \text{Re}(Y_N)^2}} \tag{3.46}$$

$$\delta Y_N = \frac{\Delta Y_N(\Delta K)}{\Delta K} = \frac{K_p K_1^2}{\left(\left(-\omega^2 L + j\omega R + K_p\right)(-\omega^2 M + j\omega C + K) - K_1^2\right)^2} \tag{3.47}$$

The RMSD value has to be high to have good sensitivity for damage detection. The RMSD value will have a maximum for certain value of inductance L and resistance R. The optimal values of the L and R can be found by optimizing the function $\text{RMSD}(\Delta K)$ to achieve the maximum value of the RMSD. The Figure 3.9 show the surface plot of the function $-\text{RMSD}(\Delta K)$ value for the various valued of the L and R. The Figure 3.9 shows that there are several local minimum values and also a global minimum, which is a maximum for the function$\text{RMSD}(\Delta K)$. This value is found using the optimization toolbox in the Matlab, the optimization algorithm used by Matlab is described in the appendix.
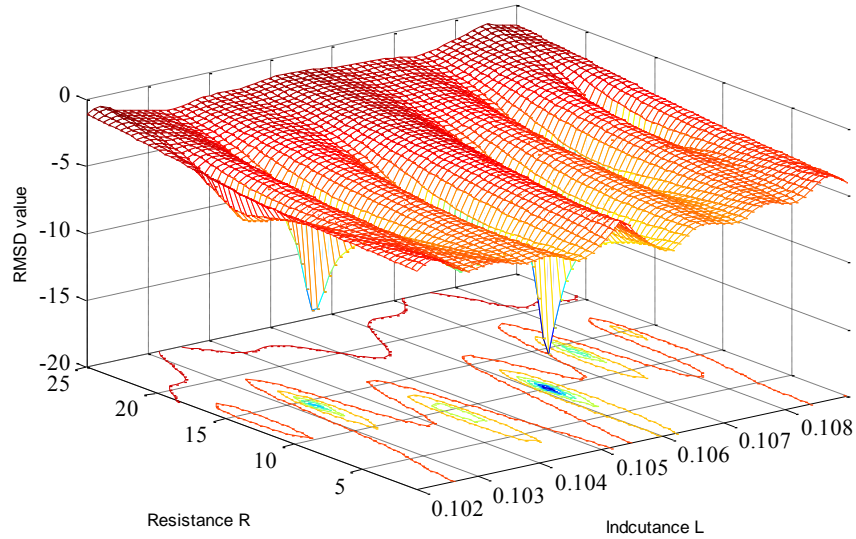
Figure 3.9: Surface plot for objective function (RMSD) vs. inductance and resistance for single DOF inductive circuit integrated to structure

The optimal values of the inductance (L=106.2mH) and the resistance (R=10.07ohm) are found using the optimization toolbox and the values are used to plot the shift in the admittance for a change in the structural stiffness caused due to the damage. The Figure 3.10 shows that a significant change in the peaks heights and also shift in the peaks of the admittance change magnitude.
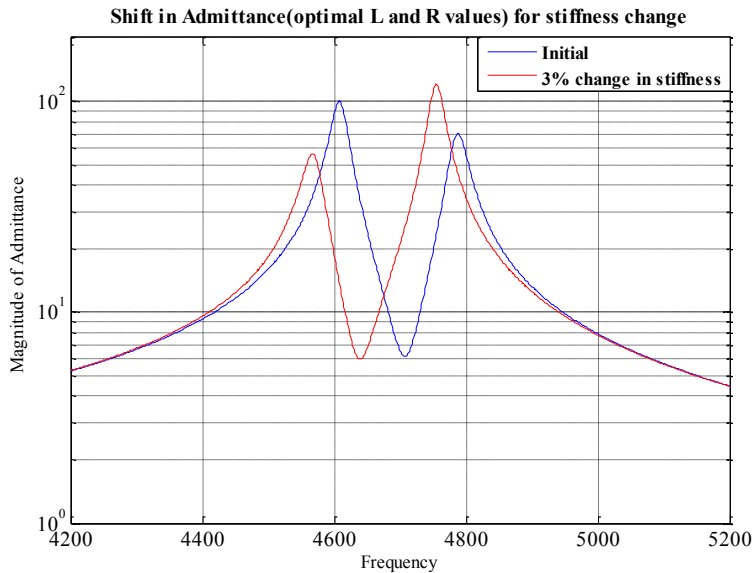
Figure 3.10: Shift in the admittance peaks to the structural stiffness change for single DOF inductive circuit (optimal values) integrated to structure

47

The Figure 3.11 shows both the actual admittance and the admittance change where it is clear that the admittance change caused due to damage is significant when compared to the actual admittance of the circuit.
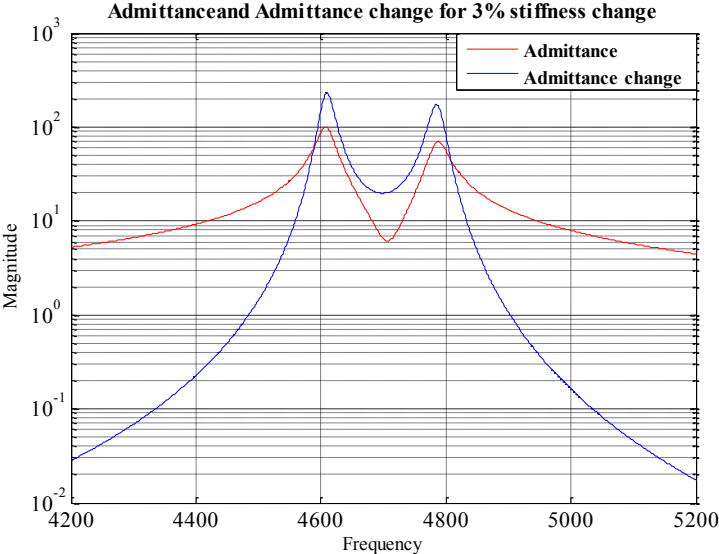
Figure 3.11: Admittance and Admittance change for single DOF inductive circuit (optimal values) integrated to structure

3.4 Two degree freedom inductance circuit

3.4.1 Circuit description

In this section a two degree freedom inductance circuit shown in Figure 3.12 is investigated for the admittance based structural damage detection. The two degree freedom circuit will be a higher order circuit. The higher order circuit will have more sensitivity to parameter changes and also broadens the admittance over the frequency range by inducing an additional peak.
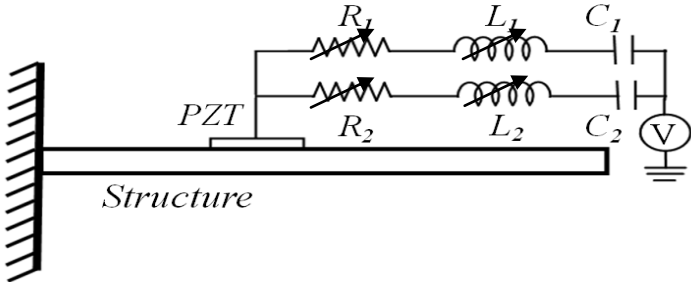
Figure 3.12: Two degree of freedom PZT inductance circuit integrated to the structure

$V(t)$ is the voltage across the piezoelectric patch which is given by Kirchhoff's voltage law

$$V(t) = -L_1\ddot{Q}(t) - R_1\dot{Q}(t) - \frac{Q(t)}{C_1} + V_o \tag{3.48}$$

The modified coupled equations of motion are

$$M\,\ddot{q}(t) + Kq(t) + C\dot{q}(t) + K_1Q(t) = F_s \tag{3.49}$$

$$K_1\,q(t) + K_p\,Q(t) + L_1\ddot{Q}(t) + R_1\dot{Q}(t) + \frac{Q(t)}{C_1} = V_o \tag{3.50}$$

$$L_1\ddot{Q}_1(t) + R_1\dot{Q}_1(t) + \frac{Q_1(t)}{C_1} = L_2\ddot{Q}_2(t) + R_2\dot{Q}_2(t) + \frac{Q_2(t)}{C_2} \tag{3.51}$$

All the similar simulations done in the single degree freedom inductance circuit are repeated for the higher order circuit. These above three coupled equations can be used to derive the transfer functions of the structural response over external disturbance and that between structural response and input voltage

$$\frac{q}{V}$$
$$= \frac{AK_1}{K_1{}^2A - B(s^4L_1L_2 + s^3(L_2R_1 + L_1R_2) + s^2(R_1R_2 + LK_p + L_1K_{v2} + L_2K_{v1}) + s(RK_p + R_1K_{v1} + R_2K_{v2}) + K_pK_v + K_{v1}K_{v2})} \tag{3.52}$$

$$\frac{q}{F}$$
$$= \frac{s^4L_1L_2 + s^3(L_2R_1 + L_1R_2) + s^2(R_1R_2 + LK_p + L_1K_v) + s(RK_p + R_1K_v) + K_pK_v}{B(s^4L_1L_2 + s^3(L_2R_1 + L_1R_2) + s^2(R_1R_2 + LK_p + L_1K_{v2} + L_2K_{v1}) + s(RK_p + R_1K_{v1} + R_2K_{v2}) + K_pK_v + K_{v1}K_{v2}) - K_1{}^2A} \tag{3.53}$$

Where

$$A = s^2L + sR + K_v; \quad B = Ms^2 + sC_d + K;$$

$$L = L_1 + L_2; \quad R = R_1 + R_2; \quad K_v = K_{v1} + K_{v2};$$

$$K_{v1} = \frac{1}{C_1}; \quad K_{v2} = \frac{1}{C_2}$$

The above two transfer functions are plotted in figure (3.13) for the 17th mode where all the structural properties like the mass, stiffness, damping and the electro-mechanical coupling coefficient are taken only for the respective mode
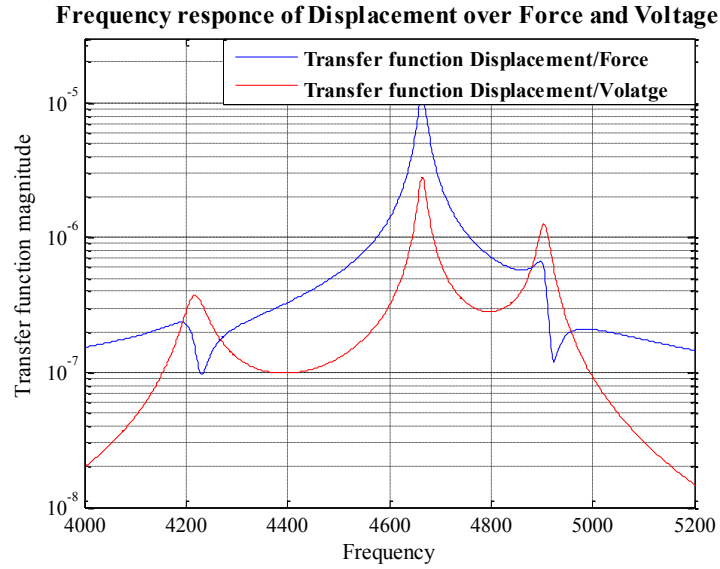
Figure 3.13: Frequency response of displacement over force and voltage for the Two DOF PZT inductive circuit integrated structure

3.4.2 Admittance of the circuit

The by using the above transfer functions in Eq. 3.52&3.53 and the equations of motion in Eq. 3.49, 3.50&3.51 we get the admittance of the circuit as

$Y_i(\Delta K)$

$$= \frac{K_p B A}{B(s^4 L_1 L_2 + s^3(L_2 R_1 + L_1 R_2) + s^2(R_1 R_2 + LK_p + L_1 K_{v2} + L_2 K_{v1}) + s(RK_p + R_1 K_{v1} + R_2 K_{v2}) + K_p K_v + K_{v1} K_{v2}) - K_1^2 A} \quad (3.54)$$
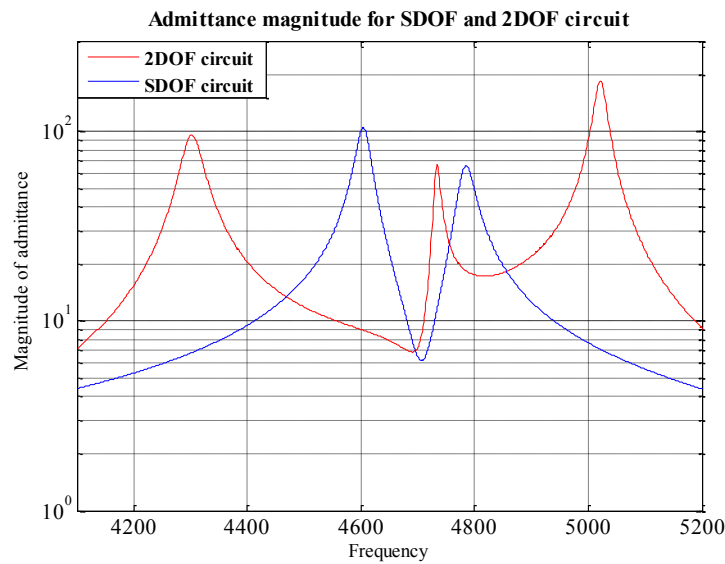
Figure 3.14: Comparison of the admittance for single DOF inductive circuit and Two DOF inductive circuit integrated to structure

50

The admittance of the two degree freedom impedance circuit integrated to the structure in Eq. 3.54 is plotted in Figure 3.14. The Figure 3.14 also shows the admittance of the single degree freedom circuit, it can be seen that he admittance is little enhanced in magnitude and also broadened with an additional peak due to the higher order of the circuit.

Change in Admittance for Inductance change
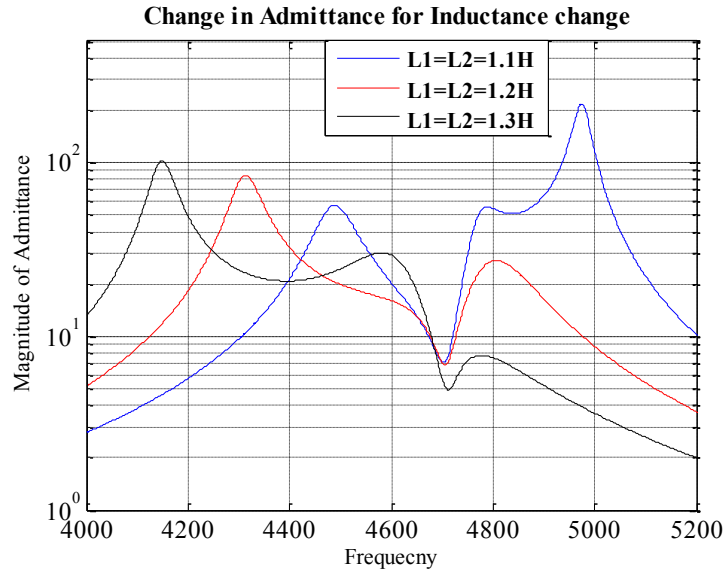
Figure 3.15: Admittance sensitivity to inductance change for Two DOF inductive circuit integrated to structure

Change in admittance for resistance change
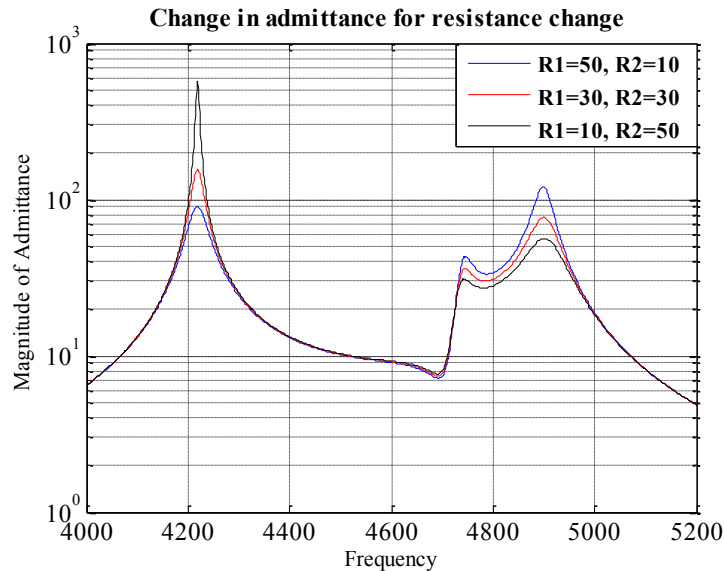
Figure 3.16: Admittance sensitivity to resistance change for Two DOF inductive circuit integrated to structure

The Figure 3.15 shows the sensitivity of the admittance for a small change of the inductance value. The three resonant peaks heights of the admittance change for a small change of the

51

inductor value. The Figure 3.16 shows the admittance change for the different resistor values. As the resistance increase the damping of the structure and also the integrated circuit vary.

3.4.3 Change in the admittance of circuit for a damage

The change in admittance for the two degree freedom circuit for a change in the structural stiffness is derived as in the same way of the above section 3.4.3, using the Taylor series approximation. The Eq(3.55) shows the expression for the admittance change for the two degree freedom circuit. The figure(3.17) show the admittance change for a different percentage of change in the structural stiffness. The figure shows that the admittance change is significantly enhanced due to the inductance circuitry than that of the just resistive circuit.

$$Y_i(\Delta K)$$

$$= \frac{KK_1^2A^2}{\left[B(s^4L_1L_2 + s^3(L_2R_1 + L_1R_2) + s^2(R_1R_2 + LK_p + L_1K_{v2} + L_2K_{v1}) + s(RK_p + R_1K_{v1} + R_2K_{v2}) + K_pK_v + K_{v1}K_{v2}) - K_1^2A\right]^2} \quad (3.55)$$
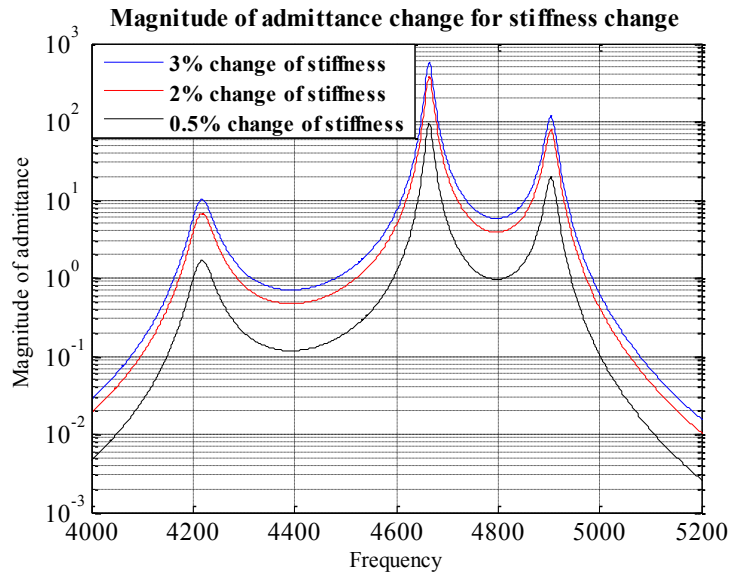
Figure 3.17: Admittance change for percentage of structure stiffness change for Two DOF inductive circuit integrated to structure

3.4.4 Damage detection metric, Root mean square deviation (RMSD)

The optimal values of the L and R can be found by optimizing the function $\text{RMSD}(\Delta K)$ to achieve the maximum value of the RMSD

$$\text{RMSD}(\Delta K) = \frac{\text{RMSD}}{\Delta K} = \frac{\sqrt{\sum_1^n \text{Re}(\delta Y_N)^2}}{\sqrt{\sum_1^n \text{Re}(Y_N)^2}}$$

52

Where δY_N is given in Eq. 3.55 and Y_N is given in Eq. 3.54 for the two degree of freedom circuit integrated to the structure

The optimal values of the inductance (L_1=1.106H and L_2=1.15H) and the resistance (R_1=97ohm and R_2=6ohm) are found using the optimization toolbox and the values are used to plot the shift in the admittance for a change in the structural stiffness caused due to the damage
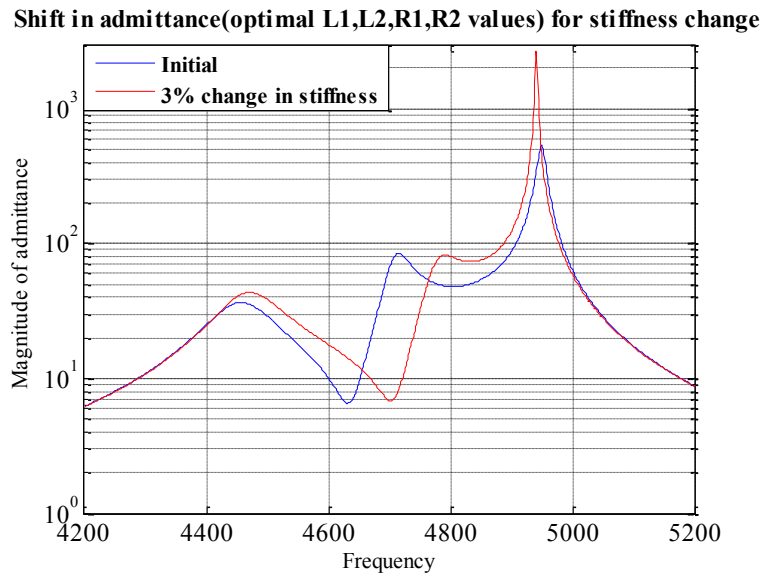
Figure 3.18: Shift in the admittance peaks to the structural stiffness change for Two DOF inductive circuit (optimal values) integrated to structure
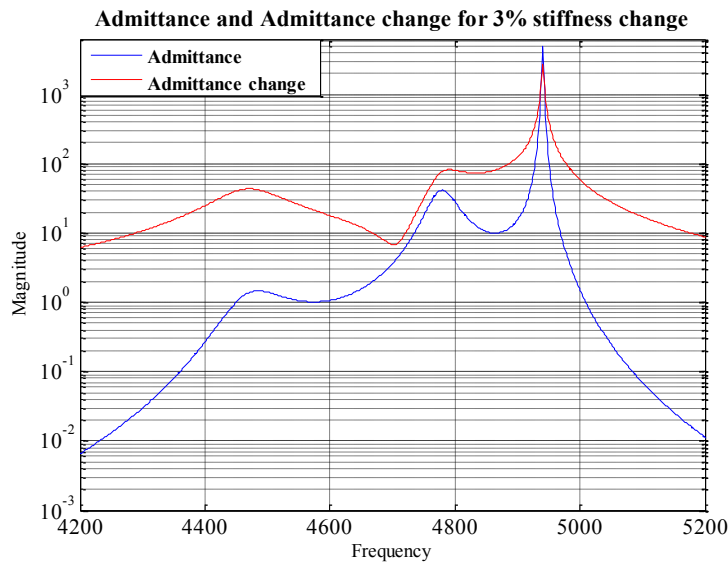
Figure 3.19: Admittance and Admittance change for Two DOF inductive circuit(optimal values) integrated to structure

53

3.5 Comparison of the RMSD values

The RMSD value of the admittance change for a structural stiffness change for the optimal values of the circuit parameters are compared to show that the inductance addition will increase the value significantly than the just resistance circuit and the two degree freedom circuit will have still increase the value over the single degree freedom circuit. The following Table 3.2 shows the comparison of the RMSD values.

Table 3.2: comparison of the RMSD values for all three types of circuits integrated to structure

PZT circuit type	Only resistance	SDOF- LCR circuit	2DOF- LCR circuit
RMSD value(optimal values of circuit)	0.0219	14.3425	27.8426

3.6 Conclusions

In this chapter two different piezoelectric inductive circuits integrated to the structure are analyzed for the low cost admittance based damage detection. The inductive circuit parameters are optimized for enhancing the damage metric sensitivity. It is shown that the single degree of freedom inductive circuit will increase the admittance based damage detection metric (RMSD) sensitivity over the simple resistive based circuit. The two degree freedom inductance circuit will increase the admittance based damage detection metric (RMSD) further more than the single degree freedom inductive circuit. This low cost admittance measurement circuits can be used to detect the very small size localized damage in the structure because of their enhanced sensitivity. This type of low cost enhanced damage detection sensitivity admittance measuring circuits can be used to detect damages in the joints like the bolted joints and welded joints of the rails.

Chapter 4 - Assessment of Linear Electromagnetic harvesters

4.1 Introduction

When the freight train moves on a track it gets deflected vertically due to the load exerted by the train on it. This track vertical displacement under the weight of a passing train can engage the regenerative device i.e. electromagnetic harvester for generating useful power. This generated power is stored and used for powering railway applications like track switches and signals directly. In this chapter linear Electromagnetic harvesters are assessed for Energy harvesting from Railway track vibrations. The power generated from the Electromagnetic harvester depends on various parameters like Radial magnetic flux(B_r), Velocity(V_{track}) at which the track deflects and length(L_{total}) of the harvester etc. These required parameters of the conventional Electromagnetic harvester of Tufts university design which is patented for the vehicle suspension energy harvesting [66] are estimated for generating the required electric power of 10watts, 250watts and 3000watts from railway track deflections caused due to train.

4.2 Introduction to Railway track electric infrastructure:

A substantial portion of railroad tracks exist in relatively remote areas, where electrical infrastructure is not present due to it being uneconomical to install and maintain. Thus absence of proper electrical supply leads to failure of railway safety devices like signals and switches, which leads to severe accidents. If a significant amount of energy can be harvested from track vibrations and stored to power the railway safety equipments the accidents can be prevented. The power requirements of the railway track electric infrastructure are important to estimate the requirements of the harvester. This section gives the details of the track electric infrastructure.

The main safety equipments are signal lights near grade crossings, grade crossing gate and track switch. Other railway equipments like axel counter to count the train traffic on the track and health monitoring sensors are also used in remote areas. All these safety equipments have different power requirements which are shown in the below Table 4.1 [67&68].

Table 4.11 Power requirements for the railway safety equipments

Safety equipment	Track switch	Signals (LED lights)	Axle counter	Grade crossing gate
Power required(watts)	800-1000	8-10	100-150	150-200
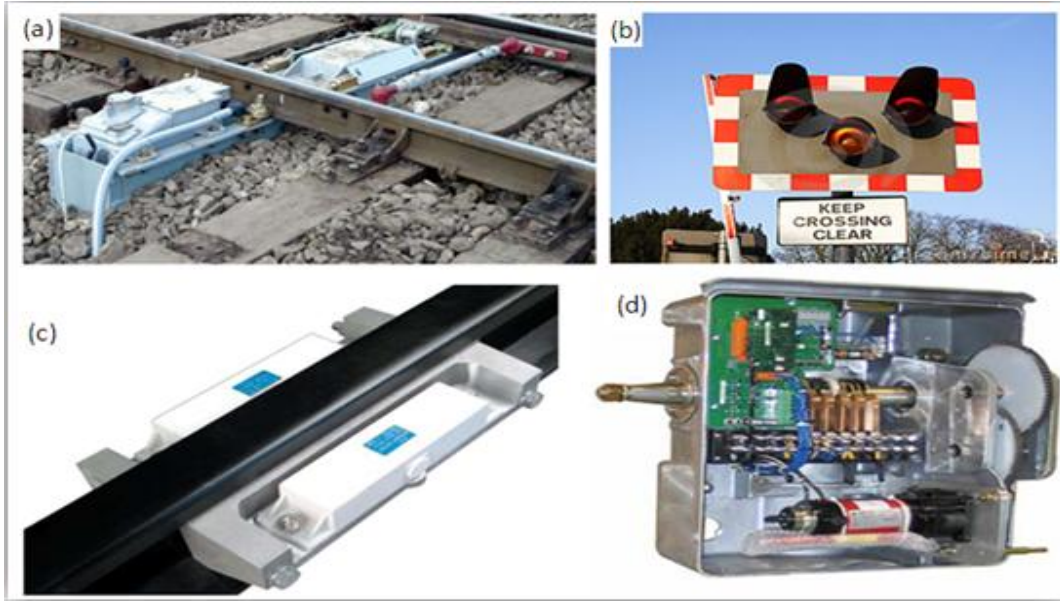
Figure 4.1 Railway safety equipments (a) Track switch; (b) Signal lights; (c) Axle counter; (d) Grade crossing gate [67&68]

Technologies have been developed for railway energy harvesting using piezoelectric harvesters [11], but piezoelectric harvester cannot generate sufficient energy to power the safety equipments they are only limited to track health monitoring. The EMH can produce more amount of power to power the safety equipments unlike the piezoelectric harvesters.

4.3 Track vibration due to moving train

When the train is moving on the track the track displaces vertically as shown in Figure 4.2 with certain velocity and frequency depending on the load exerted by the train, speed at which it is moving and track substructure (ballast, underground soil) properties. A typical freight train moves with a speed of 25mph and exerts a load around 20,000 to
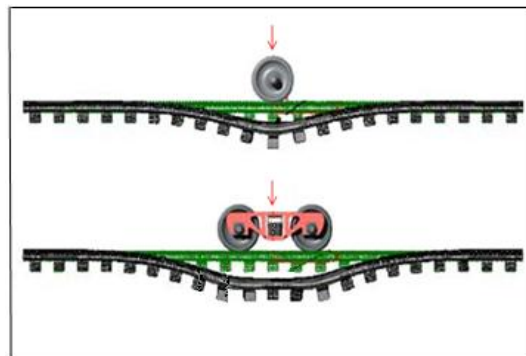
Figure 4.2 Vertical track deflection [69]

30,000pounds on the track surface [69&70]. The maximum range of track displacement can be up to 20mm, with the average travel 7mm to 12mm [69-71]. The periodic frequency at which the track deflects depends on the distance between the two bogies of the train. Usually the freight trains have different cart lengths so the distance between bogies is not uniform. The frequency is

around 0.6Hz calculated by assuming the average uniform distance between the wheel pair of a bogie is 16mts and the train is moving at a speed of 25mph.
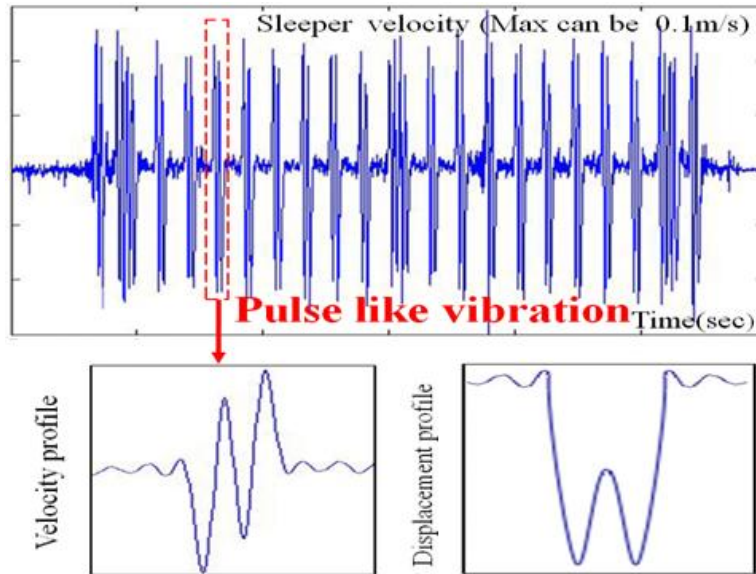
Figure 4.3 Track vibration profile (pulse like vibration)

The Figure 4.3 show the profile of the track vibration caused due a moving train. The figure clearly depicts that the track vibration is like a pulse which is not continuous when the train is moving on it. At a point the track moves down vertically only when the wheel is under it, retains it position when the wheel crosses the point and will remain in the idle position until the next wheel comes near the point. During the time when there is no wheel directly under the particular point the track displacement is almost zero. The idle period of the track vibration depends on the distance between two wheel pairs. The track vibration directly under the wheel is not exactly sinusoidal profile it has different profile as show in Figure 4.3, this is because the wheels of the train are in pairs as shown in Figure 4.2. The profile will be close to sinusoidal when the train is moving at very high speed. The peak vibration speed of the track mainly depends on the velocity of the train. The peak velocity can be up to 0.1m/s for a train moving at average velocity of 60km/hr. Also the track deflections are large at the grade crossing due to the sudden change in the stiffness.

4.4 Estimation of available power on the railway track

The estimation of the available power is important to design the harvester. The average power available on the railway track site due to the moving train can be estimated using the following equation

57

$$P_{avg} = \frac{NFd}{T} \qquad\qquad 4.1$$

N is the No of wheel pairs for a train, d is the total track displacement due to a pair of wheels, F is the normal force excreted by wheel pairs on the track and T is the total time taken by the train to pass by

Normal load exerted by the freight train wheels on the track is 20000pounds to 30000 pounds.

The average vertical track displacement is 7mm to 10mm

The total distance moved by the track is estimated using the displacement profile shown in Figure 4.3. The total distance moved is 20mm and 28mm for the average vertical displacement of 7mm and 10 mm respectively.

Assuming the train has 10 bogies (20 pairs of wheels on one side and 160mts length bogie) and moving at a speed of 40km/hr the available power can be estimated using Eq. 4.1.

The average power available on the track side is 3kw to 5kw. Considering that 40% of the energy is transferred to the harvester the useful power is 1.5kw to 2.5kw.

4.5 Principle of Electromagnetic Harvester

The Electromagnetic harvester(EMH) is in the configuration of the linear generator. The EMH consists mainly of magnetic array rings and coil assembly. As the coil with a cross section(A_c) and length(l_c) cuts the radial magnetic flux(B_r) with a constant velocity(v_z) the EMF voltage V generated is given by the Eq. 4.2.

$$V = B_r v_z l_c \qquad\qquad 4.2$$

The maximum current(I) generated in the coil is given by equation[2].

$$I = \sigma B_r v_z A_w \qquad\qquad 4.3$$

Where σ is the electrical conductivity of the conductor, B_r is the magnetic field intensity in the radial direction, v_z is the constant relative velocity of the coil conductor in the axial direction moving in the magnetic flux and A_w is the cross-sectional area of the conductor

The power (P) generated per coil is calculated by the Eq. 4.4.

$$P = VI = \sigma B_r^2 v_z^2 A_w l_c = \sigma B_r^2 v_z^2 V_{coil} \qquad\qquad 4.4$$

From the Eq. 4.4 it can be said that the increase in magnetic flux B_r or increase in velocity of the coil will increase the power of the EMH. The principle used in the Tufts EMH design is increase in the magnetic flux density B_r within the coil region to harvest more power.

4.6 Estimation of Parameters to harvest required power

The Power generated per coil is given in Eq. 4.4. To generate a required power of 10watts, 250watts and 3000watts a certain number of coils are required. The No of coils required can be calculated by calculating the power output from each coil which depends on the following parameters they are.

1) Radial Magnetic flux density B_r
2) Average velocity of the track V_{track}
3) Volume of the coil V_{coil}

The estimation of the above parameters for the EMH of Tufts University design (Max Dia 6inch) and specified design (Max Dia 3.5inch) are described below.

4.6.1 Radial Magnetic flux density (B_r)

Eq. 4.4 shows that the power of the electromagnetic shock absorber is directly proportional to the radial magnetic flux density B_r. Figure 4.4 shows the cross sectional view of the Tufts Electromagnetic harvester with two magnetic arrays. The Electromagnetic harvester has two sets of concentric magnetic array rings, inner and outer. The orientation of the both inner and outer cylindrical concentric magnets of the design is as shown in the Figure 4.4. The inner concentric magnets are glued to aluminum rod to fix them in the respective positions. An air gap is provided between the inner and outer magnets to place the coil windings. The inner coil is placed between the inner and outer magnetic

Figure 4.4 : Cross sectional view of Tufts Design[66]

rings where as the outer coil is placed outside the outer magnetic rings. The inner and outer magnetic array rings are separated by high permeability spacer to limit dispersion of magnetic

fields at magnetic pole regions and enhance the radial magnetic flux density within the coil winding regions. Since the arrangement of magnets and coils is planar symmetric the average radial magnetic flux density(B_r) within the coil regions for the design is analyzed by 2D FEA software *Finite Element Method Magnets*[72].

The 2D FEA analysis is done for two design specifications. One is for the example provided in the Tufts Patent [1] which has the maximum diameter of 6inches and the later is with specification which limits the maximum diameter to 3.5inches. In both the designs the width of the air gap(G) between the inner and outer magnetic arrays within the magnetic coil region is same.

4.6.1.1 Tufts Design (Max Diameter 6in)

The dimensions of the Design used for the FEA analysis is listed in the Table 4.2. The materials used in the FEA analysis are NdFeB grade N52 magnets and the steel 1018 spacer between magnetic arrays with relative magnetic permeability 529, which are used in the Tufts Electromagnetic harvester design. The analysis shown is done for 10 inner and outer magnetic arrays with in air medium. The results of 2D FEA analysis in Figure 4.5 shows the distribution of the inner and outer magnetic flux (IB_r and OB_r) in both radial and Z direction. This analysis is used to calculate the average radial magnetic flux within the coil regions which is used for the estimation of the power in the coils. The calculated values of average radial magnetic flux within the coil regions are show in the Table 4.2.
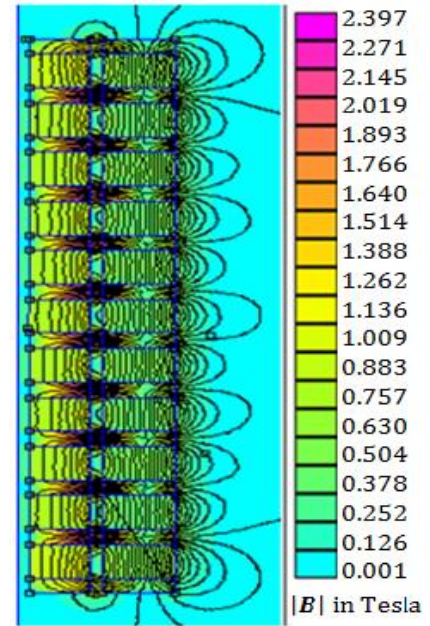
Figure 4.5 Radial Magnetic flux

Table 4.12 : Specifications and results for the Tufts Design (Max diameter of 6in)

G(mm)	R$_1$(mm)	R$_2$(mm)	H(mm)	R$_3$(mm)	R$_4$(mm)	L(mm)	IB$_r$(Tesla)	OB$_r$(Tesla)
5	2.5	35	10	40	75	22.5	1.81	0.57

4.6.1.2 Tufts Design (Max Diameter 3.5in)

The tufts design is reduced to the size of 3.5inch diameter to fit the required specifications. The inner and outer diameters of smaller and larger magentas are reduced keeping the air gap and thickness of the magnets and spacer as same in the tufts design. The dimensions of the Design 2 EMH used for the FEA analysis is listed in the Table 4.3. The same materials for the magnets and the spacer used in Tufts design are used here. The analysis is also shown for 10 magnetic arrays in the air medium. The results of 2D FEA analysis in Figure 4.6 shows the distribution of the inner and outer magnetic flux(IB_r and OB_r) in both radial and Z direction. The average radial magnetic flux values within the coil regions are show in the Table 4.3.
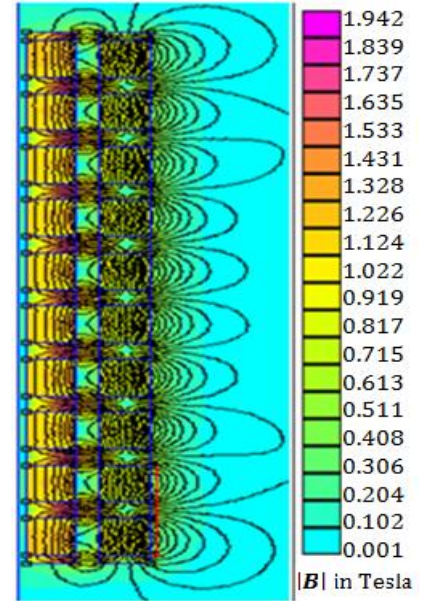
Figure 4.6 Radial Magnetic flux

Table 4.13 : Specifications and results for the Specified Design (Max diameter of 3.5in)

G(mm)	R$_1$(mm)	R$_2$(mm)	H(mm)	R$_3$(mm)	R$_4$(mm)	L(mm)	IB$_r$(Tesla)	OB$_r$(Tesla)
5	2.5	20	10	25	42.5	22.5	1.34	0.56

4.6.2 Average velocity of the rail and sleeper:

As the freight train moves on the track the track deflects due to the moving load of the train. This deflection depends on the parameters like load exerted by the train, velocity of the train and the track substructure properties. The deflection of a typical track is around 5mm to 7mm for a loaded train moving at 25mph [60,70,71&73]. The vertical rail deflections for different conventional ballast tracks (classified like softer, soft, stiff and stiffer based on the track substructure properties) are listed in the Table 4.4[71]. These deflections are measured by running a train with wheel loads of 5kPa to 15kPa. Based on these deflections (5kPa to 15kPa) the other deflections (15kPa to 30kPa) are estimated using curve fitting. The typical fully loaded train exerts a wheel load of around 20kPa to 25kPa [70]. The Table 4.4 gives a clear insight that the vertical track deflection ranges from 3mm to 10mm and typical value will be around 6mm to 7mm.

Table 14.4 : Vertical Deflection of different tracks for various wheel loads

Load Track	5(kpa)	10(kPa)	15(kPa)	20(kPa)	25(kPa)	30(kPa)
Softest track	3.18	4.71	6.24	7.78	9.29	10.82
Soft track	0.58	1.50	2.42	3.34	4.26	5.19
Stiff Track	1.08	1.67	2.25	2.83	3.41	4.03
Stiffest Track	0.73	1.19	1.65	2.11	2.56	3.02

The Figure 4.7 shows the Vertical rail deflection in time domain. This is based on the experiments done using particle image velocimetry for a fully loaded train moving at 16km/hr[73]. The figure clearly depicts that the defections are caused periodically due to the combined loads of the two wheels of a train bogie. The frequency depends on the length of the train carts and the distance between two bogies. The track velocity will not be more periodic for the fast moving trains like around 50km/hr, since the freight trains move with a maximum speed of 40km/hr the track displacement can be assumed periodic.
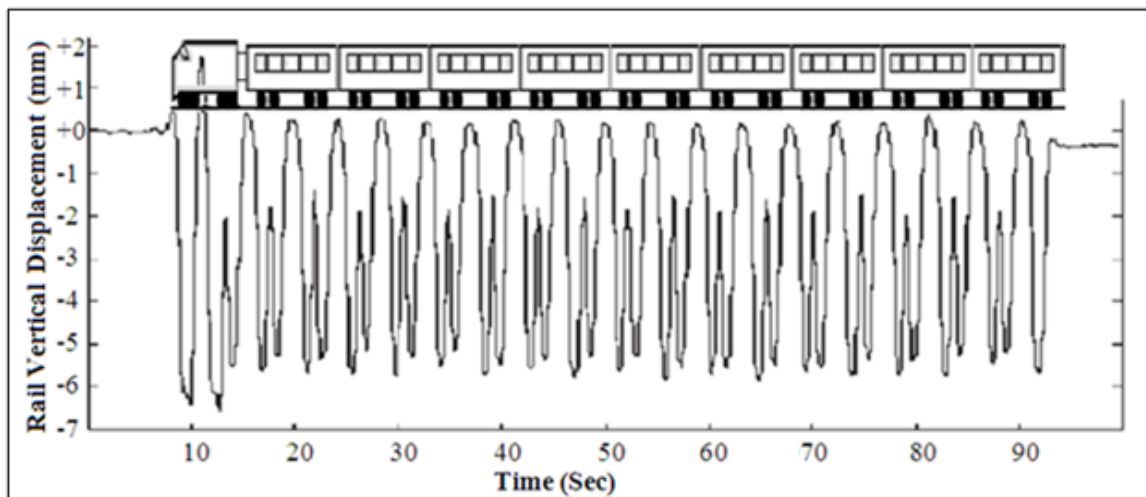
Figure 4.7 Track deflections due to loaded train moving at 16Km/hr [73]

The displcement and the velcoity profiles of the track vibration are drawn in the Figure 4.8. The profiles are drawn based on the experimental results from different literatures[60-73]. This figure can be used to estimate the root mean square and average velocity over a time period of T $(T_a + T_p)$ which will be used for estimating the power generated.

Asuming the velcoity profile is sinosoidal the root mean square V_{rms} can be calculated by

$$V_{rms} = \frac{V_{max}}{\sqrt{2}}$$

The maximum velocity V_{max} for each sinosoidal peak is calculated based on piece wise linear approximation from zero to maximum velcoity.

As the Figure 4.8 shows the track will not be under deflection during certain period (T_p) where there is no wheel loads exerted on it.

Then the average velocity can be calcuted based on thr root mean sqaure velociy

$$V_{avg} = \frac{\sqrt{3} V_{rms}}{\sqrt{2}} \qquad 4.5$$

$T_a = Active\ time\ period$

$T_p = passive\ time\ period$

$T = total\ time\ period$
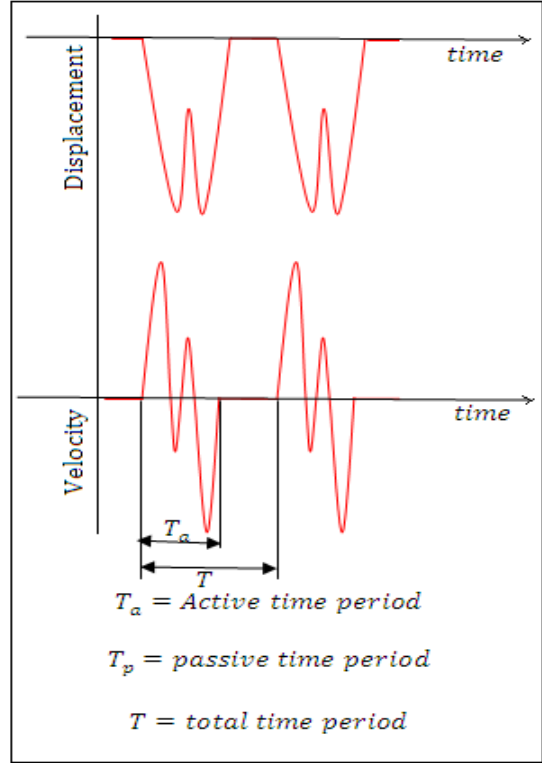
Figure 4.8 Displacement and velocity profile of the track

Using the above method the average velcoities are calculated for three different type of loadings like empty train, moderastely laoded train and fully loaded train moving at 25km/hr are listed in the Table 4.5

Table 4.15 : Average velocities of the track for different train loadings

Loading type	$V_{V_{T_a}\ avg}\ (mts/sec)$	$V_{V_T\ avg}\ (mts/sec)$
Empty train(deflection-3mm)	0.017	0.016
Moderately loaded(deflection-7mm)	0.045	0.042
Fully loaded (deflection-12mm)	0.073	0.068

4.6.3 Volume of the coil winding (V_{coil})

A copper coils are place in the air gap (G) between the inner and outer magnetic array rings. This copper coil is placed in concentric with the high magnetic permeability spacer and is of the same length of it as shown in Figure 4.4. A coil made of copper wire with gauge 30 AWG and diameter(d) of 0.9068mm was used in the analysis and the length l is given by Eq. 4.6

$$l = \pi D_c N_t \qquad 4.6$$

Where D_c is the average diameter of the coils and N_t is the number of turns which is determined as

$$N_t = \frac{\pi}{2\sqrt{3}} \frac{A_c}{A_w} = \frac{\pi}{2\sqrt{3}} \frac{4A_c}{\pi d^2} = \frac{2}{\sqrt{3}} \frac{A_c}{d^2} \qquad 4.7$$

Where d is the diameter of the wire, and A_c and A_w are the cross-sectional areas of the coil and wire, respectively[75].

The number of turns N_t for both the designs are determined from Eq 4.7 and listed in the Table 4.6

Table 4.16 : Copper coil dimensions and No of turns

Design	Average diameter of inner coil (mm)	Average diameter of outer coil (mm)	No of turns of inner coil (N_t)	No of turns of outer coil (N_t)
Design 1	37.5	77.5	70	70
Design 2	22.5	45	70	70

The average voltage of one coil will be

$$V = \frac{2\pi B_r v_z D_c A_c}{\sqrt{3} d^2} \qquad 4.8$$

and the average power will be

$$P = \frac{\pi^2 \sigma B_r^2 v_z^2 D_c A_c}{2\sqrt{3}} \qquad 4.9$$

where B_r is the average radial magnetic flux with in the copper coil winding region and v_z is the average track deflection velocity i.e. V_{track} which is calculated using Eq. 4.5.

4.7 Results

The required No of coils (N_{coil}) and the length of the Electromagnetic Harvester for the power requirements of 10watts, 250watts and 3000watts are calculated in this section.

4.7.1 No of coils and length of EMH required

The No of coils (N_{coil}) required to generate required amount of power P_{req} can be calculated from by dividing the required power with the power produced per unit coil. The equation is below.

$$P_{req} = N_{coil}P \qquad\qquad 4.10$$

$$N_{coil} = \frac{2\sqrt{3}P_{req}}{\pi^2 \sigma B_r^2 v_z^2 D_c A_c} N_{coil} \qquad\qquad 4.12$$

Based on No of coils(N_{coil}) the total length of the EMH can be determined from

$$L_{total} = (N_{coil} + 1)(H + L) \qquad\qquad 4.12$$

The estimated No of coils(N_{coil}) required and the length(L_{total}) of the electromagnetic harvester for power requirements 125watts and 3000watts for both the designs are given in the Tables 4.7 & 4.8.

Table 4.17 : Estimated No coils and Length of harvester for Tufts Design (Max Dia 6in)

Track load	Track deflection and velocity (7 mm and 0.45mts/sec)				Track deflection and velocity (12mm and 0.73mts/sec)			
Power required (W)	Power per coil (W)	No of coils	Power per unit length (W/in)	Length of the EMH(in)	Power per coil (W)	No of coils	Power per unit length (W/in)	Length of the EMH(in)
10 watts	Inner 2.01 Outer 0.24	5	1.31	7.6	Inner 5.30 Outer 0.63	2	4	2.5
250 watts		111	1.31	142		42	4	53.7
3000watts		1330	1.31	1700		506	4	648

Table 4.18 : Estimated No coils and Length of harvester for Specified Design (Max Dia 3.5in)

Track load	Track deflection and velocity (7 mm and 0.45mts/sec)				Track deflection and velocity (12mm and 0.73mts/sec)			
Power required (W)	Power per coil (W)	No of coils	Power per unit length (W/in)	Length of the EMH(in)	Power per coil (W)	No of coils	Power per unit length (W/in)	Length of the EMH(in)
10 watts	Inner 1.21 Outer 0.24	7	1.12	10.23	Inner 3.18 Outer 0.63	3	2.9	5.1
250 watts		173	1.12	222		66	2.9	85
3000watts		2070	1.12	2648		787	2.9	1006

4.8 Discussions for design improvements to high power density

In the Tufts design the radial magnetic flux density(B_r) is maximum only in the air gap region(G) next to the steel spacers as shown in Figures 4.5 & 4.6 where the copper coils are

initially placed. Once the coils slide up or down the radial magnetic flux density exerted on the coil is decreased abruptly to small value which can also seen in Figures4.5 & 4.6. When the coil moves up and down due to the track displacement the coil will move out of the maximum flux density region and the power produced in the coil will be decreased. In the tufts design the radial magnetic flux within the initial coil region is very high but decreases to a very low value as coil moves up and down. Because of this highly non uniformity of radial magnetic flux within the range in which the coil moves when the track is displaced the power produced is less. Hence the design is not optimized.

More power can be generated with the similar design or magnets orientation by doing significant changes which are discussed below

1) For the Tufts Design the coil moves out of phase if the deflection is large and generates less power. The increase in coil length or continuous coil tube results in more amount of coil always being in the maximum flux density region. In fact, the number of coil phases also has significant influence on the power, which needs to be optimized.

2) The thickness of the spacer(H) compared to its radius(R_2 and R_4) can be optimized. We found that there is an optimal value for that parameter. Besides, the dimension of the air gap(G) for the coil, which is corresponding to the volume of conducting coil. A table below shows that the change in the spacer thickness for the same magnet thickness will significantly increase the power. This space thickness can be optimized for a fixed magnet thickness.

Table 19 : Power generated for different spacer thickness for Specified Design

Track load Specifications				Track deflection and velocity (7 mm and 0.45mts/sec)			Track deflection and velocity (12mm and 0.73mts/sec)		
L (mm)	H (mm)	Radial Magnetic flux		Power per coil (W)		Power per unit length (W/in)	Power per coil (W)		Power per unit length (W/in)
		Inner	Outer	Inner	Outer		Inner	Outer	
22.5	10	1.34	0.56	1.21	0.24	1.12	3.18	0.63	2.9
22.5	22.5	1.12	0.45	1.74	0.34	1.22	4.57	0.88	4.14

3) A new configuration like the radial magnets can be used which will increase the power due to increase in radial magnetic flux density. The Figure 4.10 shows the configuration of both with and without radial magnets for a double layer. The tufts design is similar to

the double layer configuration with axial magnets in Figure 4.10. The 2D FEA analysis in Figure 4.11 shows the significant change in the radial magnetic flux density in the coil region due to the replacement of spacer with radial magnets. On a whole the radial magnets configuration will increase the power up to 65% over the axial magnets[76].
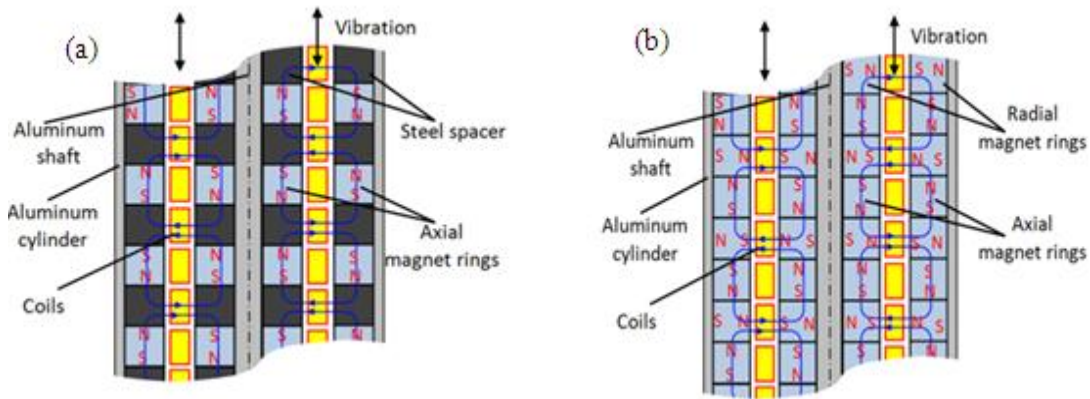
Figure 4.9 Different configurations (a) double-layer with axial magnet (similar as Tuft patent)   (b) double-layer with both radial and axial magnets
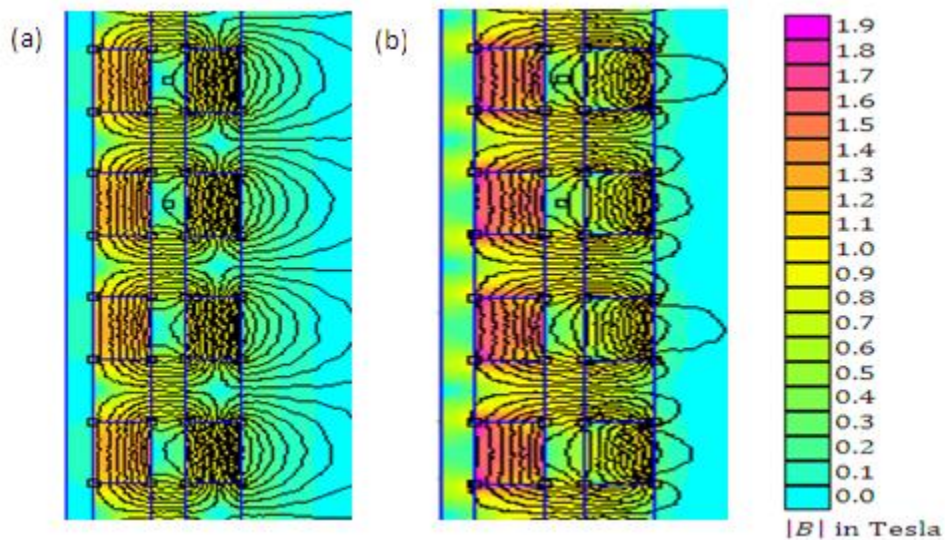
Figure 4.10 FEA result of different configurations: (a) double-layer with axial magnets, (b) double-layer with axial and radial magnets

4) A rack and pinion mechanism can be used to convert the vertical track displacements to rotational motion, and gear transmission to enhance the rotational speed by using gear ratio. This enhanced rotational motion can engage the electric generator to generate the power. Since the train wheels and their loads are unevenly distributed the input to the harvester will be erratic, so a flywheel can be used to get a constant output power. This

design is capable of harvesting a power of more than 50 watts depending on the gear transmission ratio and generator characteristics.

4. 9 Conclusions:

The required parameters radial magnetic flux, velocity of the track vertical displacement and volume of the copper coil/conductor are analyzed for adapting the tufts Electromagnetic harvester design to railway energy harvesting. The radial magnetic flux analysis is done using 2D FEA software *Finite Element Method Magnets.* Using these parameters the power generated per unit coil of the Tufts EMH design is estimated based on which the No of coils required and length of the EMH to harvest given required power of 250watts and 3000watts are calculated. It is shown that the design is not optimized and valid discussions were given to make the EMH design better and optimize.

Chapter 5 - High efficient and reliable vibration energy harvester using "mechanical motion rectifier"

5. Introduction

In the previous chapter the energy harvesting capacity of the existing models of linear electromagnetic harvester from the railway track vibrations is assessed. The results shows that the power density per unit volume of the linear energy harvester is low because of the low track vibration speed and also erratic (pulse like) vibrations of the track due to the large gaps between two pair of train wheels. To harvest more energy from the railway track vibration that is sufficient to power the track side infrastructure a new design which can magnify the low speed vibration and efficiently harvest energy from the pulse like vibration has to be designed.

Typical Rotational Energy harvesters have a transmission system for motion magnification which will increase the rotational speed of the generator but when used to harvest form the irregular and pulse like vibrations they have low efficiency and less life time[12]. The section 5.1 in this chapter has a detailed description of the disadvantages of the conventional rotational harvesters for irregular vibration input.

In this chapter we proposed a new harvester design which can efficiently harvest energy from irregular and pulse like railway track vibrations. The designed harvester has a "mechanical motion rectifier" which will make the irregular upward and downward track vibration into a unidirectional motion and a fly wheel which can stabilize the generator speed by storing the energy during the high speed vibration pulse and releasing the stored energy to rotate the generator during the low speed vibration. This novel design is very high efficient and high reliable and can produce the DC current directly from the irregular vibrations without any electrics. The design is not just limited for the railway track vibrations energy harvesting it can also be extend to energy harvesting from any irregular vibration input like ocean wave etc. The detailed description of the new harvester is presented in the later section of the chapter.

5.1 Limitation of the conventional rotational energy harvester:

The conventional vibration energy harvesting system is typically composed of a mechanical motion magnification system, rotational generator, an electrical rectifier, and power regulator and energy storage element, as show in Figure 5.1.
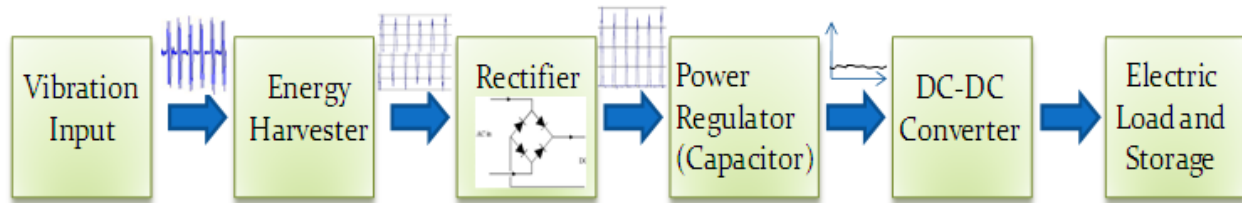
Figure 5.1: Typical vibration energy harvesting system

The motion magnification system will be mainly by rack and pinion or ball screw or hydraulic which converters the up and down vibration into oscillatory motion[76&77]. Also there will be a gear transmission to magnify the motion before connecting it to the generator shaft. The rotational generation with a rated voltage equal to the peak vibration voltage oscillates to produce a low quality output power in the form of pulses[18]. Then this low quality power is rectified using a voltage rectifier and stored in the storage unit to use when required. A rack and pinion rotational type harvester for railway track vibration energy harvesting is investigated [12] which showed the output power is very low and of poor quality. The following are the problems with the conventional rotational energy harvester when used to harvest energy from irregular and pulse like vibration inputs mainly the railway track vibrations.

1. The first problem is related with the low efficiency since the characteristics of railway track vibration are not considered. Figure 5.2 (a) shows that track vibration, which is in pulse form, large vertical deflection happens when the train wheel passes by, and there is little or no track motion before another wheel passes. Therefore, to harvest 2 watts energy, the harvester(generator) has to be 20 watts or more, as shown in Figure 5.2 (b) In this way, the electric generator can't work on the efficient speed range. In conventional harvester design, we have to choose a **large generator** rated at peak vibration power, whose capacity is often ten times more than the average power output, yielding extremely low efficiency and low power quality, such as ~30% efficiency[12].

70
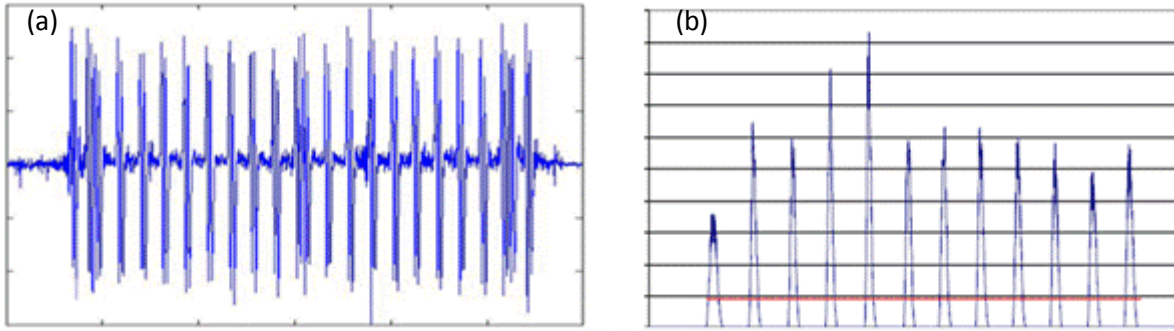
Figure 5.2: (a) Typical deflection velocity of the sleepers is in the form of pulses (b) Traditional energy harvesting technology, the instant power is large but the average power is very small

2. The second problem is the bidirectional oscillation will cause large impact force, backlash, and frictions, causing the fatigue or leakage and reducing the efficiency. Figure 5.3 shows the failure of a rack pinion element due to large impact force in our early prototype of regenerative shock absorber based on oscillatory rotation motor.

Figure 5.3: Failure of rack in the conventional harvester

3. The third problem is the reciprocating motion which makes the integration of fly wheel very hard. Fly wheels will increase the efficiency from 50% to over 70% in many cases. Integration of flywheel is not possible into any current vibration energy harvesters because of oscillation.

4. The fourth problem is the parasitic loss in the electric components. For example the semi-conductor diodes usually have a forward voltage drop 0.7V, and thus there is 1.4 V forward voltage drop in an AC/DC rectifier bridge, which causes parasitic energy loss. If the voltage generated is low then the useful voltage after rectification will be very low.

To overcome all these technical disadvantages of the convention rotational energy harvester to harvest energy from the pulse like railway track vibrations a new type of energy harvester is designed. All the above questions will be solved in the proposed energy harvester

5.2 Description of Proposed Innovations

Figure 5.4 shows the concept of the proposed new energy harvester. The zoomed view in the Figure 5.4 shows the detailed description of the assembly for the new design. The harvester design mainly composed of a transmission mechanism, an electromagnetic generator, and a fly

wheel. The transmission mechanism includes three shafts with three spur gears, a pair of rack and pinion, and two roller clutches. The two racks move together in up and down direction. The roller clutches here have a similar function as the one used in bicycle gears, allowing the motion transmission from one direction only.
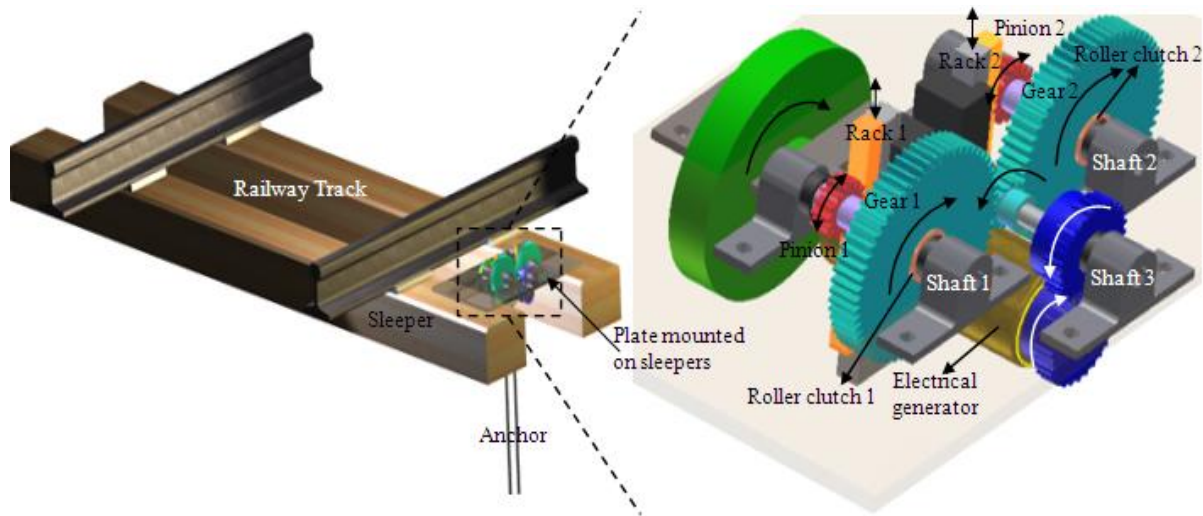
Figure 5.4: Concept of the proposed energy harvester for Railway track vibrations

For more convenience the working principle is explained based on Figure 5.5. The yellow solid line in Figure 5.5 shows the motion transmission path when the two racks move downward together, the racks drive both pinions to rotate in opposite direction but only Gear 1 on Shaft 1 is engaged through the Roller Clutch 1, thus Gear 1 will drive Shaft 3 in the counter-clockwise direction. Due to the disengagement of Roller Clutch 2, Gear 2 can rotate in the clockwise direction together with the gear on Shaft 3 even Shaft 2 is rotating in the counter-clockwise direction.

Similarly, The yellow dotted line in Figure 5.5 shows the motion transmission path when the two racks move upward together, the racks drive both pinions to rotate in opposite direction but only Roller Clutch 2 is engaged to
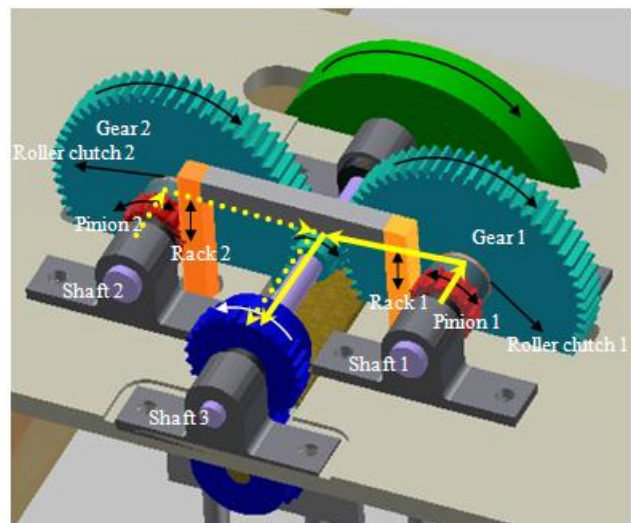
Figure 5.5: Description of the working principle

lock Shaft 2 and Gear 2, and then drive Shaft 3 in the counter-clockwise direction. Meanwhile, Roller Clutch 1 will disengage Shaft 1 and Gear 1 and the Gear 1 will rotate in clockwise direction even though shaft 1 is rotating in counter-clockwise direction.

Therefore, no matter the racks move in upwards or downwards direction, the mechanism always enable shaft 3 to rotate in one direction, and hence the electromagnetic generator will rotate in one direction. Moreover, if shaft 3 (and generator) rotates faster, both roller clutches will be disengaged. The feature enables a unique possibility to combine fly wheel into the vibration energy harvester to make full use of the feature of erratic environmental vibrations. At high vibration velocity some kinetic energy will be stored in the fly wheel; and when the vibration velocity is low or zero, the kinetic energy stored in the fly wheel can be released to drive the electric generator to produce electrical power as of in the high vibration velocity period. Therefore, we can use a flywheel to reduce the speed fluctuation of the generator, and high-quality DC voltage can be produced directly from vibration without electrical rectifier.

In real application, the generator, shafts, gears, and pinions can be mounted on a plate attached to the sleepers, and the racks can be anchored at certain depth into the ballast such that there will not be any relative motion between the rack and the plate mounted. When the train passes by, the pinions-shaft-gears-generator system will vibrate together with the track deflection, and the racks will not move or not move much. So the erratic track vibration in both up and down directions will drive the electrical generator in one direction to produce high-quality electricity.

5.3 Innovative attributes of our approach

The proposed design is totally different from all the vibration harvesters in literature. By converting the irregular reciprocating oscillation of track vibration into regular unidirectional rotation of the electrical generator and allowing the integration of flywheel, it solves the fundamental challenge in the vibration energy harvesting due to varying frequencies and low, alternating velocities, and thus achieving high efficiency and reliability.

Such a transmission design is actually a "mechanical motion rectifier", where the roller clutch is analog to semi-conductor diode in the electric voltage rectifier. It rectifies the irregular reciprocating vibration in a similar way as the electric voltage rectifier regulates an AC voltage. This leads to the unidirectional motion of the generator shaft though the rack and pinion has irregular upward and downward motion.

73

Since the "mechanical motion rectifier" like transmission system makes generator rotates in one direction, we can integrate fly wheel on the high speed generator shaft for more inertia. Moreover, if the generator rotates faster at instant small vibration speed, both roller clutches will be disengaged, and the kinetic energy stored in fly wheel will be released to drive electrical generator to produce electricity. Therefore, we can use a flywheel to reduce the speed fluctuation of the generator and increase the efficiency and power quality. Other rotary inertia acts as part of the fly wheel, reducing motion fluctuation of the harvester.

If a DC generator is used, the proposed new energy harvester can directly produce a DC power from irregular vibrations without electrical voltage rectifier. However, the mechanical motion rectifier and the flywheel is not a substitute of electrical voltage rectifier and the power regulator(capacitor). The advantages go well beyond producing a DC voltage, as listed in the following and summarized in Table 5.1.

1. <u>High Efficiency</u>: The traditional vibration energy harvester usually has large peak power and small average, as shown in Figure (5.2). Therefore, **the electric generator** has to be selected according to the peak power or 10 times or more than the average vibration, and during the majority of the time the generator works in a speed or load far from the most efficient operational condition. As a result, the efficiency is super low. The proposed design creatively integrates the **flywheel** into the vibration energy harvesting which stabilizes the speed of the generator. The electrical generator will rotate in one direction with small fluctuations. Therefore, the generator will work mostly in a more efficient speed range. This feature is especially valuable to the track vibration harvesting because the train-induced deflection is in the form of **short-time large-peak pulses**. The traditional harvester designs are extremely inefficient.

2. <u>High Reliability</u>: In traditional vibration harvester design, the **moving mass and inertia** always has a negative effect on the harvester reliability. This is because of the irregular oscillation will create large impact force and friction on the transmission gears, chain, or shaft and also the inertia will always be negative. In the proposed novel design, Since almost all the components, including the shafts, spur gears, flywheel, and generator, except the pinions and rack, will rotate unidirectional and also the influence of rotation inertia changes from negative to positive side, acting similarly as the fly wheel the impact forces on the gear

teeth, bearings, shafts, or other mechanisms are greatly reduced; therefore the reliability and service life of the system are highly increased.

3. Unlike the transitional vibration energy harvester working in oscillation, the proposed energy generator will rotate in one direction, no matter if the vibration is in upward or downward direction. Therefore, we can directly produce high quality DC power **without electrical rectifier or power regulator**. We don't need to worry about the forward voltage drop in the semi-conductor diode or switching electronics.
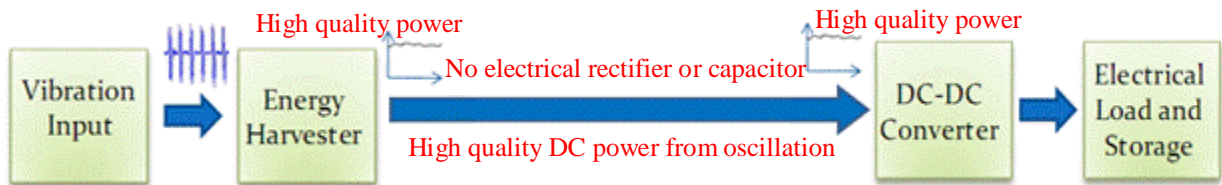
Figure 5.6: Invented energy harvesting system with mechanical rectifier. Compared with Figure 5.1, the invented technology can significantly simplify to vibration energy harvesting system and improve the efficiency and reliability to produce high quality power output.

Table 5.20 Advantages of the invented energy harvester over the conventional harvesters

Feature	Proposed Energy Harvester	Traditional Energy Harvester
Mechanical motion	Unidirectional rotation	In oscillation
Electrical generator	Relative steady speed at high efficiency	Variable speed at low efficiency
Motion inertia	Acts as temporary energy storage & helps reduce the speed fluctuation	Large impact force and reduce the reliability
DC power	Directly produce DC without electrics	Need electrical diode and capacitor

5.4 Design calculation and procedure

5.4.1 Motor Characteristics

A DC geared motor is used since the designed energy harvester can produce DC power directly. The geared motor shown in Figure 5.7 is considered for this design, because of its simplicity and efficiency. Also the selected motor has an extended shaft at the higher speed side to attach a flywheel. The specifications of the motor are shown in Table 5.2

Figure 5.7: EBM geared motor

Table 5.2 EBM geared motor specification

Manufacture	EBM-Papst		Gear Type	Planetary
Model	BCI 63.55 PX 63-9		Nominal Torque	2.2 [Nm]
Power Output	117 [W]		Nominal Speed	367[Rpm]
Gear Ratio	9:1		Nominal Current	4.9 [A]

The performance of the motor/generator tested on lay machine with different rpm and shunt resistances is shown in the Figure 5.8[78]. The figure shows power and shunt resistance relationships. Higher power output is presented with lower shunt resistance. The power can be reached to 100 watts at 2900 motor rpm with shunt resistance 0.8 ohm.
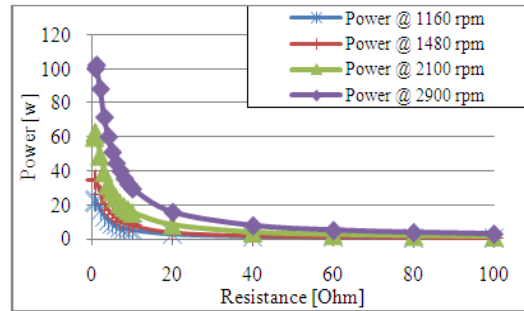
Figure 5.8: Power vs. resistance at different

5.4.2 Flywheel Selection

The purpose of the flywheel within the system is to achieve more steady rates of power generation. The flywheel is placed at the high speed side of the generator shaft where it can reach the highest rotational velocity to store the most energy, while also being placed in a position of least resistive forces from neighboring gear reductions.

The flywheel is designed to keep the harvester system into constantly harvesting power above 80% of its maximum harvesting potential, so that once the harvester reaches its 93watt harvesting potential(max for the motor in Figure 5.7), the harvester will continuously and smoothly harvest energy between 74.4 and 93Watts. The time increment between harvester inputs from the rail is roughly 0.5 seconds. The energy balance equation to solve for flywheel dimensions is as follows.

$$Energy = \frac{1}{2}I(\omega_1^2 - \omega_2^2) = P_{avg}\Delta t \tag{5.1}$$

Where ω_1 is 345.6 radians per second, ω_2 is 272.1 radians per seconds corresponding to 93watts and 74.4watts of power respectively, P_{avg} is the average mechanical power required from the

flywheel between inputs which is (0.9)(117) Watts, and Δt is the time between inputs which is assumed 0.5 seconds.

$$I_{minimum} = \frac{2 \cdot P_{avg}\Delta t}{(\omega_1^2 - \omega_2^2)} = \frac{2 \cdot 0.9 \cdot 117 \cdot 0.5}{345.6^2 - 272.1^2} = 0.00231 \; kg \cdot meter^2 \tag{5.2}$$

With the necessary mass moment of inertia for the flywheel known, flywheels of various dimensions can be calculated using the equation

$$I_{flywheel} = \frac{\pi}{2}\rho h r^4 \tag{5.3}$$

Where ρ is, h is flywheel thickness, and r is flywheel radius.

Various commercially available flywheels were compared for appropriateness. A Cast Iron V-belt pulley of density 7874 kg/meter³ and 4.45" diameter (0.0562 meter radius) was analyzed for appropriateness. Figure 5.9 depicts the flywheel.

Figure 5.9: Fly Wheel

The moment of inertial of the flywheel is estimated as follows

$$I_{flywheel} = \frac{\pi}{2}\left(7874\frac{kg}{m^3}\right)(0.02m)(0.0565\;m)^4 = 0.002523 \; kg \cdot meter^2 \tag{5.4}$$

This flywheel is therefore likely to be capable of meeting our energy needs, since the moment of inertia 0.0025 is larger than 0.0023.

5.4.3 Roll Clutches

Roller clutches are unidirectional bearings which engage and lock when spun in one direction. The roller clutches used in this harvester are One-Way Locking Steel Needle-Roller Bearings these bearings roll freely in one direction, but they lock to transmit torque when the rotation of the shaft is reversed and there by allows only unidirectional shaft rotation. These bearings do not support radial (perpendicular to the shaft) loads.

Figure 5.10: Roller Clutch

The roller clutch selected for this project is capable of withstanding 9Nm of torque which is within the safety limit. The roller clutch has a 0.5" bore and a 0.75" outer diameter and maximum of 17000rpm and minimum backlash.

5.4.4 Pillow Blocks

Shaft supports in this design will be conducted through use of bearing pillow blocks. To minimize bending stress exerted by shaft components each individual shaft in the gear train is mounted by two pillow blocks at each end as simply supported shafts. Same type of pillow blocks is selected for all the shafts. The pillow block has a capacity of 2500 pounds and rotational speed of up to 5800rpm.

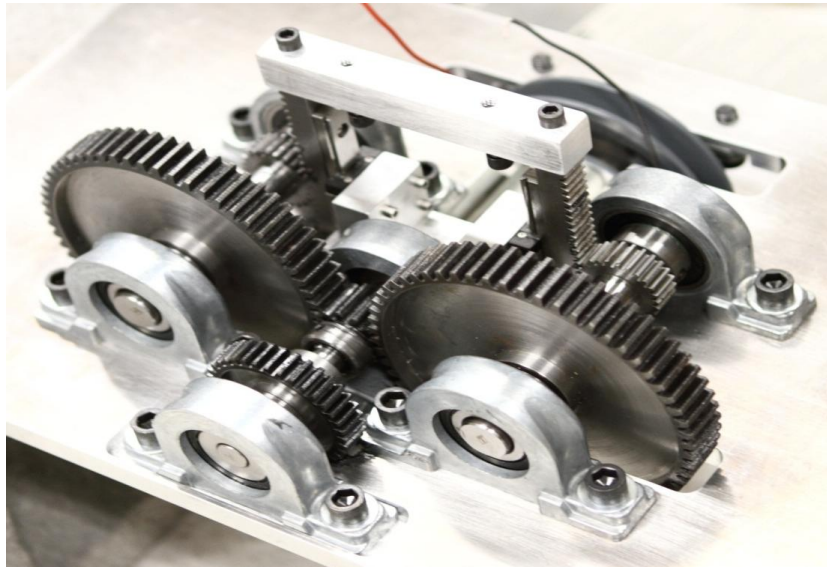The Figures 5.11 and 5.12 shows the final full-scale prototype.

Figure 5.11: Final full-scale prototype of the Energy harvester with "mechanical motion rectifier"
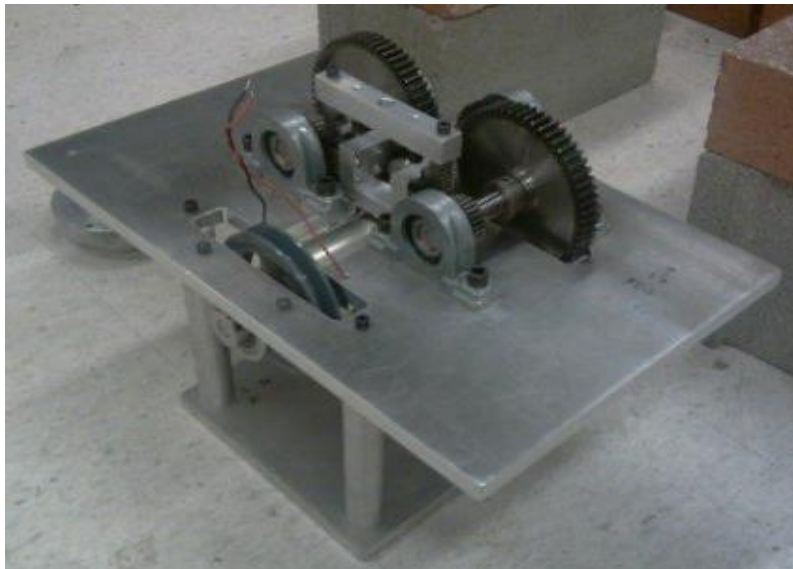

Figure 5.12: Final full-scale prototype with base plate used for experiments

5.5 Experimental Procedure:

The novel energy harvester deign is preliminarily tested in lab for studying the unique behavior of the Mechanical motion rectifier and flywheel combination. The tests on the energy harvester are conducted using a servo-hydraulic testing system, "858 Mini Bionix II" shown in the Figure 5.13. The "858 Mini Bionix II" system used is designed to easily run fatigue cycles on biomaterials at frequencies up to 30 Hz. This system can give the vertical displacement over a range of 1-30cm and the load cell has a capacity up to 4kN.

The Figure 5.13 shows the experimental setup, the energy harvester prototype is mounted on the servo-hydraulic testing system. The gear train and generator components are fixed by bolting the base plate to the bottom of the testing system. The rack bridge is screwed to the movable top of the system which is moved by the two hydraulic cylinders on the sides. The Mini Bionix II fatigue cycle loading machine can apply various oscillating loads at different frequencies onto the rack. The axial systems of Bionix II accurately measures and controls static and dynamic testing. The System is connected to a computer which records the parameters like displacement and force.
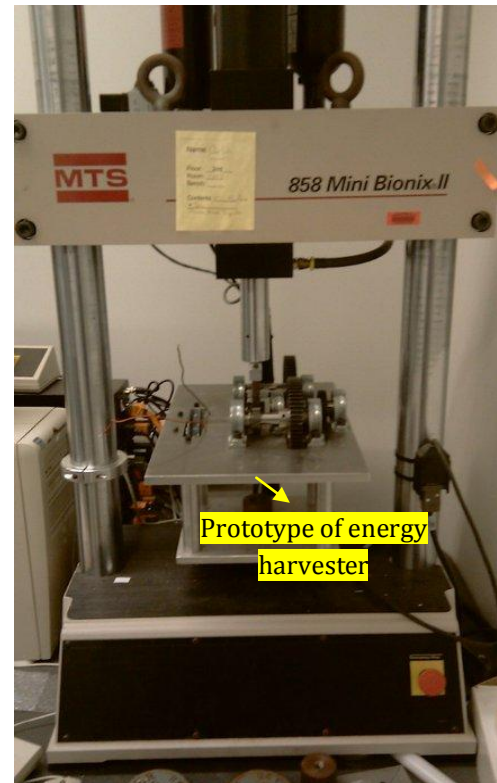
Figure 5.13: 858 Mini Bionix II

Oscilloscope is used to measure the voltage output of the motor when testing the device at varying frequencies and resistance loads. A voltage output is generated by the electric generator once the testing system moves the rack up and down.

The experiments are done for sinusoidal displacement inputs of three different amplitudes 0.25inch, 0.5inch and 0.75inchs and at frequency 1Hz, 0.5Hz and 0.3Hz respectively. For each of the sinusoidal displacement input the voltage out for open circuit and three different resistors 24ohms, 12ohms, and 6.2 ohms connected to the generator are measured. In each trial, generator voltage, device input, device displacement, rack peak velocity, and forces applied onto the device are recorded.

Since the capacity of the load cell in the "858 Mini Bionix II" is only 4kN, the experiments can only be carried for a frequency of up to 1Hz, though a detail study needs till 4Hz.

5.6 Experimental Results:

In this section the results of the experiments conducted at three different displacements inputs of the rack 0.25inch(1Hz), 0.5inch(0.5Hz) and 0.75inch(0.3Hz) for different power resisters are presented. The graphs are plotted for various parameters like voltage, force etc to show the behavior of the new energy harvester design with mechanical motion rectifier and flywheel.

5.6.1 Quarter inch (0.25) displacement input

Most of the good quality railway track has a track vibration of displacement of around 0.25 inch when the moderately loaded trains pass by. The experiments were conducted by giving an input of 0.25inch sinusoidal displacement to the rack. The Figure 5.14 shows the voltage output for different power resistors at 0.25 inch rack sinusoidal displacement. The Figure clearly shows that the output voltage is always positive and never reached zero volts because of the property of "mechanical motion rectifier" to behave as voltage rectifier and flywheel as power regulator.
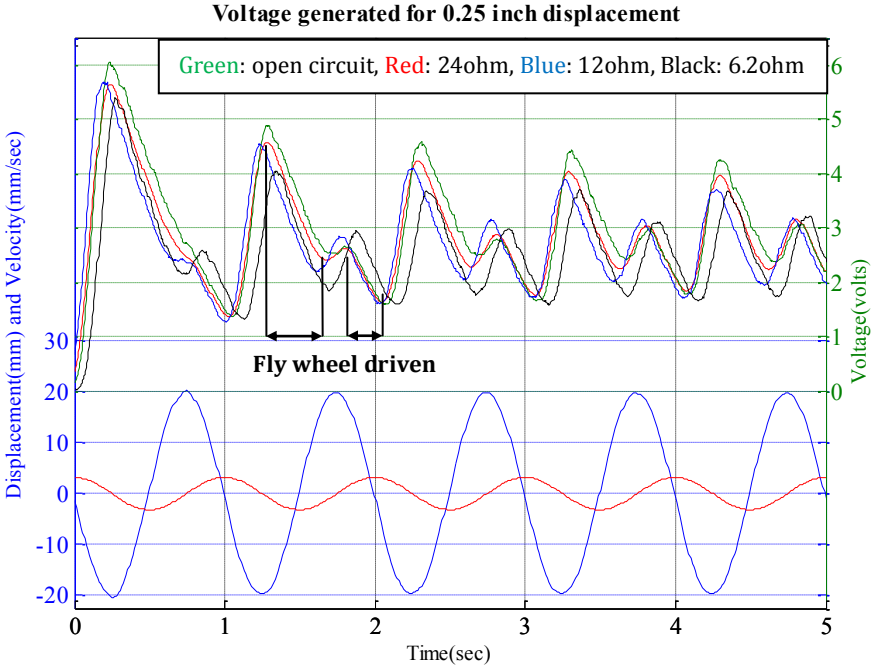

Figure 5.14: Voltage generated for 0.25in rack displacement at frequency 1Hz for various resistors

The force vs. time is plotted for the same 0.25inch sinusoidal displacement input in Figure 5.15. The Figure shows that the initial impact force in the first cycle is much larger than the force required in the later cycles. This behavior is mainly due to the flywheel, since the displacement is very small the acceleration is large, so the fly wheel needs more initial torque to start rotating and once the fly wheel reaches a certain rotational speed the inertia of the fly wheel and the other gear and will help to reduce the torque required, hence the force required will be much smaller.

The force vs. velocity is plotted for the same 0. 25inch sinusoidal displacement input in Figure 5.16. The Figure also shows that the initial impact force is very high and low in the later cycles. It clearly demonstrated the engagement and disengagement of the roller clutches. The loop has an idle period where the force required is at minimum that is when both the roller clutches are disengaged because the velocity of the generator shaft is higher than the input speed and the generator is driven by fly wheel

The Figures 5.15 & 5.16 shows the nonlinear operation of the energy harvester i.e. partially driven by the driving system and partially driven by the flywheel, hence the difference in the force required for upward motion and downward motion is very large. The overall efficiency of the system at 1Hz frequency for different power resistors used is shown in the Table 5.3.

Figure 5.15: Force required for 0.25in rack displacement at frequency 1Hz for various resistors

81

Figure 5.16 Force-velocity loops for 0.25in rack displacement at frequency 1Hz for various resistors

Table 5.3 overall efficiency of the system at 1Hz frequency for different power resistors

Resistance	6.2	12	24
Mechanical efficiency	24.92	16.37	10.25
Electrical Efficiency	88.9	93.75	96.8
Overall mechanical efficiency	22.16	15.35	9.92

5.6.2 Half inch (0.5) displacement input

The average quality railway track has a displacement of around 0.5 inch when the moderately loaded trains pass by. The experiments were conducted by giving an input of 0.5inch sinusoidal displacement to the rack. The Figure 5.17 shows the voltage output for different power resistors at 0.5 inch rack sinusoidal displacement. Since the frequency is low the flywheel effect is reduced when compared to that of the 0.25inch displacement input, hence the voltage output wave form is oscillating close to zero volts.

The force vs. time is plotted for the same 0.5inch sinusoidal displacement input in Figure 5.18. The figure shows that the initial impact force in the first cycle is slightly higher than the force required in the later cycles. Since the displacement is slightly higher the initial acceleration of the flywheel is not very high and once the fly wheel reaches a certain rotational speed the inertia of the other gear and the fly wheel will help and reduce the torque required and hence the force required will be little smaller.

82

Figure 5.17: Voltage generated for 0.5in rack displacement at frequency 0.5Hz for various resistors
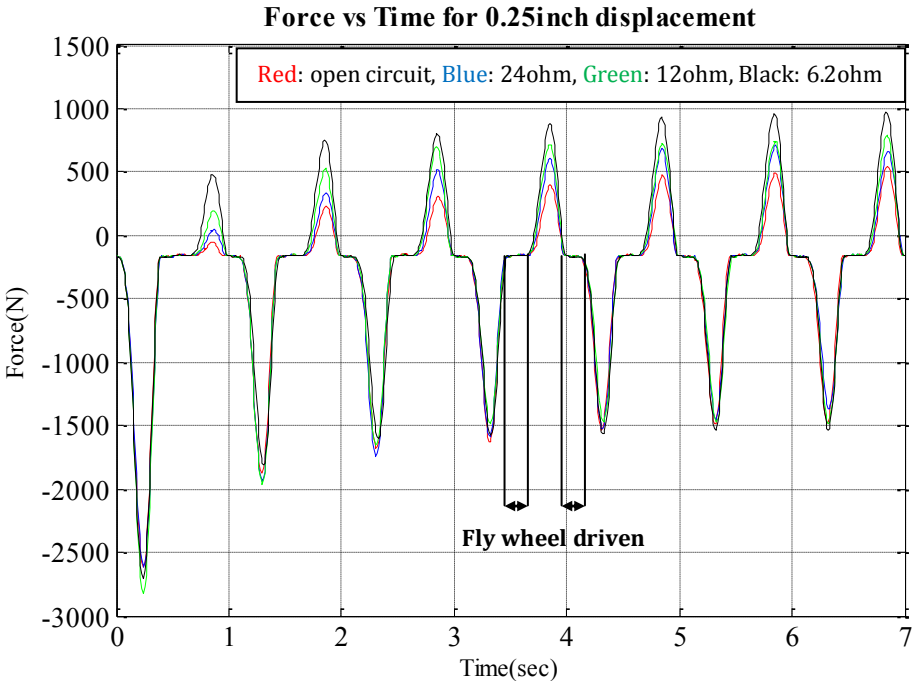

Figure 5.18: Force required for 0.5in rack displacement at frequency 0.5Hz for various resistors
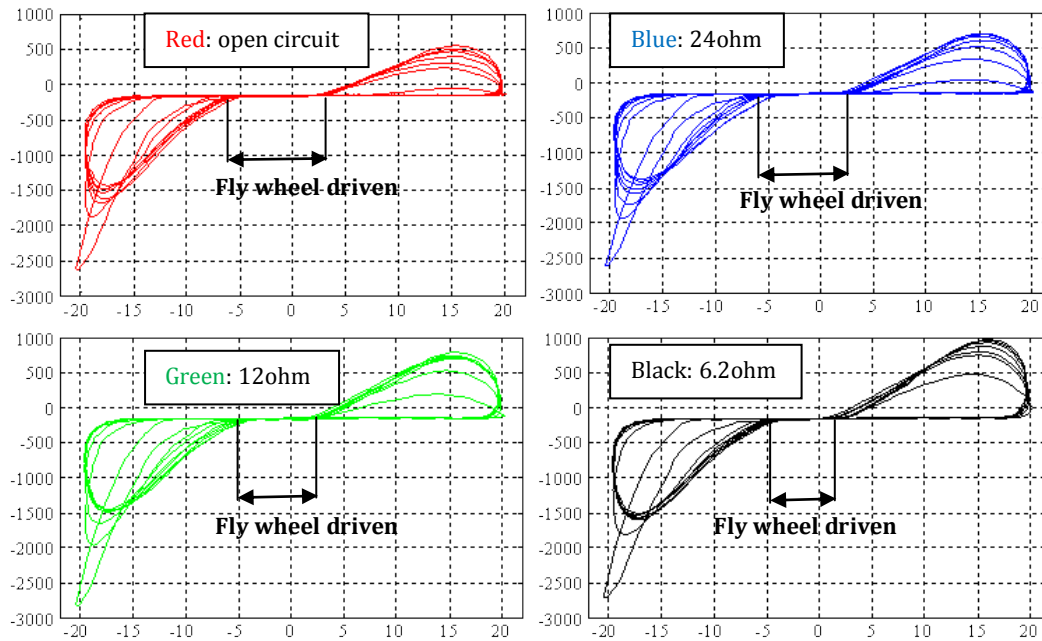
Figure 5.19: Force-velocity loops for 0.5in rack displacement at frequency 0.5Hz for various resistors

Table 5.4 overall efficiency of the system at 0.5Hz frequency for different power resistors

Resistance	6.2	12	24
Mechanical efficiency	18.95	11.36	6.2
Electrical Efficiency	88.9	93.75	96.8
Overall mechanical efficiency	16.85	10.65	6.01

The force vs. velocity is plotted for the same 0.5inch sinusoidal displacement input in Figure 5.19. This figure also shows that the impact force is slightly high than the later cycles. The Figure clearly demonstrated the engagement and disengagement of the roller clutches. The idle period of the loop where the force required is at minimum is when both the roller clutches are disengaged, because the velocity of the generator shaft is higher than the input speed and the generator is driven by fly wheel.

The above Figures 5.18 & 5.19 shows that the there is smooth non linear operation and engagement and disengagement of the roller clutches during the up and down motion of the rack. The difference in the force required for upward motion and downward motion is not very large. The overall efficiency of the system at 0.5Hz frequency for different power resistors used is shown in the Table 5.4.

84

5.6.3 Three forth inch (0.75) displacement input

The poor railway track has a displacement of around 0.75 inch when the moderately loaded trains pass by. The similar experiments were conducted by giving an input of 0.75inch sinusoidal displacement to the rack. The Figure 5.20 shows the voltage output for different power resistors at 0.75 inch rack sinusoidal displacement and 0.3Hz frequency. Since the frequency is very low the flywheel effect is not seen, hence the voltage output wave form is reaches zero volts.
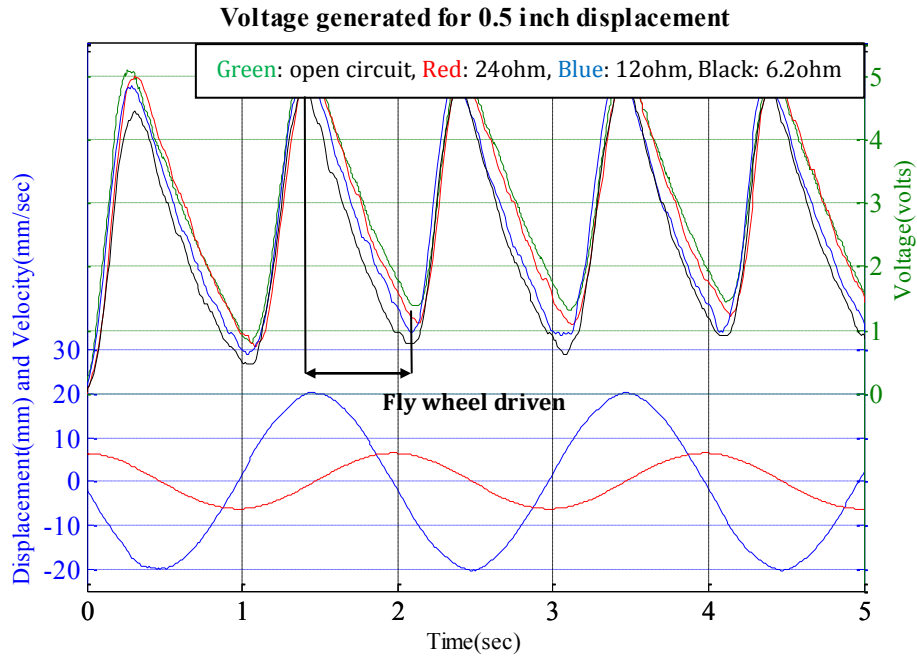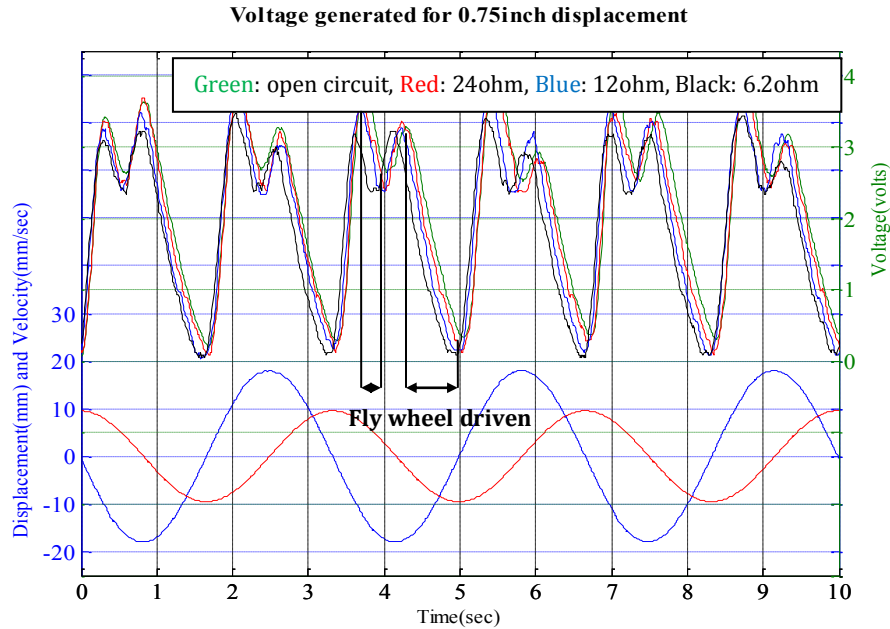

Figure 10.20: Voltage generated for 0.75in rack displacement at frequency 0.3Hz for various resistors
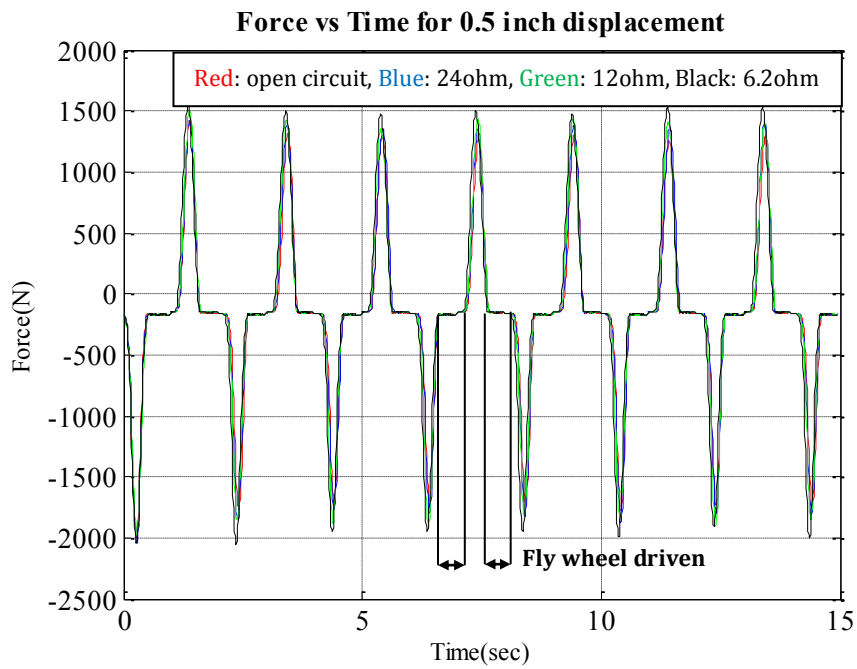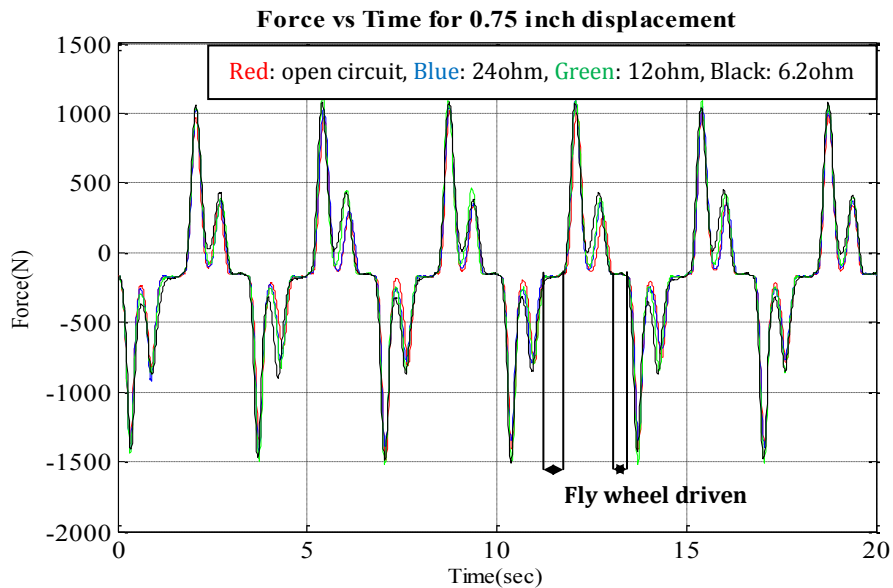

Figure 5.21: Force required for 0.75in rack displacement at frequency 0.3Hz for various resistors
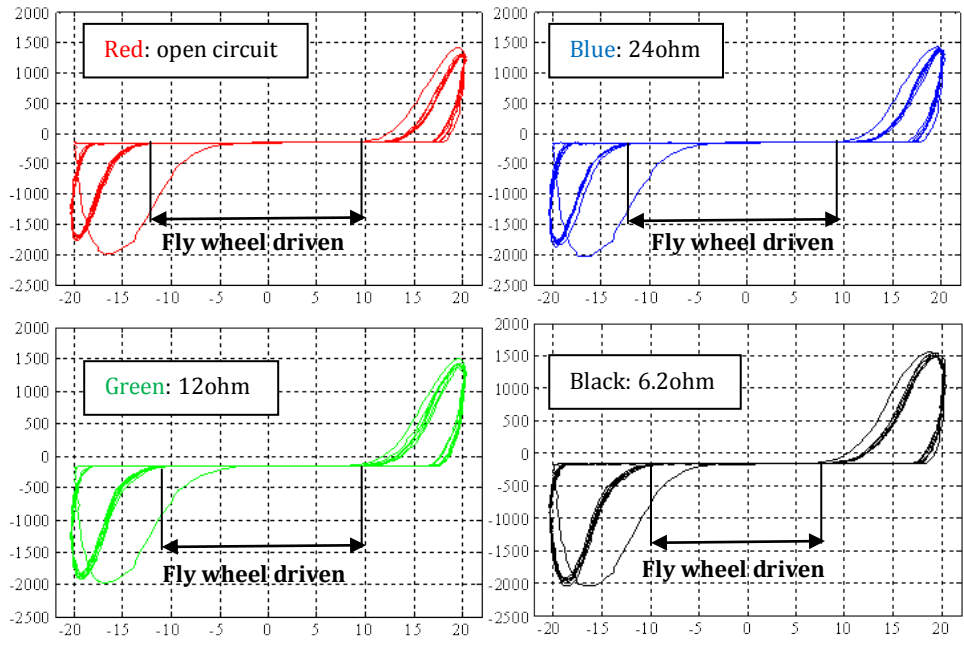
85
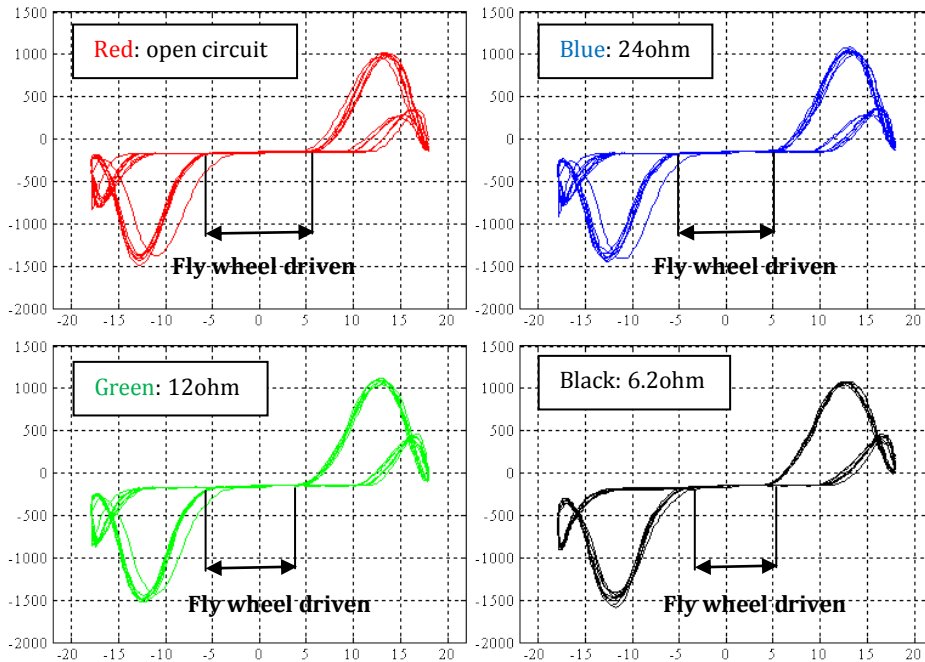
Figure 5.22 Force-velocity loops for 0.75in rack displacement at frequency 0.3Hz for various resistors

Table 5.5 overall efficiency of the system at 0.3Hz frequency for different power resistors

Resistance	6.2	12	24
Mechanical efficiency	11.91	7.12	3.71
Electrical Efficiency	88.9	93.75	96.8
Overall mechanical efficiency	10.59	6.67	3.60

The force vs. time is plotted for the same 0.75inch sinusoidal displacement input in Figure 5.21. The figure shows that the initial impact force in the first cycle is same as the force required in the later cycles. Since the displacement is higher the initial acceleration of the flywheel is low and the fly wheel will not generate sufficient inertia effect and always follow the rack and pinion motion.

The force vs. velocity is plotted for the same 0.75inch sinusoidal displacement input in Figure 5.22. The Figure clearly demonstrated the engagement and disengagement of the roller clutches. The Figure shows the idle period of the loop where the force required is at minimum, when both the roller clutches are disengaged. The Figure shows the roller clutch engagement and disengagement happens twice in a cycle, because of the very low input speed.

The above figures show that the there is very smooth engagement and disengagement of the roller clutches during the up and down motion of the rack and difference in the force required for

upward motion and downward motion is not very large, this is because of low frequency and high displacement input.

5.7 Future Work

5.7.1 Modeling the energy harvester

The dynamics of the nonlinear mechanical motion system has a perfect analogy in the electrical domain: full-wave voltage rectifier using a center-tapped transformer and two diodes. Figure 5.23 shows the analogy of the mechanical motion system and electrical voltage rectifier, where the two roller clutches correspond to the two semiconductor diodes, the rack acts as transformer's primary coil, and the two pinion gears correspond to the transformer's two secondary coils. The irregular vibration is converted into the regular rotation by the proposed mechanical motion system in a similar way as the AC voltage is converted into DC by the electrical voltage rectifier. The mechanical impedance (from the generator and harvesting circuit) acts as the electrical load in the electrical circuit. Therefore, we can use the well-developed principle of AC/DC powder electrical circuit to model the nonlinear mechanical motion rectifier system. Note again that this mechanical rectifier is to regulate the motion, not a substitute of electrical voltage rectifier.
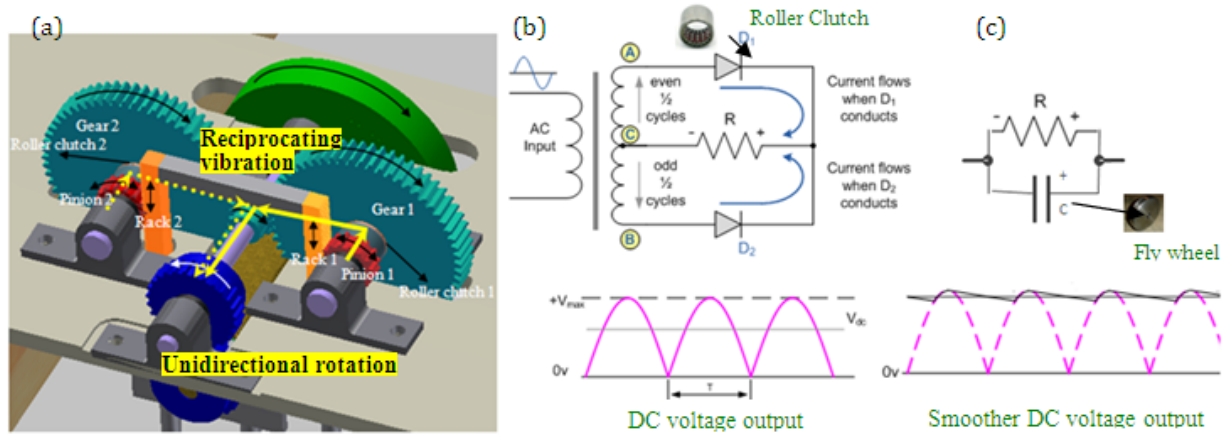
Figure 5.23: The proposed mechanical motion rectifier using a rack, two pinions and two roller clutches is analogy to a full-wave voltage rectifier using a transformer and two diodes.

5.7.2 Integration of a flywheel into vibration energy harvesting

In the electrical voltage rectifier, a capacitor is usually added in parallel with the resistive load, so that we can smooth the waveform and increase the output voltage V_{dc} from $2V_{peak}/\pi$ to nearly $V_{peak.}$ Similar principle can be extended to mechanical motion rectifier, in which we integrate a

"flywheel" to smooth the rotary motion of the generator which acts as capacitor in the elective voltage rectifier. The fly wheel will temporally store the peak kinetic energy that beyond the recovery capacity of generator and later converted into electricity. That is why combination of a flywheel in the regenerative braking can significantly improve the efficiency.

5.7.3 Improving the efficiency and reliability of the harvester

The harvester efficiency can be significantly improved by considering some design changes in the existing design. The modification to the design of the mechanical motion rectifier can be considered. The mechanical motion rectifier can be achieved in two different ways by changing the position of the roller clutches, one by placing the roller clutches under the pinion gears and the other by placing under the transmission gear which is similar to the one shown in this chapter. The best design which has less transmission losses can be identified before implementing the design.

The pillow blocks used in this design have more friction losses in them which will reduce the efficiency heavily. Since the shafts have different rotational speeds and subjected to different loads, proper selection of the pillow block has to be made instead of using the same pillow blocks for all shafts. The pinion shaft pillow blocks need more load bearing capacity and less speed and where the generator shaft pillow blocks needs less load bearing capacity and high rotational speed. So the pillow blocks with minimum frictional losses has to chosen for high efficiency.

The position of the fly wheel is also important, the fly wheel can be placed on either sides of the generator shaft, like the low speed side or the high speed side. Usually it is placed on the high speed side to generate more inertia, but the initial required torque is very high at high frequencies which will have huge stresses on the gears and shafts and lead to the reduce the reliability and also the safety factor has to be high while designing. If the flywheel is attached on the low speed side it will also less initial torque requirement but the inertia will be low which will make the fluctuation large. The proper study of this can help to increase the reliability of the harvester.

References

1. Federal Railroad Administration, Safety Statistics, U.S. Department of Transportation

2. M. Papaelias, C. Roberts, and C. L. Davis, 2006, "A review on non-destructive evaluation of rails: state-of-the-art and future development," *Proc. IMechE*, Vol. 222 Part F: J. Rail and Rapid Transit.

3. R. J. Greene, J. R. Yates, and E. A. Patterson, 2007, "Crack detection in rail using infrared methods," *Optical Engineering*, Vol. 46, No. 5

4. D. Hesse and P. Cawley, 2007, "Defect detection in rails using ultrasonic surface waves," *Insight*, Vol. 49(6), pp. 318–326.

5. R. S. Edwards, X. Jian, and S. Dixon, 2006, "Rail defect detection using ultrasonic surface waves. *Review of quantitative nondestructive evaluation*," Vol. 25, pp. 1601-1608.

6. M. Junger, H. M. Thomas, R. Krull, and S. Ruhe, "The potential of eddy current technology regarding railroad inspection and its implementation," In Proceedings of the 16thWorld Conference on Non-Destructive Testing,

7. R. Aharoni, and E. Glikman, 2002, "A novel high-speed rail inspection system," In Proceedings of the 8th ECNDT, Barcelona, Spain.

8. S. Dixon, R. S. Edwards and X. Jian, "Inspection of the rail track head surfaces using electromagnetic acoustic transducers," *Insight*, Vol. 46, pp. 326-330.

9. F. Di Scalea, P. Rizzo, S. Coccia, I. Bartoli, M. Fateh, E. Viola and G. Pascale, 2005, "Non-contact ultrasonic inspection of rails and signal processing for automatic defect detection and classification," *Insight*, Vol. 47(6).

10. K. Bruzelius, D. Mba, 2004, "An initial investigation on the potential applicability of acoustic emission to rail track fault detection," *NDT&E Int*, Vol. 37(7).

11. C. Nelson, S. Platt, S. Farritor, D. Albrecht, and V. Kamarajugadda, 2007, Regenerative Power for Track-Health Monitoring. Reported to Federal Railroad Administration,

12. C A. Nelson, S R Plattb, S E. Hansen, M Fateh, 2009, "Power Harvesting for Railroad Track Safety Enhancement using Vertical Track Displacement," Proc. of SPIE: Active and Passive Smart Structures and Integrated Systems, Vol. 7288.

13. O. Orringer, J. Orkisz and Z. Swiderksi, 1992, "Residual stress in rails. *Field experience and test results*," Vol. 1.

14. R. C. Thakur, R. Topno, B. Krishna, B. Roy, and G. M. D Murty, 2006, "Residual stress measurement in rails. In Proceedings of the National Seminar on Non-Destructive Evaluation," Hyderabad, India.

15. J. L. Rose, M. J. Avioli, 2000, "Elastic Wave Analysis for Broken Rail Detection," 15th World Conference on Non-Destructive Testing, Rome, Italy.

16. G. Park, H. Sohn, C. R. Farrar, D. J. Inman, 2003, "Overview of Piezoelectric Impedance-based Health Monitoring and Path Forward," *The Shock and Vibration Digest*, Vol. 35, pp. 451-463.

17. D. Peairs, G. Park, and D. J. Inman, 2002, "Improving Accessibility of the Impedance based Structural Health Monitoring Method," *Journal of Intelligent Material Systems and Structures*.

18. W. Powrie and J. Priest, 2010, "Behavior of ballasted track during high speed train passage," University of Southampton, UK.

19. T. Hayashi, W. J. Song, J. L. Rose, 2003, "Guided wave dispersion curves for a bar with an arbitrary cross-section, a rod and rail example," *Ultrasonics,* Vol. 41, pp. 175–183.

20. I. Bartoli, A. Marzani, F. LanzadiScalea, E. Viola, 2006, "Modeling wave propagation in damped waveguides of arbitrary cross-section," *Journal of Sound and Vibration*, Vol. 295, pp. 685–707.

21. J. Ryue, D. J. Thompson, P. R. White, D. R. Thompson, 2008, "Investigation of propagating wave types in railway tracks at high frequencies," *Journal of Sound and Vibration,* Vol. 315, pp. 157–175.

22. J. Ryue, D. J. Thompson, P. R. White, D. R. Thompson, 2009, "Decay rates of propagating waves in railway tracks at high frequencies," *Journal of Sound and Vibration,* Vol. 320, pp. 955–976.

23. On-line High-speed Rail Defect Detection, U.S. Department of Transportation. Federal rail road administration.

24. I. Bartoli, F. Lanza di Scalea, M. Fateh, and E. Viola, 2004, "Modeling Guided Wave Propagation with Application to the Long-Range Defect Detection in Railroad Tracks," *NDT&E, International*.

25. F. Lanza di Scalea, and J. McNamara, 2003, "Ultrasonic NDE of Railroad Tracks: Air-coupled Cross-sectional Inspection and Long-range Inspection," *Insight-NDT and Condition Monitoring*, Vol. 45(6), pp. 394-401

26. P. Cawley, P. Wilcox, D. N. Alleyne, B. Pavlakovic, M. Evans, K. Vine, and M. Lowe, 2004, "Long range inspection of rail using guided waves – field experience," In Proceedings of the 16th World Conference on Non-Destructive Testing, Montreal, Canada.

27. P. Wilcox, M. Evans, B. Pavlakovic, D. Alleyne, K. Vine, P. Cawley, and M. Lowe, 2003, "Guided Wave Testing of Rail," *Insight-NDT and Condition Monitoring*, Vol. 45(6), pp. 413-420.

28. J. L. Rose, M. J. Avioli, P. Mudge, 2004, "Guided wave inspection potential of defects in rail," *NDT E Int*. Vol. 37, pp. 153–161.

29. J. L. Rose, M. J. Avioli, W. J. Song, 2002, "Application and potential of guided wave rail inspection," *Insight*, Vol. 44 (6), pp. 353–358.

30. C. Liang, F. P. Sun, and C. A. Rogers, 1994, "Coupled Electro-Mechanical Analysis of Adaptive Material Systems-Determination of the Actuator Power Consumption and System Energy Transfer," *Journal of Intelligent Material Systems and Structures*, Vol. 5, pp. 12-20.

31. Z. Chaudhry, T. Joseph, F. Sun, and C. Rogers, 1995, "Local-Area Health Monitoring of Aircraft via Piezoelectric Actuator/Sensor Patches," Proceedings, SPIE Conference on Smart Structures and Integrated Systems, Vol. 2443, CA.

32. F. Lalande, B. Childs, Z. Chaudhry, and C. A. Rogers, 1996 "High-Frequency Impedance Analysis for NDE of Complex Precision Parts," Proceedings, SPIE Conference on Smart Structures and Materials, Vol. 2717, pp. 237-245. CA.

33. G. Park, K. Kabeya, H. H Cudney, and D. J. Inman, 1999a, "Impedance-Based Structural Health Monitoring for Temperature Varying Applications," *JSME International Journal*, Series A, Vol. 42(2), pp. 249-258.

34. G. Park, H. Cudney, and D. J. Inman, 1999b, "Impedance-based Health Monitoring Technique for Massive Structures and High-temperature Structures," *Smart Structures and Materials*, Proceedings of SPIE, Vol. 3670, pp. 461-469.

35. G. Park, H. Cudney, and D. J. Inman, 2000a "Impedance-based Health Monitoring of Civil Structural Components," *ASCE Journal of Infrastructure Systems*, Vol. 6(4), pp. 153-160.

36. G. Park, H. Cudney, D. J. Inman, 2000b, "An Integrated Health Monitoring Technique Using Structural Impedance Sensors," *Journal of Intelligent Material Systems and Structures*, Vol. 11(6), pp. 448-455.

37. G. Park, H. Cudney, and D. J. Inman, 2001 "Feasibility of Using Impedance-based Damage Assessment for Pipeline Systems," *Earthquake Engineering & Structural Dynamics Journal*, Vol. 30(10), pp. 1463-1474.

38. V. Giurgiutiu, and A. Zagrai, 2000, "Characterization of Piezoelectric wafer Active Sensors," *Journal of Intelligent Material Systems and Structures*, Vol. 11, pp. 959-976.

39. V. Giurgiutiu, A. N. Zagrai, 2002, "Embedded Self-Sensing Piezoelectric Active Sensors for Online Structural Identification", *ASME Journal of Vibration and Acoustics*, Vol. 124, pp. 116-125.

40. V. Giurgiutiu, A. Zagrai, and J. J. Bao, 2002, "Piezoelectric Wafer Embedded Active Sensors for Aging Aircraft Structural Health Monitoring," *International Journal of Structural Health Monitoring*.

41. V. Giurgiutiu, A. Zagrai, J. J. Bao, J. Redmond, D. Roach, K. Rackow, 2003 "Active Sensors for Health Monitoring of Aging Aerospace Structures", *International Journal of*

the Condition Monitoring and Diagnostic Engineering Management, UK, Vol. 6(1), pp. 3-21.

42. V. Giurgiutiu, 2003, "Embedded NDE with Piezoelectric Wafer Active Sensors in Aerospace Applications", *Journal of Materials- Special Issue* on NDE.,

43. S. Bhalla, A. S. K. Naidu, and C. K. Soh, 2002a, "Influence of Structure-Actuator Interactions and Temperature on Piezoelectric Mechatronic Signatures for NDE", *The Shock and Vibration Digest*, Vol. 35(6), pp. 451-463.

44. S. Bhalla, A. S. K. Naidu, C. W. Ong, and C. K. Soh, 2002b, "Practical Issues in the Implementation of Electro-mechanical Impedance Technique for NDE", Proceedings of SPIE on Smart Materials, Nano-, and Micro-Smart Systems,

45. A. Naidu, S. Bhalla, 2002, "Damage Detection in Concrete Structures with Smart Piezoceramic Transducers," Proceedings of SPIE on Smart Materials Structures and Systems, India.

46. X. M. Wang, C. Ehlers, and M. Neitzel, 1996, "Dynamic analysis of piezoelectric actuator bonded on beam," Proceedings of 3rd International Conference on Intelligent Materials SPIE, Vol. 2779, pp. 883-890.

47. J. P. Stokes and G. L Cloud, 1993, "The Application of Interferometric Techniques to the Nondestructive Inspection of Fiber-reinforced Materials", *Experimental Mechanics*, V. 33, pp. 314-319.

48. S. Bhalla. A. Gupta, S. Bansal and T. Garg, 2009, "Ultra Low-Cost Adaptations of Electro-mechanical Impedance Technique for Structural Health Monitoring", *Journal of Intelligent Material Systems and Structures*, Vol. 20.

49. J. Esteban, 1996. "Modeling of the Sensing Region of a Piezoelectric Actuator/Sensor", Ph.D. Dissertation, Virginia Polytechnic Institute and State University, Blacksburg, VA.

50. S.R. Anton, D.J. Inman, G. Park, 2009, "Reference-free damage detection using instantaneous baseline measurements," *AIAA Journal*, Vol. 47, pp. 1952–1964.

51. S. B. Kim and H. Sohn, 2007, "Instantaneous reference-free crack detection based on polarization characteristics of piezoelectric materials," *Smart Mater. Struct.* Vol. 16, pp. 2375–2387.

52. A. P. Seunghee, B. C. Lee, H. sohn, 2009, "Reference-free crack detection using transfer impedances," *Journal of Sound and Vibration*.

53. F. Bouteiller, B. L. Grisso, D. M. Peairs, D. J. Inman, 2006, "Broken rail track detections using smart materials," Proceedings of SPIE on NDE for Health Monitoring and Diagnostics, Vol. 6178, pp. 65–75, CA.

54. Innowattech Ltd, Haifa 32000, Israel, www.innowattech.co.il/

55. H. Abramarich, E. Harash, Milogram, Amit, Azilay, 2008, Power Harevsting from railways; apparatus, system and method US patent 7812508.

56. Z. F. Mian, 2009, Wireless railroad monitoring US patent 12/493,789

57. C. A. Nelson, S. R. Platt, D. Albrecht, V. Kamarajugadda, and M. Fateh, 2008, "Power Harvesting for Railroad Track Health Monitoring Using Piezoelectric and Inductive Devices," Proc. Of the SPIE: Active and Passive Smart Structures and Integrated Systems, vol. 6928(1).

58. P. J. Remington, Wheel/rail noise— part IV: rolling noise, *Journal of Sound and Vibration* Vol. 46 pp. 419–436.

59. J. L. Rose, Ultrasonic Waves in Solid Media, Cambridge University Press, Cambridge, 1999.

60. Http://www.molyneuxindustries.com/RailData.htm.

61. W. Yan, and F. D. Fischer, 2000, " Applicability of the Hertz contact theory to rail-wheel contact problems," *Arch. Appl.Mechanics*, Vol. **70**, pp. 255-268.

62. Y. C. Chen and J. H. Kuang, 2002, "Contact stress variations near the insulated rail joints," Proc Instn Mech Engrs, Vo.l, IMechE.

63. P. J. Remington, Wheel/rail noise— part IV: rolling noise, 1976, *Journal of Sound and Vibration* Vol. 46, pp. 419–436.

64. X. Wang and J. Tang, 2010a, "An enhanced piezoelectric impedance approach for damage detection with circuitry integration" *Smart Mater. Struct*.

65. X. Wang and J. Tang, 2010b, "Damage detection using piezoelectric admittance approach with inductive circuitry", *J. Intell. Mater. Syst. Struct*.

66. R. B. Goldner and P. Zerigian, 2005, "Electromagnetic linear generator and shock absorber," US Patent Specification 6,952,060 B2 (inventors; Trustees of Tufts College, assignee. Oct. 4 2005)

67. Tiefenbach USA Lt http://www.tiefenbach.com/store/product_detail_pages/railway.htm

68. GE Transportation Lt http://www.getransportation.com/rail/rail-products.html

69. J. Igwemezie, 2007, "Understanding Stresses in Rails," *Interface Journal of wheel/Rail interaction.*

70. S. Farritor, R. Arnold, and S. Lu, B. McVey, C. Hogan, and C. Norman, 2006, " Real-Time Vertical Track Modulus Measurement System from a Moving Railcar," Reported to Federal Railroad Administration.

71. D. Bowness, A. C. Lock, W. Powrie, J. A. Priest, and D. J. Richards, 2006, "Monitoring the dynamic displacements of railway track," Proceedings of the IMEE, Rail and rapid transit.

72. Finite Element Method Magnetics http://femm.foster-miller.net/wiki/

73. H. Grabe, 2010, "Axle load and track deflection on a heavy haul line. *Civil engineering.*

74. K. Oldknow, R. Reiff, 2006, "Use of Dynamic Rail Deflection as a Means of Determining Changes in Top of Rail Friction," Reported to Federal Railroad Administration.

75. L. Zuo, B. Scully, J. Shestani and Y. Zhou, 2010, "Design and characterization of an electromagnetic energy harvester for vehicle suspensions," *Smart Materials and Structures.*

76. X. Tang, L. Zuo, T. Lin, and P. Zhang, 2001, "Improved Design of Linear Electromagnetic Transducers for Large-Scale Vibration Energy Harvesting," Smart Structures and Materials: Proceedings of SPIE. CA.

77. X. Tang and L. Zuo, 2009, "Towards MESO And Macro Scale Energy Harvesting of Vibration," Proceedings of the 2009 ASME International Mechanical Engineering Congress and Exposition, Florida.

78. Z. Li, Z. Brindak, and L. Zuo, 2011 "Modeling of an Electromagnetic Vibration Energy Harvester with Motion Magnification", accepted by 2011 ASME International Mechanical Engineering Congress and Exposition

79. P. Zhang, Master thesis, 2010, "Study of Road Energy and Regenerative Electromagnetic Shock Absorber", SUNY Stony Brook.